

MICROWAVE-INDUCED THERMOACOUSTIC TOMOGRAPHY: APPLICATIONS
AND CORRECTIONS FOR THE EFFECTS OF ACOUSTIC HETEROGENEITIES

A Dissertation

by

XING JIN

Submitted to the Office of Graduate Studies of
Texas A&M University
in partial fulfillment of the requirements for the degree of

DOCTOR OF PHILOSOPHY

December 2007

Major Subject: Biomedical Engineering

MICROWAVE-INDUCED THERMOACOUSTIC TOMOGRAPHY: APPLICATIONS
AND CORRECTIONS FOR THE EFFECTS OF ACOUSTIC HETEROGENEITIES

A Dissertation

by

XING JIN

Submitted to the Office of Graduate Studies of
Texas A&M University
in partial fulfillment of the requirements for the degree of

DOCTOR OF PHILOSOPHY

Approved by:

Co-Chairs of Committee,	Lihong Wang
	Kenith Meissner
Committee Members,	Peter Kuchment
	Alvin T. Yeh
Head of Department,	Gerard L. Cote

December 2007

Major Subject: Biomedical Engineering

ABSTRACT

Microwave-Induced Thermoacoustic Tomography: Applications and Corrections
for the Effects of Acoustic Heterogeneities. (December 2007)

Xing Jin, B.S., Northwestern Polytechnical University, China;

M.S., Louisiana State University

Co-Chairs of Advisory Committee: Dr. Lihong Wang
Dr. Kenith Meissner

This research is primarily focused on developing potential applications for microwave-induced thermoacoustic tomography and correcting for image degradations caused by acoustic heterogeneities. Microwave-induced thermoacoustic tomography was first used to verify the feasibility of noninvasively detecting the coagulated damage based on different dielectric properties between normal tissue and lesion treated with high intensity focused ultrasound. Good image contrasts were obtained for the lesions. A comparison of the size of the lesion measured with microwave-induced thermoacoustic tomography and the size measured by a gross pathologic photograph was presented to verify the effectiveness the proposed method. Clinical data for breast tumors were also collected to verify the feasibility of using microwave-induced thermoacoustic tomography in breast cancer imaging. Next, the effects of acoustic heterogeneities on microwave-induced thermoacoustic tomography in weakly refractive medium were investigated. A correction method based on ultrasonic transmission tomography was proposed to correct for the image distortion. Numerical simulations and phantom

experiments verify the effectiveness of this correction method. The compensation is important for obtaining higher resolution images of small tumors in acoustically heterogeneous tissues. Finally, the effects of the highly refractive skull on transcranial brain imaging were studied. A numerical method, which considered wave reflection and refraction at the skull surfaces, was proposed to compensate for the image degradation. The results obtained with the proposed model were compared with the results without considering the skull-induced distortion to evaluate the skull-induced effects on the image reconstruction. It was demonstrated by numerical simulations and phantom experiments that the image quality could be improved by incorporating the skull shape and acoustic properties into image reconstruction. This compensation method is important when the thickness of skull cannot be neglected in transcranial brain imaging.

*To my husband Yongjun and my parents.
Thank you for your love and unconditional support.*

ACKNOWLEDGMENTS

This project was made possible by my advisors: Dr. Lihong Wang and Dr. Kenith Meissner, as well as the other members of my committee: Dr. Alvin T. Yeh and Dr. Peter Kuchment.

I would like to express my appreciation to my advisors for their insight and guidance throughout this research. I would also like to thank Yuan Xu, Minghua Xu, Geng Ku, Alejandro Garcia-Uribe, Changhui Li, Xinmai Yang of Dr. Wang's Optical Imaging Laboratory, for useful discussion and help, and Dr. George Stoica for his knowledge and assistance with tissue samples.

I would like to thank my sisters for their love and support and my friends for the great time and understanding.

This project was sponsored in part by National Institutes of Health grants R01 NS46214 and R01 EB000712.

TABLE OF CONTENTS

	Page
ABSTRACT	iii
ACKNOWLEDGMENTS.....	vi
TABLE OF CONTENTS	vii
LIST OF FIGURES.....	ix
1. INTRODUCTION.....	1
2. MEASUREMENT OF THE MICROWAVE ABSORPTION COEFFICIENT	6
2.1 Energy deposition in TAT	6
2.2 Microwave absorption coefficient.....	7
2.3 Experimental results.....	9
3. APPLICATIONS IN MEDICAL IMAGING	14
3.1 Visualize HIFU-induced lesion with thermoacoustic tomography.....	14
3.2 Clinical breast cancer imaging	33
3.3 Other potential applications	39
4. THE EFFECTS OF ACOUSTIC HETEROGENEITIES IN WEAKLY REFRACTIVE MEDIUM	40
4.1 Introduction	40
4.2 Effects of acoustic heterogeneities on TAT in weakly refractive medium ...	42
4.3 Theoretical basics and methods.....	46
4.4 Experimental system	52
4.5 Results and discussion.....	54
4.6 Conclusions	66
5. THE EFFECTS OF ACOUSTIC HETEROGENEITIES ON TRANSCRANIAL BRAIN IMAGING.....	67

	Page
5.1 Introduction	67
5.2 Theory and method.....	70
5.3 Results	81
5.4 Discussion	94
5.5 Conclusion.....	96
6. SUMMARY AND CONCLUSIONS.....	97
REFERENCES.....	99
VITA	110

LIST OF FIGURES

	Page
Fig. 2.1 Schematic of the experimental setup for measuring dielectric properties	10
Fig. 2.2 Dielectric properties: (a) real component of complex relative permittivity of test samples and (b) imaginary component of complex relative permittivity of test samples.....	12
Fig. 2.3 (a) Microwave absorption coefficients of tissues as compared with water, and (b) $1/e$ penetration depth in biological tissue as compared with water.....	13
Fig. 3.1 Side view of the experimental setup.....	17
Fig. 3.2 (a) Gross pathologic photograph of the sample used in the experiment. (b) Reconstructed image using the local-tomography-type algorithm. (c) Reconstructed image using the approximate filtered back-projection algorithm.....	21
Fig. 3.3 (a) Photograph of the phantom used in the experiment. (b) Reconstructed image using local-tomography-type method.	22
Fig. 3.4 (a) Gross pathologic photograph of the sample used in the experiment; the lesion was induced at an RF power of 15 W for one and half minutes; (b) Schematic side view of the sample.	23
Fig. 3.5 Comparison of the pizeoelectric signal before and after the treatment	24
Fig. 3.6 Reconstructed image using local-tomography-type reconstruction method: (a) before heating; (b) after heating. (c) The differential image obtained by subtracting the data collected before heating from the data collected after heating. (d) Reconstructed profile across the region at a depth shown by arrows in (a) and (b)	25
Fig. 3.7 Scatter plot of the area of the lesion evaluated using TAT vs. the area measured from pathologic photographs.....	27

Fig. 3.8 Simulation of a piezo-electric signal in response to a microwave-induced thermoacoustic signal.	31
Fig. 3.9 (a) TAT image of the mastectomy specimen. The tumor region has been identified as the region denoted by the two solid gray arrows; (b) Line profile across the tumor region indicated by the two dashed gray arrows in (a); (c) Preoperative sonogram; (d) Digital radiograph of the mastectomy specimen	35
Fig. 3.10 (a) Thermoacoustic image of the excised whole breast (mastectomy specimen). The tumor region is indicated by the gray arrows. 12 o'clock and 3 o'clock are marked. (b) Line profile across the tumor region indicated by the two black arrows in (a). (c) Digital radiograph of the mastectomy specimen. 12 o'clock and 3 o'clock are marked. (d) Postoperative sonogram of the breast.	37
Fig. 4.1 Ray refraction at the boundary between two different tissues	45
Fig. 4.2 Experimental setup and the scanning geometry: (a) Experimental setup for the combined TAT/UTT imaging system and (b) Schematic of the scanning geometry in top view.	52
Fig. 4.3 Numerical simulation: (a) Object function (distribution of microwave absorption) for TAT in the simulated phantom sample and (b) object function (acoustic speed distribution) for UTT in the sample. (c) Close-up TAT image without correction for the acoustic speed variations and (d) close-up TAT image with correction for acoustic speed variations.	56
Fig. 4.4 Effects of speed variations on a sample made with gelatin: (a) TAT image without speed compenstaion; (b) TAT image with speed compenstaion by adjusting average speed.	57
Fig. 4.5 Effects of speed variations on a sample made with porcine fat and muscle: (a) TAT image without speed compenstaion; (b) TAT image with speed compenstaion by adjusting average speed.	58

Fig. 4.6 (a) Schematic graph of the phantom used in the experiment; (b) Time of flight image reconstructed from the measurements by ultrasound transmission tomography; (c) Reconstructed speed-of-sound image by using filtered back-projection method.	59
Fig. 4.7 Phantom experiment: (a) Photograph of the phantom sample in top view, (b) the speed-of-sound image of the phantom sample; (c) close-up TAT image obtained by adjusting the average acoustic speed (boundaries are denoted by arrows), (d) close-up TAT image obtained by acoustic speed compensation using the acoustic speed distribution (boundary are denoted by arrows).	61
Fig. 4.8 Phantom experiment: (a) Photograph of the phantom sample in top view, the three absorbers were made by porcine muscle, (b) the speed-of-sound image of the phantom sample, (c) TAT image obtained by adjusting the average acoustic speed (boundaries are denoted by arrows), (d) TAT image obtained by acoustic speed compensation using the acoustic speed distribution (boundary are denoted by arrows), (e) line plot across absorber 1 as pointed by the gray dashed arrows in (c), and (f) line plot across absorber 3 as pointed by the gray dashed arrows in (c).	63
Fig. 5.1 Schematic illustration of the reflection, refraction, and mode conversion of the longitudinal incident waves.	71
Fig. 5.2 Schematic illustration of the forward TAT propagation.	76
Fig. 5.3 Numerical simulation: (a) Schematic illustration of the phantom sample used in the simulation; (b) Close-up view of the five absorbers in the imaging area; (c) Reconstructed TAT image without correction for the skull effects; (d) Reconstructed image after correction for the skull effects; (5) Comparison of the reconstructed profile across the five absorbers.	83
Fig. 5.4 Side view of experimental setup using a piece of monkey skull bone.	84

- Fig. 5.5 Thermoacoustic signals after traveling through a monkey skull bone with a thickness of 6 mm: (a) Phase shift is marked by two dotted perpendicular lines; (b) Amplitude attenuation after phase shift has been compensated for; (c) Comparison of amplitude spectrum of the thermoacoustic signals with and without the skull present..... 85
- Fig. 5.6 Reconstructed TAT image (a) using filtered back-projection method when skull was absent; (b) using filtered back-projection method when skull was present; (c) using proposed numerical method when skull was present; (d) comparison of the reconstructed signals at the depth as marked on (a), (b), and (c). 88
- Fig. 5.7 Experimental results with two strong absorbers: (a) Schematic of the phantom sample used in experiments; (b) reconstructed image when no PVC tube was used in the experiment; (c) Reconstructed TAT image using the filtered back-projection method; (d) Reconstructed TAT image using the numerical method proposed in this section; (e) Reconstructed profiles across the region at the depth as marked on (c) and (d). 91
- Fig. 5.8 Experimental results with a wire object: (a) Schematic of the phantom sample used in experiments; (b) Reconstructed image when no PVC tube was used in the experiment. (c) Reconstructed TAT image using the filtered back-projection method; (d) Reconstructed TAT image using the numerical method proposed in this section; (e) Reconstructed profiles across the region at the depth as marked on (c) and (d)..... 93

1. INTRODUCTION

When electromagnetic energy is delivered into biological tissue, a portion of the energy is absorbed by the tissue and converted to heat. A temperature gradient is then produced by the heating based on the energy absorption pattern, and subsequently ultrasonic waves are generated through thermal expansion. This is called thermoacoustic effects.¹⁻⁶ In recent years, there is an increasing interest in developing new diagnostic imaging modalities based on thermoacoustic effects, in which laser-induced photoacoustic tomography (PAT), microwave-induced thermoacoustic tomography (TAT), and photoacoustic microscopy (PAM) have attracted the attentions of researchers from various fields.

Other diagnostic imaging tools include ultrasound imaging, X-ray, positron emission tomography (PET), magnetic resonance imaging (MRI), etc. Those imaging modalities relate different biological parameters with different sensitivity to pathophysiological processes, and, therefore, they have both advantages and limitations. Among them traditional X-ray and positron emission tomography (PET) are either ionizing or radioactive; the image contrast of ultrasonic imaging is limited by the mechanical properties of the tissue; the size and cost of MRI prevents its use as a portable and routine screening tool. Thermoacoustic effects directly relate the pattern of the absorbed electromagnetic energy with generated thermoelastic waves, and, thus, it

This dissertation follows the style of Medical Physics.

can provide some unique physical and chemical information for noninvasive tissue characterization.

The imaging modalities based on thermoacoustic effects are noninvasive and nonionizing. The sizes of imaging systems for PAT, PAM and TAT at 3 GHz are small, and can be easily made portable. Among the three imaging modalities, PAT and PAM are laser-based imaging modality. PAT has been successfully applied in imaging vascular structure in the tissue and doing functional brain imaging in small animals,^{7,8} and PAM obtained promising results in imaging subcutaneous microvasculature and functional imaging of single vessels in animals and total hemoglobin concentration in humans.^{9,10} Nevertheless, their applications are limited by the penetration depth of the laser lights in the visual light region. By using near-infrared laser and a contrast agent, Ku and Wang¹¹ have reported 5~6 cm penetration depth for PAT with phantom experiments, but since the electromagnetic properties of human tissues change with wavelengths, microwave-induced TAT and near-infrared PAT can provide different thermal properties of the tissue.

In microwave-induced TAT, the ultrasonic wave that is generated through thermoelastic expansion will propagate through a coupling medium, and then detected by the ultrasonic transducer to map the distribution of the energy deposition in the tissue. TAT has been developed to overcome the limitations of both conventional ultrasound and microwave imaging. Microwave imaging has been used in imaging of soft tissue structures, but its application is limited by the low resolution of microwave, which is usually at centimeter level.¹² Ultrasound imaging has low image contrast but relatively

high image resolution depending on the wavelength used for imaging. Microwave-induced TAT combines the advantages of microwave imaging and conventional ultrasound imaging. Its image contrast is determined by the differences in the microwave absorption coefficients of different biological tissues, and its resolution is determined by the wavelengths of the generated ultrasonic waves. Microwave absorption coefficients of tissues are determined by their dielectric properties.¹³ It has been reported that malignant tissue and normal tissue differ substantially in their water content, and, consequently, their dielectric properties varies greatly. Most of the other soft tissues have a value between them.¹³⁻¹⁷ In our current TAT experiments, the image contrast between normal and malignant tissue is about 2~5 times, and the image resolution is less than 1 mm. Also the radiation level of microwave energy is below the safety limit on human subjects. TAT, therefore, has the potential for applications in tumor detection and treatment monitoring.

Recently a lot of efforts have been done to develop new applications for TAT.¹⁸⁻²³ Kruger *et al.*^{21,22} studied feasibility of using a 433 MHz TAT system in breast cancer imaging. Xu and Wang²³ obtained trans-skull brain imaging on Rhesus monkey with a 3 GHz TAT system. Ku *et al.*²⁴ proposed a new imaging method by combining microwave-induced TAT and near-infrared PAT. More efforts, however, are still necessary to explore new applications for TAT and to improve current technology to get better image quality for potential clinical applications.

In this research, first we will explore potential application for TAT. Here, we focus on verifying the effectiveness of using TAT in visualizing HIFU-induced lesion

and getting clinical data for breast cancer imaging with our 3 GHz TAT system. Next, we will investigate the effects of acoustic heterogeneities on TAT. Existing reconstruction algorithms for TAT are based on the assumption that the acoustic properties in the tissue are homogeneous, biological tissue, however, has heterogeneous acoustic properties, which lead to distortion and blurring of the reconstructed images. It is, therefore, necessary to evaluate the effects the acoustic heterogeneities on TAT image, and propose compensation methods to minimize those effects.

In section 2, we introduced a method to measure microwave absorption coefficient and obtained the dielectric properties of the tissues used for this research.

In section 3, first, thermoacoustic tomography was applied to the visualization of high-intensity focused ultrasound (HIFU)-induced lesions. Two reconstruction algorithms were explored: a filtered back-projection and a local-tomography-type algorithm, where the latter was implemented to emphasize the boundaries between the different tissues. Gross pathologic photographs of the tissue samples were used to confirm the effectiveness of TAT. Next, clinical experimental data were obtained in M. D. Anderson cancer center for breast tumors. The results were compared with ultrasonic image and X-ray CT image to evaluate the effectiveness of TAT for breast cancer imaging. A possible application of TAT in joint imaging was also briefly introduced.

In section 4, a correction method based on ultrasonic transmission tomography was developed to improve the image quality of TAT in weakly refractive medium. We analyzed the effects of acoustic speed variations on TAT and then proposed a compensation method based on ultrasonic transmission tomography to correct for these

effects. Numerical simulations and phantom experiments were used to verify the effectiveness of this correction method.

In section 5, the effects of acoustic heterogeneities on trans-skull brain imaging with microwave-induced thermoacoustic tomography were studied. A numerical model for calculating the propagation of thermoacoustic waves through the skull was developed and experimentally examined. The model takes into account the wave reflection and refraction at the interfaces between the skull and surrounding media therefore provides improved accuracy for the reconstruction. This compensation method is important for obtaining good brain images when the effects of acoustic heterogeneities cannot be ignored.

2. MEASUREMENT OF THE MICROWAVE ABSORPTION COEFFICIENT

2.1 Energy deposition in TAT

The propagation of an electromagnetic field in a medium is defined by the relationship

$$E = E_0 e^{j\omega t - \gamma(\omega)z} \quad (2.1)$$

where E is the electric field at a distance Z from the source of field strength E_0 . The propagation constant $\gamma(\omega)$ can be written as^{25,26}

$$\gamma(\omega) = \alpha(\omega) + j\beta(\omega) \quad (2.2)$$

where $\alpha(\omega)$ and $\beta(\omega)$ are the attenuation constant and phase constant at angular frequency ω , respectively. The energy deposition by the electromagnetic radiation at a specific point in tissue is determined by its dielectric properties and the electrical field at that specific location. To find the total rate of energy absorbed by an object, we use specific absorption rate (SAR), which is defined as

$$SAR = \sigma |E|^2 / \rho \quad (2.3)$$

where ρ is the mass density of the object at that point and σ is the conductivity of the tissue.²⁷ We will show that attenuation constant can be derived from the dielectric properties of a material in the next section. Therefore, if we know the dielectric properties of a tissue, we can estimate the strength of the electric field and the conductivity of the tissue at a specific point, and then we can easily estimate the energy deposition at that location.

To evaluate the effectiveness of a contrast agent for TAT, we need to estimate the electrical field within the tissue. In our experiments the sizes of test samples are small as compared with the wavelength of the microwave source. Thus, we assume uniform electric-field distribution in test samples to simplify the computation. Also as shown in the definition of SAR, the phase constant of the electric field does not have any effects on the value of energy deposition, therefore we only need to find attenuation constant of the tissue. Moreover, because the attenuation of an electromagnetic field in a medium is mainly brought by dielectric loss, which will eventually produce a rise in temperature, we will use $\alpha(\omega)$ to evaluate the microwave absorption coefficient.

2.2 Microwave absorption coefficient

Permittivity relates to a material's ability to transmit an electric field. The complex relative permittivity $\varepsilon^*(\omega)$ is defined as $\varepsilon^*(\omega) = \varepsilon_r(\omega) - j\varepsilon_i(\omega)$, where $\varepsilon_r(\omega)$ and $\varepsilon_i(\omega)$ are the real and imaginary parts of the complex relative permittivity respectively. We will use two different definitions of the complex refractive index to derive the absorption coefficient of a material. The complex refractive index $n^*(\omega)$ for a given material is defined as the square root of the product of the complex relative permittivity $\varepsilon^*(\omega)$ and complex relative permeability $\mu^*(\omega)$,²⁸

$$n^*(\omega) = \sqrt{\varepsilon^*(\omega)\mu^*(\omega)} \quad (2.4)$$

Where $\mu^*(\omega) = \mu_r(\omega) - j\mu_i(\omega)$, $\mu_r(\omega)$ and $\mu_i(\omega)$ are the real and imaginary parts of the complex relative permeability, respectively, The complex refractive index can also be

derived from the extinction coefficient of tissue and is given by

$$n^*(\omega) = n(\omega) - jk(\omega) \quad (2.5)$$

where $k(\omega) = \lambda\alpha(\omega)/(2\pi)$ is the extinction coefficient. From Eqs. (2.4) and (2.5), we get

$$n(\omega) - jk(\omega) = \sqrt{(\varepsilon_r(\omega) - j\varepsilon_i(\omega))\mu^*(\omega)} \quad (2.6)$$

We first do a squaring of both sides of Eq. (2.6). Notice that the imaginary and real parts on the left side should equal to those on the right side, and, thus, we get two equations. Solving those two equations for $k(\omega)$ and using the relationship between $k(\omega)$ and $\alpha(\omega)$, and then we obtain the microwave absorption coefficient of a material as:

$$\alpha(\omega) = \frac{\omega}{c_0} \sqrt{\frac{\mu_r^*(\omega)\varepsilon_r(\omega)}{2} \left(\sqrt{1 + \left(\frac{\sigma(\omega)}{\omega\varepsilon_0\varepsilon_r(\omega)} \right)^2} - 1 \right)} \quad (2.7)$$

Where c_0 is the speed of electromagnetic waves in vacuum (approximately 3×10^8 m/s) and $\sigma(\omega)$ is the conductivity which is defined as $\omega\varepsilon_0\varepsilon_i(\omega)$ ($\varepsilon_0 = 8.85 \times 10^{-12}$ F/m is the permittivity of free space). $1/e$ penetration depth in the tissue is defined as $1/\alpha(\omega)$. For nonmagnetic materials, we have $\mu^*(\omega) = 1$. Eq. (2.7) can be further simplified as:

$$\alpha(\omega) = \frac{\omega}{c_0} \sqrt{\frac{\varepsilon_r(\omega)}{2} \left(\sqrt{1 + \left(\frac{\sigma(\omega)}{\omega\varepsilon_0\varepsilon_r(\omega)} \right)^2} - 1 \right)} \quad (2.8)$$

In our TAT system, the electric field is several orders stronger than the magnetic field. We will use Eq. (2.8) to calculate microwave absorption coefficients in the following experiments. When the magnetic properties cannot be ignored, we, however, need to

measure both the permittivity and permeability of the material to get a reasonable estimate of the absorption coefficient. This will be very difficult to implement in reality. Kim et al.²⁹ provides a simple experimental method using microwave oven to determine approximately the microwave energy deposition for this case. The experimental setup discussed below is only feasible for non-magnetic materials.

2.3 Experimental results

Among the different ways to measure relative permittivity, a coaxial probe is ideal for liquids and semi-solid materials,^{30,31} and has thus been chosen for our application. The open-ended coaxial probe can be regarded as a cut-off section of a transmission line. The dielectric properties of a material are measured by immersing the probe in a liquid or touching it to the flat face of a semi-solid test sample. The electric fields at the probe tip propagate into the test sample and vary as they come into contact with different test samples. The reflected signals from the test sample are then measured and related to the complex relative permittivity.

The main measurement system includes a coaxial probe kit, a network analyzer and a RF source. The microwave absorption coefficients are calculated using Eq. (2.8). The network analyzer measures the complex relative permittivity. The schematic graph of the experimental setup is shown in Fig. 2.1. We use an Agilent 8510C vector network analyzer to make broadband measurements from 200 MHz to 20 GHz. We use the Agilent 85070E dielectric probe kit which includes a coaxial probe and the corresponding software. An external computer controls the network analyzer through

GPIB. Before each measurement, a calibration at the tip of the probe must be performed. The principle of the calibration is to use the difference between the predicted and actual values of three well-known standards (air, a short circuit and deionized water) to remove the repeatable systematic errors from the measurement. Before making a measurement, we performed a system calibration. During the experiments, it is important to make sure that the cable is stabilized and not flexed between the calibration and measurement. The air bubbles on the tip of the probe need to be carefully removed to ensure the accuracy of a measurement. And the test sample must also be thick enough to appear infinite to the probe.

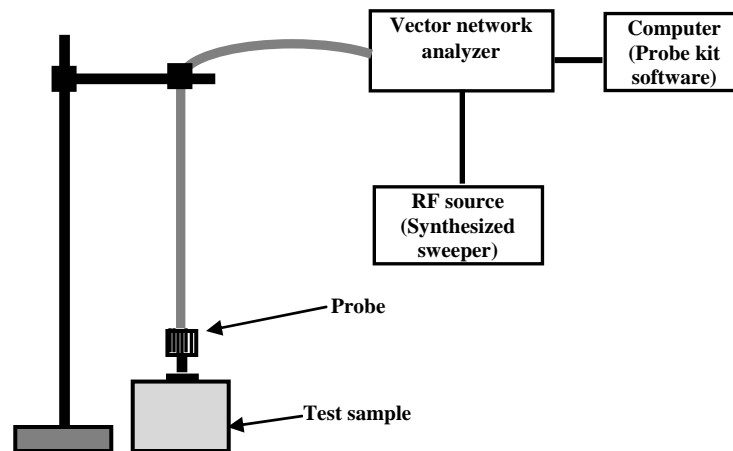


Fig. 2.1 Schematic of the experimental setup for measuring dielectric properties

Next, we measure the dielectric properties of some tissue samples used in this study by using the presented measurement method. Since tumorous tissues are associated with increasing level of water content, in this research we used muscle tissues to simulate the tumorous tissues because of similar dielectric properties.³² In the following experiment, we test three different muscles tissue, porcine fat and dionized water. The real component of complex relative permittivity is shown in Fig. 2.2(a), and the imaginary component of complex relative permittivity is shown in Fig. 2.2(b). It is observed that the dielectric properties of the muscle tissues from different species only varies a little, and the dielectric properties of the different tissue types for the same species, such as porcine fat and porcine muscle, differ greatly. The difference in dielectric properties is mainly determined by their difference in water content. The water content in muscle tissues is around 70%, and the water content in fat is around 20%. We know that the imaginary component of the complex relative permittivity ϵ_i is related to the conductivity of a material. We expect big differences in the microwave absorption coefficients between porcine fat and muscle tissues.

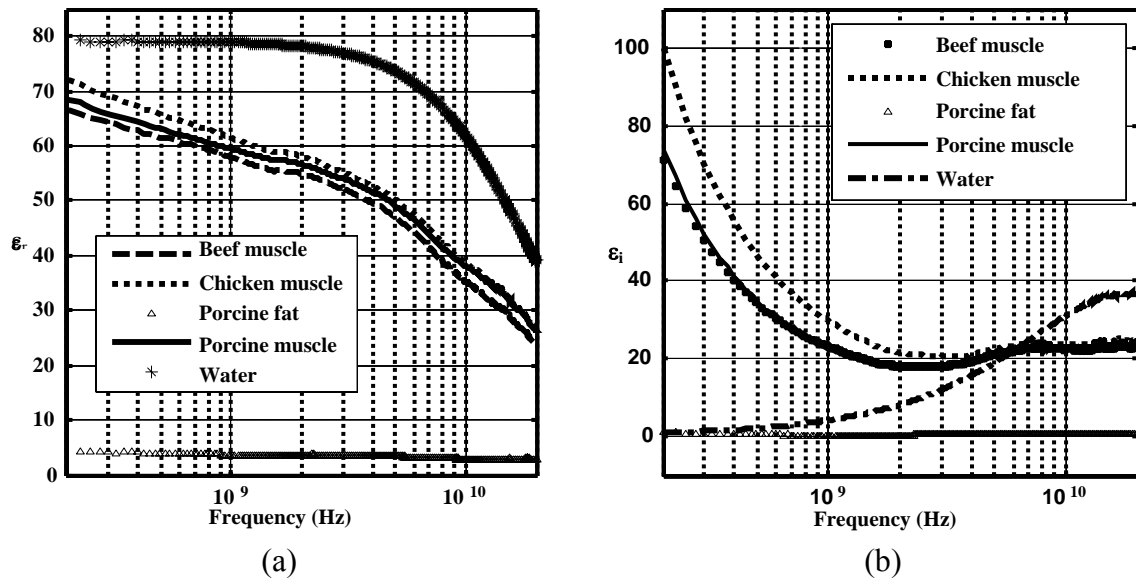
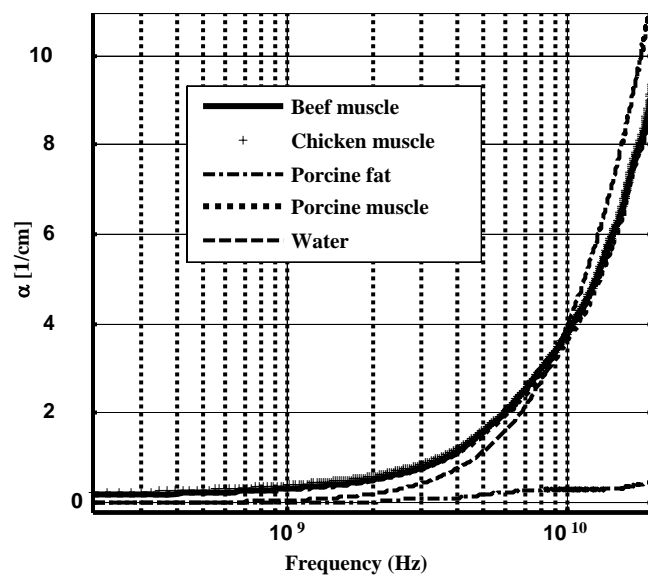
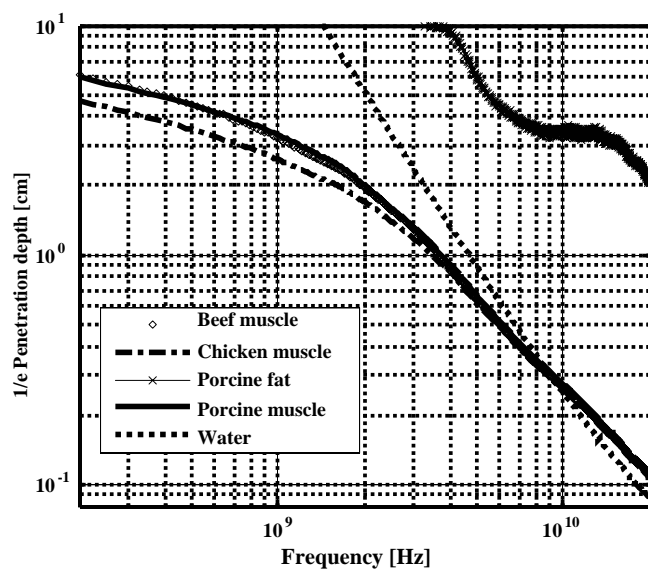


Fig. 2.2 Dielectric properties: (a) real component of complex relative permittivity of test samples and (b) imaginary component of complex relative permittivity of test samples.

The microwave absorption coefficient was calculated and shown in Fig. 2.3. As we expected, the microwave absorption rates of the muscles are close to that of the water, and are much greater than that of the fat tissue in a broad frequency range. $1/e$ microwave penetration depth in biological tissues is the inverse of the absorption coefficient. From Fig. 2.3(b), it is estimated that at 3 GHz, which is used by our TAT system, the penetration depth of muscle tissue is between 1~2 cm, and the penetration depth in fat is near 10 cm. Our measurements show good agreement with experimental data presented in literatures.¹⁴⁻¹⁶



(a)



(b)

Fig. 2.3 (a) Microwave absorption coefficients of tissues as compared with water, and (b) 1/e penetration depth in biological tissue as compared with water.

3. APPLICATIONS IN MEDICAL IMAGING*

3.1 Visualize HIFU-induced lesion with thermoacoustic tomography

3.1.1 Introduction

High-intensity focused ultrasound (HIFU) has been used as an effective minimally invasive treatment for tumors deep in the body.³³⁻³⁶ The objective of HIFU treatment is to use a highly focused ultrasound beam to destroy a predetermined volume of malignant tissue while minimizing, or avoiding, damage to the surrounding tissue. The HIFU beam introduces a rapid rise in temperature, which results in tissue coagulation, in the target region. Research using pathologic studies³⁷ has shown irreversible tumor cell death and severe damage to tumor blood vessels in the treated region in human tissue *in vivo*. The size and shape of the induced lesions are related to the amount of ultrasonic energy delivered to the tissue. Monitoring the treated region of the target tumor, as well as the untreated region, is important for providing feedback on the treatment.

To improve the clinical effectiveness of HIFU treatments, much effort has been focused on developing effective imaging techniques to visualize the treatment process as well as determine the immediate thermal effects. Currently, HIFU ablation damage is

*Reprinted with permission from “Imaging of HIFU-induced lesions in soft biological tissue using thermoacoustic tomography” by X. Jin, Y. Xu, L.-H. Wang, Y. R. Fang, C. I. Zanelli, and S. M. Howard, 2005. *Med. Phys.* 32, 5-11 Copyright [2005] by Medical Physics.

best observed by using MRI,³⁸⁻⁴⁰ but MRI makes the treatment cumbersome and expensive. Unfortunately, conventional pulse-echo ultrasonic imaging methods are not suitable for visualizing thermal damage because the ultrasonic backscattering coefficients of the HIFU-treated regions are not substantially different from those of the untreated surrounding regions. The changes in tissue during HIFU-treatment that can be observed by B-mode ultrasound imaging are thought to be influenced by gas bubbles and tissue vaporization which makes the detection unreliable. Studies on the acoustic properties of lesions have been carried out by many researchers.^{41,42} Their results show increases in the attenuation coefficient and the sound speed in the lesion region compared to those in untreated tissue regions. Imaging techniques based on changes in acoustic properties have been proposed to visualize HIFU-induced lesions, and while preliminary results have been obtained for ultrasonically homogeneous tissues such as liver, results for more heterogeneous tissues are still under investigation.^{43,44}

Thermal ablation of malignant tissue is associated with a decrease in water content and conductivity. There are two explanations for the loss of water in the lesion region. To kill malignant tissue with ultrasonic ablation, the temperature in the target region is elevated to 65 °C or higher. At such high temperatures, tissue begins to coagulate and subsequently water evaporates.⁴⁵ Due to water vaporization, the lesion region has less water content than the untreated region. In addition, reduced blood flow results in water loss. Experiments on breast tumor and liver tumor have shown that HIFU treatments interrupt the blood flow within tumor vessels, and, consequently, that the blood flow within the tumor vessels declines dramatically following HIFU

treatments.^{45,46} Because the lesion region has less water content than the untreated area and the conductivity of this region is, therefore, lower than that of the untreated area, it absorbs less microwave energy than the untreated area. The effect of the heating on the intracellular ionic concentration, however, is still not clear. Some research has claimed that no obvious changes in ionic concentration occur during or after heating.⁴⁷ Because TAT can differentiate thermally induced lesions from untreated tissue based on differences in their electromagnetic properties, it has the potential to image HIFU-induced lesions.

The purpose of this section is to establish the feasibility of using TAT to noninvasively detect the coagulated damage in tissue that is being treated. Two reconstruction algorithms are explored: a filtered back-projection and a local-tomography-type algorithm, where the latter was implemented to emphasize the boundaries between the different tissues. To verify that TAT can differentiate low water-content tissue from high water-content tissue, a sample was made by embedding low water-content fat in high water-content porcine muscle. This sample was then imaged. Subsequently, a HIFU-induced lesion in porcine muscle was produced for the purpose of evaluating the ability of TAT to detect ablation. Good contrast was obtained between the lesion and the tissue surrounding it. A comparison of the size of the lesion measured with TAT and the size measured by a gross pathologic photograph is also presented.

3.1.2 Experimental methods

A side view of the experimental setup is shown in Fig. 3.1. The tissue sample was constructed by embedding a piece of fresh porcine muscle in fat. The whole tissue sample was immersed in mineral oil and placed on a base in the X-Y plane. In the experiments, we carefully removed the air bubbles between the fat and muscle and fixed the relative position of the muscle with a thin string. The porcine muscle had a water content of $\sim 75\%$,³² which is similar to the water content of cancerous tissue.

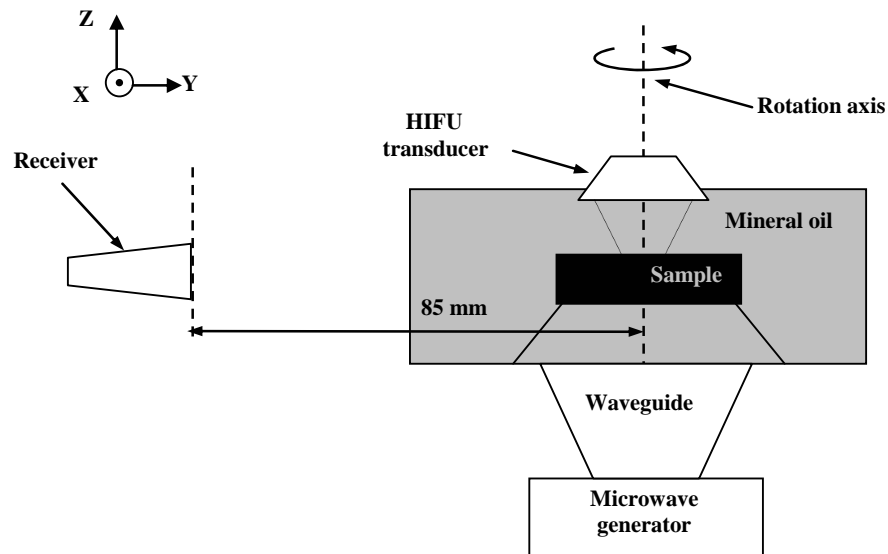


Fig. 3.1 Side view of the experimental setup.

The ultrasonic receiver was an unfocused transducer (V323, Panametrics NDT Inc.), with a central frequency of 2.25 MHz and a diameter of 6 mm. This receiver was scanned around the Z axis, and its axis was aligned with the center of the muscle.

Thermal lesions were induced in the muscle using a spherically focused transducer (Onda Corporation), which irradiated the sample from above, along the Z direction.

The HIFU transducer operated at a central frequency of approximately 4 MHz, with a focal length of 25 mm. It was driven by a continuous sinusoidal voltage produced by a signal generator (DS345, Stanford Research) and passed through a RF amplifier (240L, ENI). The HIFU transducer was immersed in mineral oil to provide coupling to the sample. Because the HIFU-induced lesion was formed preferentially before the focus, the distance between the HIFU transducer and the tissue sample was less than 25 mm.

The experiment was conducted in a plastic container filled with mineral oil. The plastic container was large enough so that the reflection of the thermoacoustic waves from the boundaries of the container would not interfere with our reconstruction results. The microwave energy was delivered into the biological tissue from the bottom of container through an air-filled pyramidal horn antenna with an opening of 120 mm x 88 mm. The tissue sample was placed above the opening of the antenna as shown in Fig. 3.1. The central frequency of the microwave generator was 3 GHz. At this frequency, the penetration depth in fat is 9 cm, and the penetration depth in muscle is 1.2 cm. Most other soft tissues have penetration depths between these two values. The peak power of the microwave pulse is estimated to be 2 kW, and the estimated total energy of the microwave pulse is about 1 mJ. The pulse width of the microwave source is 0.5 μ s, which means that ultrasonic waves up to \sim 2 MHz were generated, thus providing spatial resolution on the millimeter scale. We used an unfocused transducer (Panametrics-NDT,

model C3015, Waltham MA) with a central frequency of 1 MHz and bandwidth of 0.8 MHz as the receiver. The amplitude of the received data is at μV level; we amplified the thermoacoustic signal at 40~60 dB with an ultrasound pulser-receiver (Panametrics-NDT, model 5072PR, Waltham MA), and then sampled the data with an oscilloscope (Tektronix, model TDS640) at 20 MHz. The microwave generator and the oscilloscope were synchronized by a function generator. Several minutes after the lesion was generated in the tissue, we turned on the microwave generator and began to collect the thermoacoustic signals. The estimated microwave radiation level based on the above settings conforms to the safety requirements.²⁷ The data were then transmitted to the computer and recorded for further processing.

3.1.3 Reconstruction method

The reconstruction methods are based on previous studies.⁴⁸⁻⁵¹ An approximate 2-D filtered back-projection algorithm was applied to obtain an energy deposition image first. To emphasize the sharp details in the reconstructed image, we then used a local-tomography-type reconstruction algorithm that was also studied in the paper referenced above. In the following experiments, we reconstructed the image with full (panoramic) view data, which were collected by scanning the ultrasonic transducer around the tissue sample in a full circle. In practice, we often can obtain only limited-view data and then must use the limited-view algorithm discussed previously⁴⁸ to reconstruct the image.

3.1.4 Results and discussion

a) Experimental results

First, the reconstructed images, using two different reconstruction methods, are compared in Fig. 3.2(a) shows a gross pathologic photograph, and Fig. 3.2(b) shows the results of the approximate filtered back-projection method. Because of the band-limited effect of the receiving transducer, the low-frequency components of the thermoacoustic signals detected by the receiver were filtered out. To reconstruct the image through the approximate filtered back-projection method, we estimated the ultrasound pressure by integration. The integration process resulted in only an approximation of the non-filtered thermoacoustic signals. From Fig. 3.2(c), we observe that the reconstructed image is uniform due to the smoothing effect of this integration. Fig. 3.2 (b) is the result using a local-tomography-type algorithm; here the reconstructed image has better contrast. To better characterize the size and position of the lesion in the reconstructed image, we were interested in the interfaces between the muscle and the HIFU induced lesion, in which high-frequency components of the thermoacoustic signals dominated. For this reason, we used the local-tomography-type reconstruction method in our analysis. The image contrast in Fig. 3.2(b) is improved as a result of removing the low-frequency components and emphasizing the boundaries between the different tissues. Because of the filtering effects and our use of the local-tomography-type reconstruction method, the reconstructed image in Fig. 3.2(b) is not a direct energy deposition image.

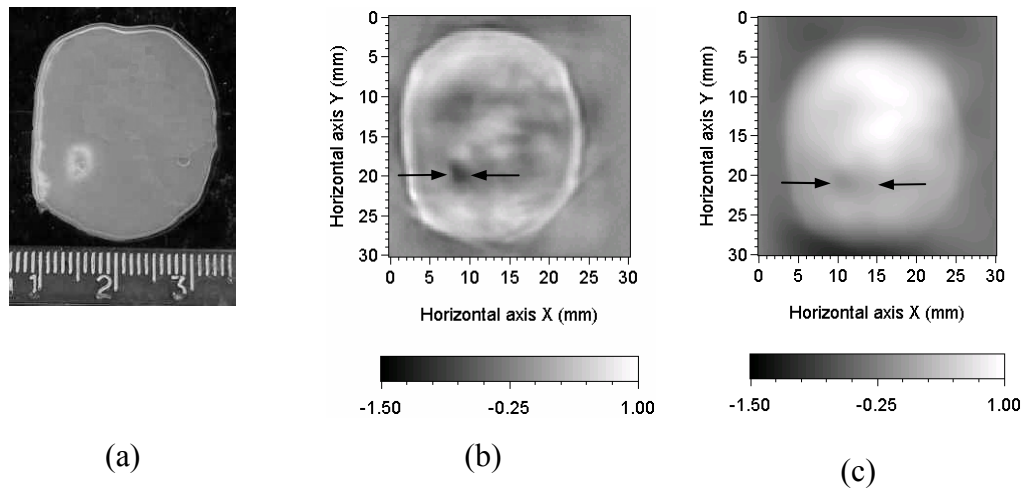


Fig. 3.2 (a) Gross pathologic photograph of the sample used in the experiment. (b) Reconstructed image using the local-tomography-type algorithm. (c) Reconstructed image using the approximate filtered back-projection algorithm. The lesion region is indicated by arrows.

Next, to examine the image contrast that results from the differences in water content in the different tissues, we began with a sample of two small pieces of fat embedded in a piece of porcine muscle. A photograph of the sample is shown in Fig. 3.3(a). The sample consisted of two fat cylinders with a diameter of about 7 mm and a thickness of 6 mm. Because the water content in fat is much lower than the water content in muscle, we expected a large contrast between the two small pieces of fat and their surrounding areas in the reconstructed image. Figure 3.3(b) shows the reconstructed image using the local-tomography-type reconstruction method. We observe large changes in the fat regions. This experiment verifies that image contrast is related to differences in the water content of biological tissues.

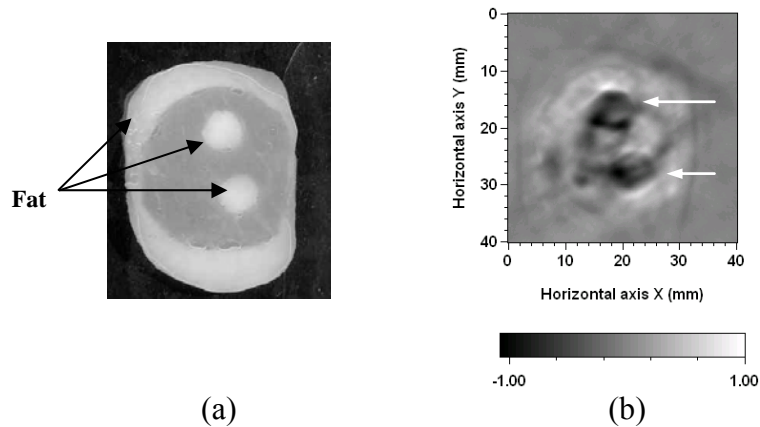


Fig. 3.3 (a) Photograph of the phantom used in the experiment. (b) Reconstructed image using local-tomography-type method.

Our final step was to generate HIFU-induced lesions in the tissue and obtain TAT images of them. Because our objective was to visualize HIFU-induced lesions with TAT, we attempted to simplify the creation of the lesions by not adding a layer of normal tissue above the tissue to be treated. This should have no effect on our results in terms of microwave penetration because the microwave energy source was placed beneath the sample to force the microwave pulses to propagate through the tissue. The tissue sample was constructed of a piece of muscle surrounded by fat. Figure 3.4(a) shows a photographic top view of the sample. Figure 3.4(b) depicts a schematic side view of the phantom used in the experiment. The approximate dimensions of the muscle were $40 \text{ mm} \times 30 \text{ mm}$, and the thickness of the muscle was 6 mm. The base fat was approximately 10 mm in thickness. Our current microwave radiation system had limited ability to provide uniformly distributed microwave energy to the tissue sample. This limitation determined the maximum size of the sample we could use without making spatial corrections. Other factors that determined the maximum size of the sample used

in the experiment included the frequency and power of the microwaves since microwave power is subject to safety requirements. The HIFU transducer heated the muscle sample from the top. The lesion was created by the HIFU transducer powered at 15 W, corresponding to approximately 600 W/cm^2 at the focus for 1.5 minutes. The dose of therapeutic ultrasound had been selected to induce water vaporization in the tissue. Several minutes after the formation of the lesion, we began to collect the TAT data. The thermoacoustic signals were sampled for $40 \mu\text{s}$ at a sampling rate of 50 MHz. The transducer was circularly scanned around the sample at a radius of 7.8 cm with a step size of 2.25° . At each detection angle, 200 thermoacoustic waves were averaged to abate the random noise and thus improve the signal-to-noise ratio of the detection.

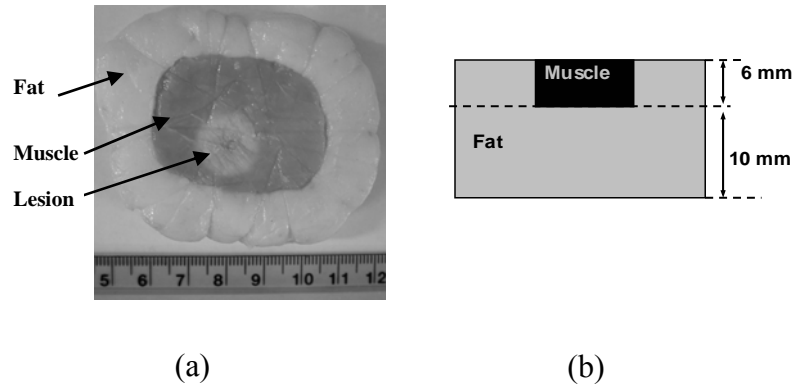


Fig. 3.4 (a) Gross pathologic photograph of the sample used in the experiment; the lesion was induced at an RF power of 15 W for one and half minutes; (b) Schematic side view of the sample.

The lesion showed up on the surface of the muscle as a white circle, sometimes with a central hole, which is clearly visible in Fig. 3.4(a). After heating, the tissue lost some of its water content due to water vaporization, which decreased accordingly its

ability to absorb microwave energy. Because in this case the fat under the muscle was only about 1cm in thickness, which was far less than the penetration depth in fat (9 cm at 3 GHz), the fat base had no obvious influence on the quality of the reconstructed TAT image.

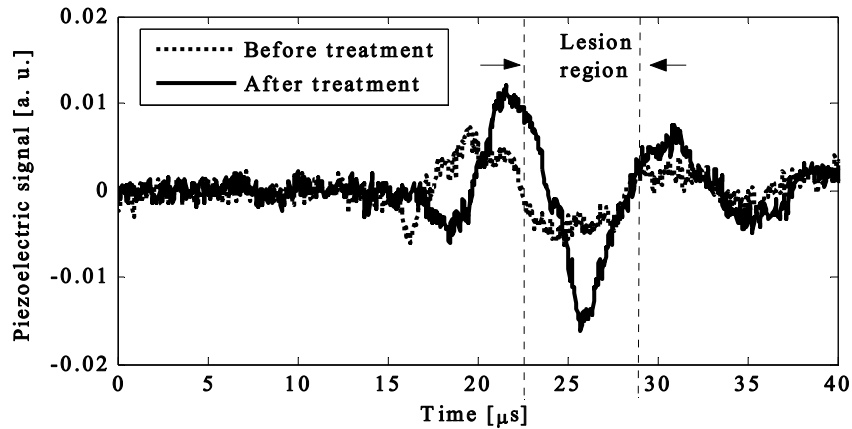


Fig. 3.5 Comparison of the piezoelectric signal before and after the treatment

In Fig. 3.5, we compared the thermoacoustic signal obtained before the treatment with that after treatment. The dotted plot is the thermoacoustic signal received by the ultrasonic transducer before the treatment, the solid line is the thermoacoustic signal received after the treatment. In the lesion region as shown between two perpendicular dashed lines, we observed a negative change in the signal strength after the treatment. We expect big change in the reconstruct image.

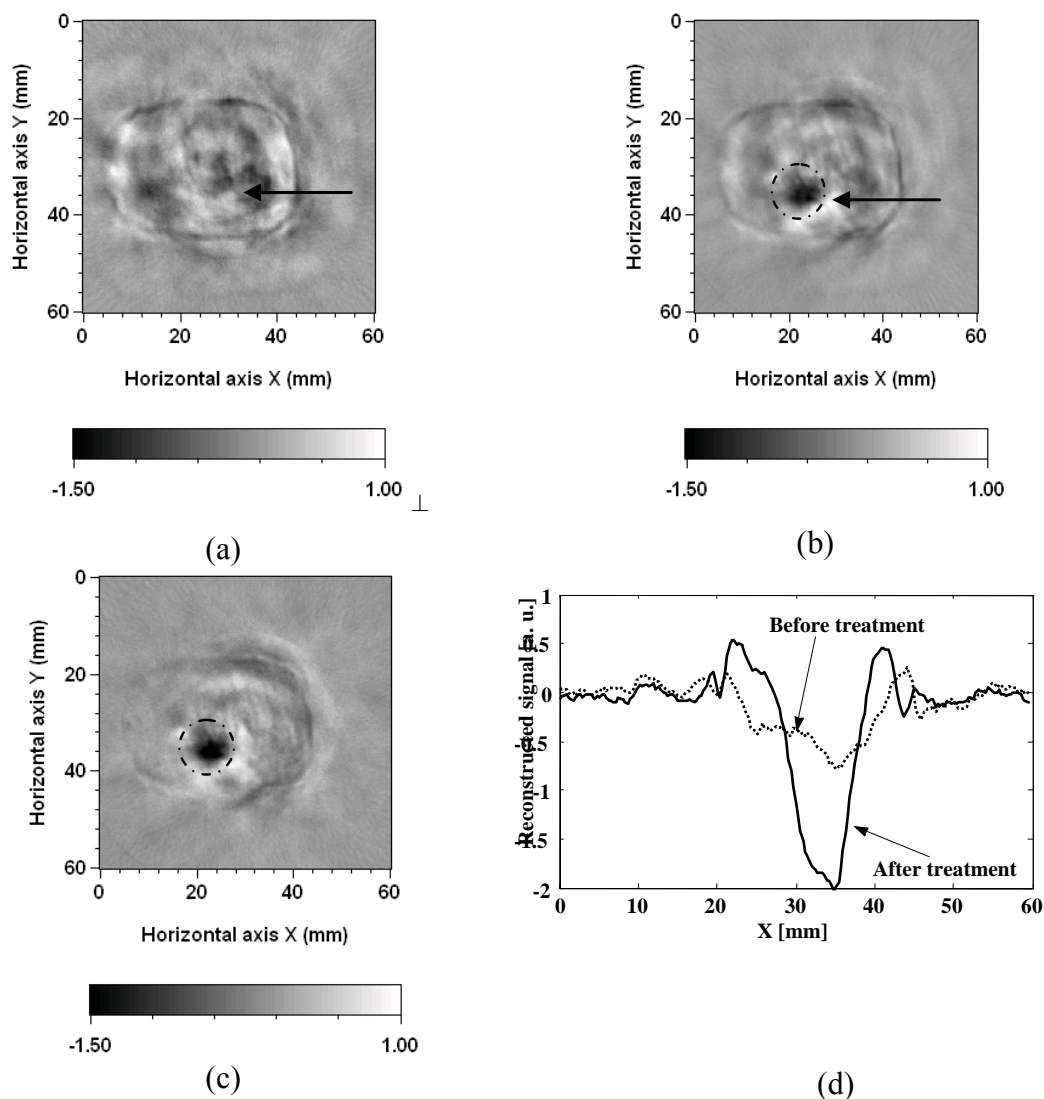


Fig. 3.6 Reconstructed image using local-tomography-type reconstruction method: (a) before heating; (b) after heating. (c) The differential image obtained by subtracting the data collected before heating from the data collected after heating. The lesion regions are indicated by dashed circles. (d) Reconstructed profile across the region at a depth shown by arrows in (a) and (b)

We reconstructed the image using the local-tomography-type reconstruction algorithm. Figure 3.6(a) is the reconstructed image before treatment, and Fig. 3.6(b) is the reconstructed image after treatment. These two images do not represent energy deposition directly, because most of the low-frequency components of the

thermoacoustic signals have been removed to emphasize the boundaries. We estimate that the ratio of the change in microwave absorption in the lesion region to the average absorption in the surrounding normal tissue was 0.85 in this case. In other similar experiments, the ratios ranged from 0.55 to 0.95. The lesion shown in the tissue photograph confirmed the corresponding regions measured by TAT. By subtracting the data collected before heating from the data collected after heating, but before reconstruction of the image, we obtained better image quality as shown in Fig. 3.6(c). Figure 3.6(d) compares two plots at the same depth shown in the reconstructed images before treatment and after treatment, as shown in Fig. 3.6(a) and (b). The lesion shown in the photograph confirmed the corresponding regions measured by TAT, and reconstructed image after subtraction has better image quality.

b) Evaluation and characterization of the lesion

In Fig. 3.7 we compare the sizes of the lesions measured from the TAT image with the sizes measured from the photograph. The lesion in the TAT image was evaluated as the area enclosed by the half maximum intensity contour of the lesion boundary. The lesion in the photograph was defined as the heated region (colored white). The scattered circles denote the results measured from TAT. The dash line shows the ideal regression of the scattered values. The solid line represents the fit using a weighted LS (least-squares) regression. The weights are the inverse of the lesion area measured in the photograph. The resulting regression equation relating the values from TAT (denoted by TAT) and the values from the photographs (denoted by Photo) is $[TAT] = 0.91 \times [Photo] + 3.67$. In

other words, the size evaluated from the TAT image was smaller than the size evaluated from the pathologic photograph. As the size of the lesion becomes larger, the discrepancy becomes more obvious. It has been shown that thermal damage is associated with an increase in the speed of sound.⁴¹ In the reconstruction process, we assumed a uniform ultrasound speed in the tissue sample without considering a change in ultrasound speed in the lesion region. This may partly explain why the size of the lesion measured from the TAT image was smaller than the size measured from the photograph. Further work that explicitly considers the difference in ultrasound speed between lesions and the surrounding tissue can potentially improve the accuracy of this method. Another important reason for the discrepancy is the limited resolution of our system, which can be improved by decreasing the microwave pulse width and increasing the bandwidth of the receiving ultrasonic transducer.

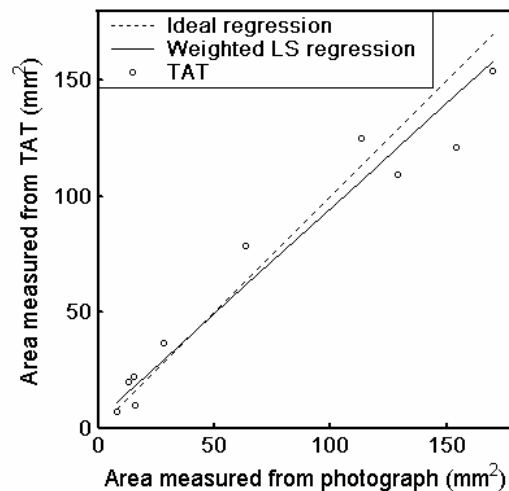


Fig. 3.7 Scatter plot of the area of the lesion evaluated using TAT vs. the area measured from pathologic photographs. The evaluation was applied to 10 lesions; the regression equation obtained using the weighted LS regression was $[TAT] = 0.91*[Photo] + 3.67$.

3.1.5 Discussion

Two problems that exist in our current imaging system are the nonuniformity of microwave distribution and the limited bandwidth of the receiving transducer. Both have great influence on the sample size used in the experiments and the resolution of the reconstructed images.

First, we consider the effects of the non-uniformity of microwave distribution on our final results. The pyramidal horn antenna used to irradiate microwave energy into the tissue sample is fed by a TE_{10} waveguide. The horn antenna is tapered gradually from the waveguide dimensions to a larger aperture so as to preserve the electric field distribution of the dominant mode in the open aperture. Neglecting the effects of the currents on the exterior surfaces of the horn antenna, the electric field at the aperture of the antenna can be approximated to have the same shape as the corresponding component of the TE_{10} mode. The electric field of the pyramidal horn near the aperture was estimated by $E_{\xi}(\eta, \xi) = E_{0,10} \sin\left(\frac{\pi\eta}{a}\right)$, where $E_{0,10}$ is the amplitude of the electric field of the TE_{10} mode, and a is the dimension of the horn aperture in the η direction. The η direction is chosen to be along the longer dimension, and the ξ direction is chosen to be along the shorter dimension. $E_{\xi}(\eta, \xi)$ depends on the η -coordinate and is independent of the ξ -coordinate (i.e., uniform in the ξ direction). The electric field reaches its maximum at the center of the longer side, and zero at both ends. More accurate values of the transient electric field radiated by the transmitting antenna in the

tissue sample can be computed by Finite-Difference Time Domain (FDTD) simulations. From the above analysis, we know that it is generally necessary to consider the microwave distribution in order to reconstruct an image of the tissue sample. In the current experiments, the tissue regions that we are interested in are very small compared with the antenna aperture, and we are only interested in the boundaries between different tissues. Therefore, it is safe to assume a relatively uniform distribution of microwave energy in the tissue sample. For large samples, however, this effect must be considered in order to achieve good image quality.

Next, we show the effects of the limited bandwidth of the receiving ultrasonic transducer on the received signals. The impulse response and the spectrum of the transducer are shown in Fig. 3.8(a) and (b). To illustrate the bandwidth-limited effects of the receiver, we numerically simulated the one-dimensional output piezo-electric signals of the thermoacoustic signals passing through the receiving transducer. In the simulations, we took into consideration the pulse width of the microwave pulse used in the experiments. Figure 3.8(c) is the temporal profile of the microwave pulse used in the experiments. Figure 3.8(e) shows the thermoacoustic signals induced by the microwave pulse. The simulation was carried on in one dimension, rather than in two, to simplify the computations although the results can be easily extended to two dimensions. The piezo-electric output of the ultrasonic transducer in response to the thermoacoustic pressure was calculated as the convolution between the thermoacoustic pressure and the impulse response of the transducer. Because of the band-limited effects of the transducer, we expected large changes at the boundary regions in the piezo-electric

output signal. The low-thermoacoustic pressure region in Fig. 3.8(d) was used to simulate the lesion. Figure 3.8(f) was the simulated piezo-electric output. We observed a deep drop in the piezo-electric signal at the lesion region. The recovery of the thermoacoustic signal through deconvolution is difficult to realize. As a reasonable simplification, in our analysis in the frequency range below 2 MHz, a differential operator was used to approximate the spectrum of the transducer.

Changes in the dielectric properties reflect HIFU-induced changes in the target region. Imaging techniques based on changes in the dielectric properties of tissue may be used to monitor the physiological changes during ultrasound treatment. Our experiments were implemented with a single ultrasonic transducer rotating in a circle to collect signals from different directions. Due to this limitation, we were unable to monitor changes in the tissue in real-time, and, consequently, changes in the dielectric properties during heating were not measured. Some research has shown that the dielectric properties of tissue increase at the initial denaturation of protein,⁵²⁻⁵⁴ which can be explained by an increased mobility of the bound water and ions. We expect stronger microwave absorption at the initial treatment. The cavitations during the treatment, however, may complicate real-time monitoring of HIFU treatments. In the future, the use of a transducer array will substantially reduce the data collection time and provide more information on the possibility of applying TAT to the real-time monitoring of HIFU treatments.

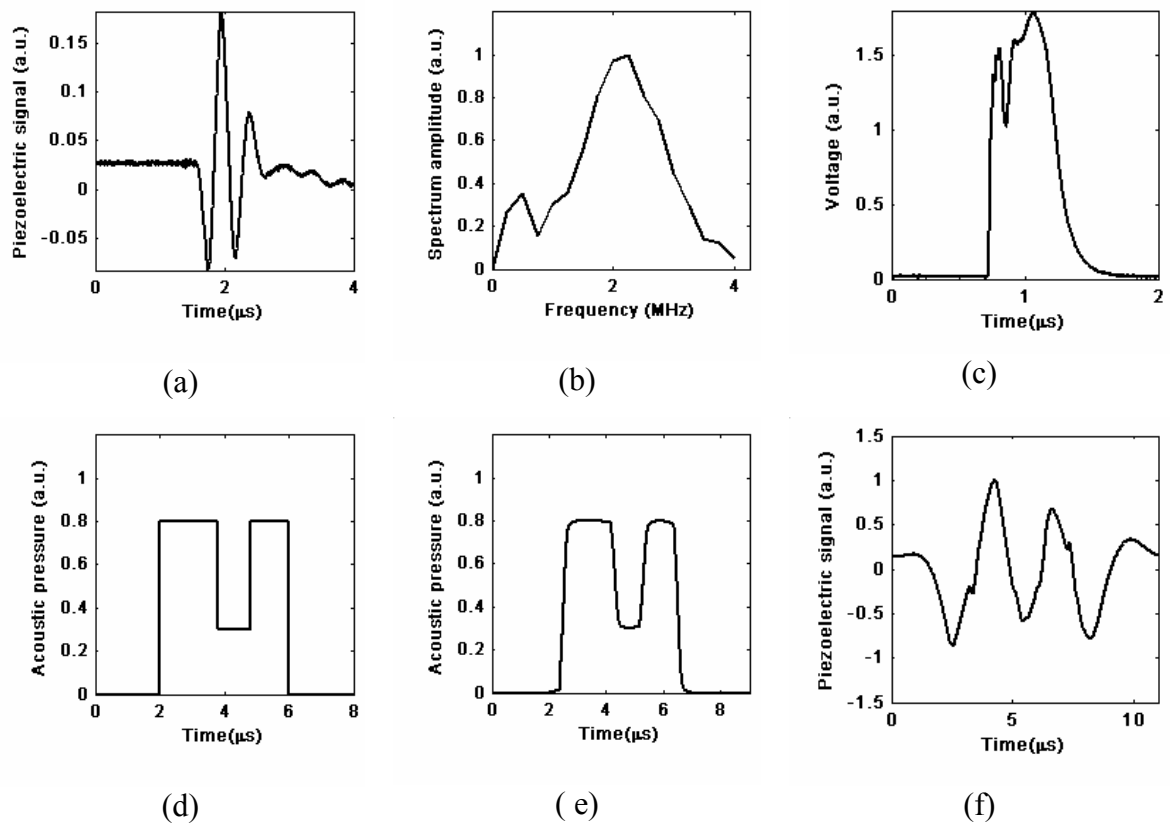


Fig. 3.8 Simulation of a piezo-electric signal in response to a microwave-induced thermoacoustic signal. (a) The temporal profile of the impulse response of the 2.25 MHz transducer. (b) Spectrum of the 2.25 MHz ultrasonic transducer. (c) Temporal profile of the microwave pulse used in the simulations. (d) Thermoacoustic signals induced by an ideal microwave pulse for a sample with a low microwave absorption region in the center. (e) Thermoacoustic signals induced by microwave pulses used in the experiments for the same samples used in (d). (f) Simulated piezo-electric signals of the 2.25 MHz ultrasonic transducer for (e).

The treatment of discrete tumors is a difficult clinical problem. When the contrast in water content between cancerous and normal tissue is large, the difference in microwave absorption is also large. Thermoacoustic tomography has been shown to be capable of detecting small tumors based on this difference in microwave absorption.²⁹ We have demonstrated that TAT can, in addition, differentiate the tumor before and after

treatment. Moreover, high-intensity focused ultrasound has been shown to be a noninvasive treatment that can induce well-defined coagulated lesions while leaving the surrounding area unaffected. The size and shape of the target region can be well controlled to focus on the individual tumor. The prospect of combining these two techniques in order to both detect tumors and apply thermal surgery during the same clinical event holds great promise for cancer treatment in the future.

3.1.6 Conclusions

HIFU-induced lesions in porcine muscle were imaged with TAT. Tissue thermal-damage can result in a localized change in a tissue's electromagnetic properties, and thus its ability to absorb microwave energy. Our preliminary results have shown that TAT has the capacity to visualize HIFU-induced lesions with good contrast using a local-tomography-type reconstruction algorithm. The boundaries of different tissues can be imaged clearly. The size and position of lesions measured from TAT images were compared with the size and position of those measured from gross pathologic photographs. It was established that TAT can estimate the size of lesions effectively. From the preliminary studies conducted here, we conclude that TAT has the potential to provide an effective, low-cost alternative method for imaging HIFU-induced lesions.

3.2 Clinical breast cancer imaging

3.2.1 Introduction

The American Cancer Society reports that breast cancer is the second overall leading cause of death among woman in the United States. X-ray mammography and ultrasonography are current clinical tools for breast cancer screening and detection. Mammography, however, uses ionizing radiation, and is not safe to frequent use. Moreover, radiographically dense breast still remains a challenge for X-ray mammography. Currently, ultrasonography is used as adjunct tool for X-ray mammography. It tends to miss non-palpable tumors due to its intrinsic limitations. Because malignant tissue and normal tissue differs in their dielectric properties, here we investigate the feasibility of using our 3 GHz TAT system for clinical breast cancer imaging at M. D. Anderson cancer center.

3.2.2 Experiment and results

The data were collected by using four ultrasonic transducers as the receiver. Channels 1 and 4 were two focused ultrasonic transducers with central frequencies at 1 MHz and 3.5 MHz, respectively. Channels 2 and 3 were two unfocused ultrasonic transducers with central frequencies at 1 MHz and 2.25 MHz, respectively. The depth of the tumor in the vertical direction was estimated by ultrasonography. The TAT image was obtained in the horizontal plane. The vertical depth of the four transducers had been adjusted to be

around the location of the tumor to get a better coverage. After the surgery, the mastectomy specimen was placed into a plastic container and bathed in mineral oil. A vacuum pump was used to remove the air between the tissue sample and the container wall. The diameter of the breast tissue sample in the imaging plane was approximately 11 cm. The thickness of the tissue sample was approximately 9 cm. The transducers scanned clockwise in a circle. The rotation step was 1.5° . We averaged the signals at each step to obtain a better signal-to-noise ratio.

The TAT images were reconstructed using a modified backprojection method. Strong image contrasts were observed in the tumor regions for all the channels with consistency of position and shape. The reconstructed images from the two focused transducers (channel 1 and channel 4) provided better signal-to-noise ratios. The TAT image of Channel 1 (1 MHz, focused) is shown in Fig. 3.9(a). An object (presumably the tumor) in the TAT image has been identified as the strong-signal (bright colored) region, which is located in the 3 o'clock position (12 o'clock and 3 o'clock are marked in Fig. 3.9 (a)). Two gray arrows show the tumor region in the TAT image. The average tumor-to-background contrast was estimated to be over 5. Figure 3.9(b) shows a one-dimensional plot across the tumor region denoted by the two dashed gray arrows in Fig. 3.9 (a). The size of the tumor was approximately $16 \text{ mm} \times 20 \text{ mm}$. The dark ring in the reconstructed image came from the system interference. Figure 3.9(c) shows preoperative sonogram of the breast shows an ill-defined tumor, which later proved to be infiltrating lobular carcinoma at pathologic examination. The transverse dimension of the lesion measures 2.7 cm as marked by the two + calipers, which verifies the

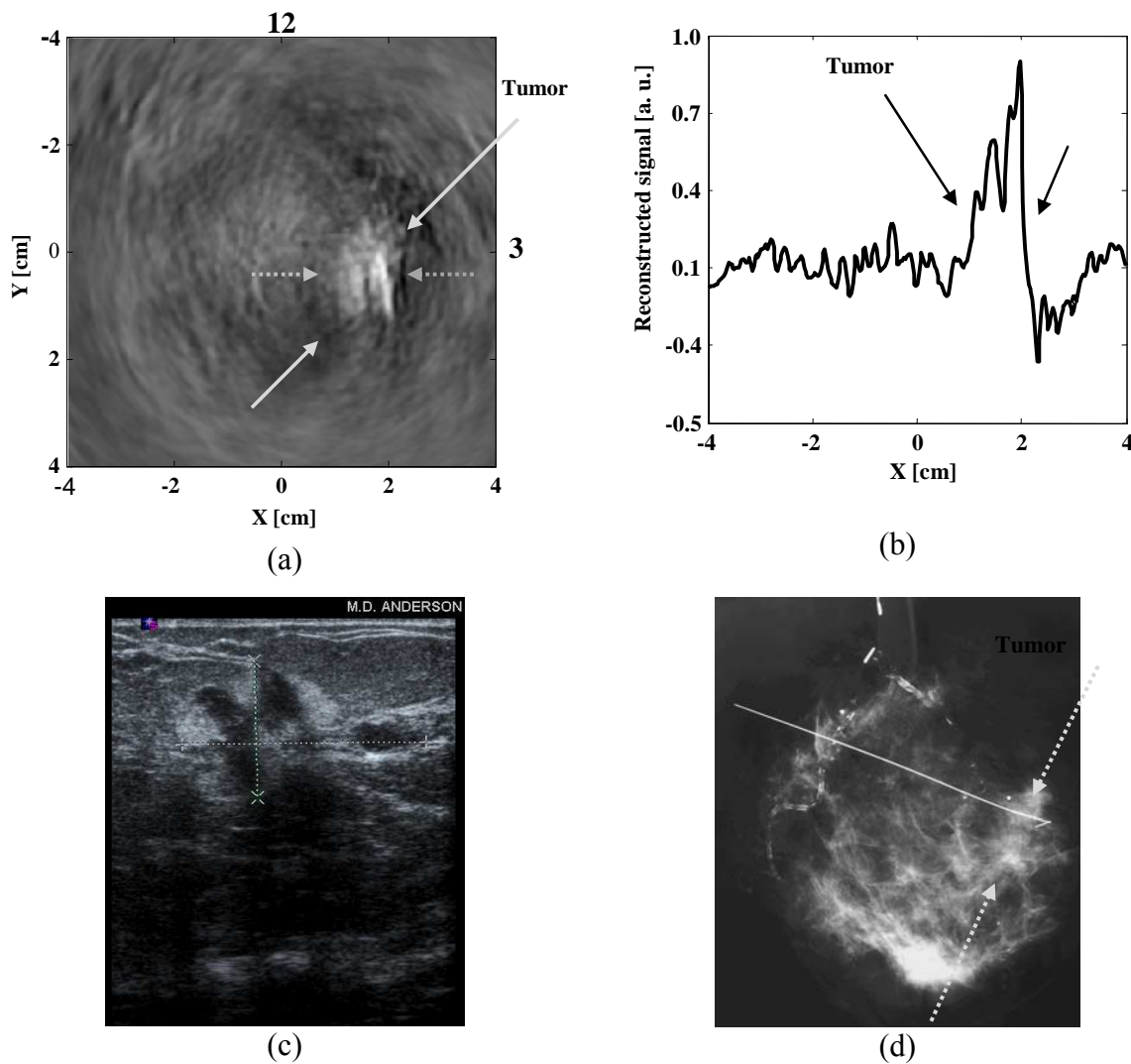


Fig. 3.9 (a) TAT image of the mastectomy specimen. The tumor region has been identified as the region denoted by the two solid gray arrows; (b) Line profile across the tumor region indicated by the two dashed gray arrows in (a); (c) Preoperative sonogram; (d) Digital radiograph of the mastectomy specimen

measurements from TAT image. The anteroposterior dimension of the lesion measures 1.5 cm as marked by the two x-shape calipers. Digital radiograph of the mastectomy specimen is shown in Fig. 3.9(d), in which the white line is a localizing wire placed into

the lesion (arrows) under real-time ultrasound guidance, and the tumor is marked by two dashed gray arrows. The digital radiograph further verifies the location of tumor obtained by TAT. In this experiment, TAT obtained better image contrast than the other two imaging modalities.

Same as in the previous experiment, four ultrasonic transducers were used for get a better coverage of the tumor region. The diameter of the breast tissue sample in the imaging plane was around 17 cm, which was about 1.5 times bigger than in the previous experiment. The thickness of the tissue sample was around 4 cm. The scanning step is 2.25° . At each step, the thermoacoustic signals were averaged. An irregular region with strong thermoacoustic signal is observed in the TAT images from all three channels with consistency of position and shape. Same as in previous experiment, the two cylindrically focused transducers (channel 1 and channel 2) gave better signal-to-noise ratio. The TAT image detected by channel 2 (2.25 MHz, cylindrically focused, located 18 mm above the bottom of the container) is shown in Fig. 3.10(a), and 12 o'clock and 3 o'clock are marked. From our results, an object (presumably the tumor) in the TAT image has been identified as the strong-signal (bright colored) region, which is located around the center of the image. Four gray arrows show the tumor region in the TAT image. The average tumor-to-background contrast is estimated to be around 4~5. A one-dimensional plot across the tumor region shown by the two arrows is also shown in Fig. 3.10(b). The diameter of the tumor is estimated to be around 3 cm. The signal-to-noise ratio is weaker than in the previous experiment.

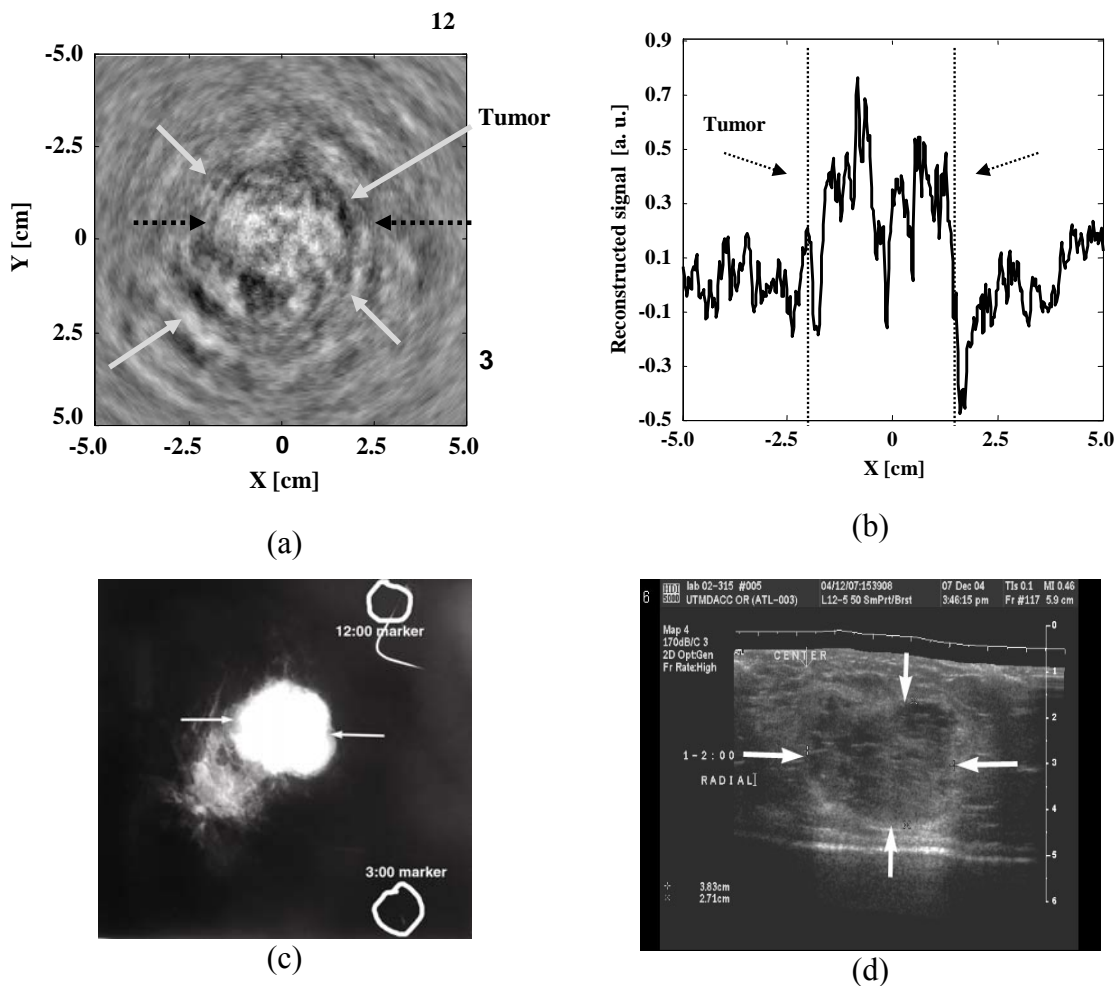


Fig. 3.10 (a) Thermoacoustic image of the excised whole breast (mastectomy specimen). The tumor region is indicated by the gray arrows. 12 o'clock and 3 o'clock are marked. (b) Line profile across the tumor region indicated by the two black arrows in (a). (c) Digital radiograph of the mastectomy specimen. 12 o'clock and 3 o'clock are marked. (d) Postoperative sonogram of the breast.

This may be because of the larger scanning radius used in this experiment, so that the microwave-induced ultrasonic signals had to pass a longer propagation path to reach the ultrasonic transducers and therefore suffered more attenuation. Figure 3.10(c) shows the digital radiograph of the mastectomy specimen. 12 o'clock and 3 o'clock are marked. Figure 3.10(d) is the postoperative sonogram of the breast. The lesion measures $\sim 27 \text{ mm} \times 38 \text{ mm}$ from sonogram, which is close to the value obtained from TAT image.

In both of two experiments, the image contrasts obtained by TAT are much better than those obtained by ultrasonography. In the first experiment, in which a radiographically denser breast was imaged, TAT obtained better image contrast than that of X-ray mammography. The geometric information obtained with TAT was confirmed by both sonogram and radiograph. Those clinical results verify that TAT has the potential to be used as a new clinical screening tool for breast cancer imaging.

3.3 Other potential applications

Other potential applications for TAT may include joint imaging for monitoring inflammatory arthritis. The increase of synovial fluid is one of the earliest pathologic changes in many inflammatory joint disease. An important substance present in articular cartilage and synovial fluid is called hyaluronic acid, which can help joint hold water.^{55,56} Injection of hyaluronic acid is also a method to treat inflammation.⁵⁷ In a previous research, laser-based photoacoustic tomography was proposed to image finger joints.⁵⁸ Microwave-induced TAT has deep penetration depth in biological tissue as well as high sensitivity to water content, ionic concentration; it may be used to image bigger joints than that has been done by laser-based photoacoustic tomography.

4. THE EFFECTS OF ACOUSTIC HETEROGENEITIES IN WEAKLY REFRACTIVE MEDIUM*

4.1 Introduction

In the previous section, it is shown that TAT has the potential to be used in breast cancer detection. Existing reconstruction algorithms for TAT is based on the assumption of homogeneous acoustic speed in biological tissue, an approximation that is only partially valid in clinical application. From breast imaging with TAT, we have learned that different components of the breast, such as the glandular tissues, stromal tissues, cancerous tissues and other fatty tissues, have different acoustic properties.³² The variations between their acoustic speeds can be as great as 10%. The acoustic speed in subcutaneous fat is between 1400 m/s and 1450 m/s, whereas the acoustic speed in normal parenchyma and stromal tissue is between 1500 m/s and 1560 m/s.

Acoustic speed variations have two effects on TAT images based on the homogeneous-speed assumption. The first effect is the displacement of thermoacoustic signals radially, i.e., along the assumed linear radiating propagation paths of a thermoacoustic signal, due to an incorrect acoustic speed being assumed in calculating the positions of targets along the path. The second effect is the displacement of

*Reprinted with permission from “Thermoacoustic tomography with correction for acoustic speed variations (www.iop.org/EJ/abstract/0031-9155/51/24/010)” by X. Jin and L.-H. Wang, 2006. *Phys. Med. Biol.* 51, 6437-6448 Copyright [2006] by IOP Publishing Limited. www.iop.org/journals/pmb.

thermoacoustic signals tangentially due to the ultrasonic refraction away from the assumed straight path. In existing reconstruction algorithms, the recorded acoustic signals from a given viewing angle are backprojected to the imaging region without position correction. Therefore, the backprojected signals from a given detection position are misplaced in the reconstructed image and subsequently added imprecisely to the backprojected signals obtained from other detection positions. This causes both blurring and displacement in the reconstructed image and reduces the contrast. Consequently, the ability of TAT to detect small tumors is compromised.

A numerical study showed that the effects of acoustic heterogeneities on TAT can be reduced by using an acoustic speed distribution,⁵⁹ which is measured independently of TAT. To this end, we use ultrasonic transmission tomography (UTT) to quantitatively measure the acoustic speed distribution in the tissue. UTT is implemented by time-of-flight measurements,⁶⁰⁻⁶³ and it is compatible with our TAT system. Since UTT reveals mechanical contrast, the image quality of UTT alone is insufficient for early-stage tumor detection. The deterioration of the image quality due to ultrasonic attenuation and refraction is less obvious in TAT than in UTT, because in TAT the ultrasonic wave propagates one way only and the central frequency of the generated thermoacoustic waves is lower (around 1 MHz).

In this section, we analyze the effects of acoustic speed variations on TAT imaging and then propose a compensation method based on UTT to correct for these effects. We show that the acoustic speed distributions obtained from UTT can be used to improve the image quality of TAT in weakly refractive tissue. Numerical simulations

and phantom experiments are presented to verify the effectiveness of the proposed method.

4.2 Effects of acoustic heterogeneities on TAT in weakly refractive medium

Assume the number of heterogeneities in the breast is limited, when the sizes of the heterogeneities are comparable to or smaller than the wavelength, diffractive phenomena dominate over refractive effects, amplitude distortion of the wavefront is trivial if we placed the detectors in the far field of the heterogeneities. When the sizes of the heterogeneities are greater than a wavelength, by using ray theory (geometric propagation) we will show that refraction-induced multipath interference is minimal; consequently, no severe amplitude distortion as those found in ultrasound tomography occurs. Furthermore, the effects of the phase distortion can be evaluated through the variations in the time-of-flight for weakly refractive medium.

4.2.1 Amplitude distortion of the wavefront

Here we only consider large-scale heterogeneities in the following analysis. Amplitude distortion induced by wave refraction is our primary concern. Refraction occurs when there are acoustic speed variations between different tissues; hence thermoacoustic waves will propagate through a path departed from the assumed straight path. In this case multipath interferences occur and induce amplitude distortion. The effects of acoustic heterogeneities on breast TAT has been studied with simulated data,⁵⁹ in which the theoretical analyses are based on an assumption that breast parenchyma is acoustic

homogeneous. Under this assumption, we only need to consider the refraction effects at the interface between the breast parenchyma and subcutaneous fat while the refraction effects at the boundary between the mineral oil and subcutaneous fat is neglected due to the small difference in their acoustic speed variations.

For convex interface, it can be proved that there are no refraction-induced multipath interferences and consequently amplitude distortion due to refraction can be ignored for this case.⁵⁹ This conclusion also can be applied to a boundary with wavelength-scale concave segment. This kind of boundary can be treated as a convex boundary approximately because the effects of the small concave segment can be neglected when the detectors are placed in the far field of the segments.

For concave or irregular interfaces, if the interference is non-focusing type, which means the interference of short transient pulses from the same source propagating through different paths with different time-of-flights, because travel time along different ray paths varies, we can differentiate them in time axis if their individual arrival times do no overlap each other and the difference between their travel times is larger than the average pulse-width of thermoacoustic signals. For focusing-type interference, when the interface segment is much larger than a wavelength, strong amplitude distortion can be minimized by placing the detector within the far field of the heterogeneities for a wavelength-scale boundary segment.⁵⁹ It is not necessary to apply the inequality when ultrasound waves has a frequency range below 0.5 MHz, because ultrasound scattering by soft tissue is small and thus no severe amplitude distortion due to scattering.

In real applications, breast parenchyma can be acoustic heterogeneous.⁶⁴ The refraction may occur at several interfaces, either convex or concave. As the neighboring rays propagate through the heterogeneous medium, they may intersect at some field point. But for the weakly refractive medium considered in this study, the amplitude distortion due to multipath interferences is trivial as compared with amplitude distortion induced by phase shift. We will neglect the effects of multipath interferences in the following analysis.

4.2.2 Phase distortion of the wavefront

Phase distortion can be brought by wave refraction and acoustic speed variations. In weakly refractive medium, we will show that refraction-induced phase distortion can be approximated with the phase shift along a straight ray path, thus the effects of phase distortion on TAT is only determined by the displacement of thermoacoustic signals axially, i.e., along the assumed linear radiating propagation paths of a thermoacoustic signal, due to an incorrect acoustic speed being assumed in calculating the positions of targets along the path. This is important because if we don't consider the phase shift of received thermoacoustic signals in reconstruction algorithms, the recorded acoustic signals from a given viewing angle can be backprojected to the imaging region without position correction. Therefore, the backprojected signals from a given detection position are misplaced in the reconstructed image and subsequently added imprecisely to the backprojected signals obtained from other detection positions.

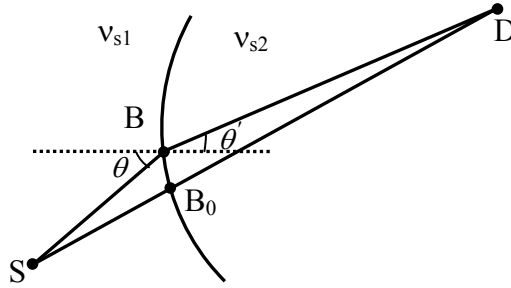


Fig. 4.1 Ray refraction at the boundary between two different tissues

By the assumption that the medium is of weakly refractive, the beam widening can be ignored. The wave refraction at the boundary is shown in Fig. 4.1. The following results are true for both concave and convex boundaries. The total travel time of an acoustic signal is given by the integral of the inverse of the acoustic speed in the tissue along the ray path:

$$T = \int_{l(\mathbf{r})} \frac{1}{c(\mathbf{r})} dl \quad (4.1)$$

where $c(\mathbf{r})$ is the acoustic speed distribution in the tissue and $l(\mathbf{r})$ is the ray path. Define $\varepsilon = \max_{\mathbf{r}} |(c(\mathbf{r}) - c_0)/c_0|$, where c_0 denotes the acoustic speed of the homogenous reference medium. For weakly refractive medium, ε is a small value. Although the total length of the refractive path is longer than that of the straight line, the refractive path has a longer length in the higher acoustic speed region and a shorter path in the lower acoustic speed region. This results in the cancellation of the first-order term of ε , thus we only have second-order term of ε . It can be proved that⁵⁹

$$\frac{|T_2 - T_1|}{|T_1 - T_0|} = o(\varepsilon) \quad (4.2)$$

where T_1 be the time of flight along the refracted path l_{SD} , T_2 be the time of flight along the straight path l_{SD} without considering refractive effects, and T_0 be the time of flight along l_{SD} by assuming constant acoustic speed in the medium. Therefore, the error by neglecting the refractive effects is small; we can neglect refractive effects and only calculate the time shift along the straight ray path. In more general cases the ray may pass through several interfaces, the above derivation is still true. Therefore the correction of acoustic heterogeneities on TAT has been simplified to the problem of correcting the phase shift induced by acoustic speed variations along straight ray paths. In the following analysis, we assume acoustic speed variations along the ray path dominating the phase shift in weakly refractive medium; therefore we will only correct the image distortion and blurring induced by the phase shift along the straight ray paths.

4.3 Theoretical basics and methods

4.3.1 Measurement of the speed-of-sound distribution

To correct for the effects of acoustic speed heterogeneities, we need to measure the acoustic speed distribution. In this preliminary research, the measurement of two-dimensional acoustic speed distributions is achieved by UTT. The relationship between the speed-of-sound image and measurements obtained for UTT will be explained.

In UTT, the acoustic speed in biological tissue can be calculated from the arrival times of ultrasonic waves. The total travel time T can be measured from the recorded ultrasonic signals. The time-of-flight measurement for a specific projection line is computed by a cross-correlation operation between the signals from the ultrasonic transmitter and the signals from the ultrasonic receiver. The location of the maximum of the cross-correlation represents the time-of-flight of the ultrasonic wave in the tissue. Since $l(\mathbf{r})$ depends on $c(\mathbf{r})$, the relationship between T and $1/c(\mathbf{r})$ is nonlinear in general. Below, we linearize this problem.

The travel-time perturbation δT is defined as

$$\delta T = T - T_0 \quad (4.3)$$

A homogenous reference medium is used to measure T_0 . The travel times are considered stationary here.^{65,66} For weakly refractive tissues, we linearize $l(\mathbf{r})$ to the reference ray in the homogenous reference medium, $l(\mathbf{r}_0)$, which is independent of $c(\mathbf{r})$. As a result, we have

$$\delta T = \int_{l(\mathbf{r}_0)} \left(\frac{1}{c(\mathbf{r})} - \frac{1}{c_0} \right) dl \quad (4.4)$$

The integration is now taken over $l(\mathbf{r}_0)$. Since $l(\mathbf{r}_0)$ is assumed to be straight, the above equation represents a linear relationship between δT and the difference in the inverse of the acoustic speed and is a form of the Radon transform. This equation sets up the relationship between the acoustic speed distribution in the tissue and the measurements obtained from UTT. Of course, Equation (4.4) is valid only for weakly refractive tissue.

If strong bending of ultrasonic rays occurs as they cross strongly refractive tissue, Eq. (4.4) is no longer valid.

To implement UTT based on Eq. (4.4), we divide the two-dimensional imaging area into cells and assume that $c(\mathbf{r})$ remains constant in each cell. For viewing angle i , we let l_{ij} be the length of the path that the ultrasound pulse transverses through cell j .

The discretized form of Eq. (4.4) is then written as

$$\delta T_i = \sum_j l_{ij} \left(\frac{1}{c_j} - \frac{1}{c_0} \right) \quad (4.5)$$

where c_j is the acoustic speed in cell j . The nonlinear problem in Eq. (4.2) has been simplified to a system of linear equations. To solve Eq. (4.5) for the acoustic speed distribution in the tissue, we simply perform a linear inversion using a filtered back-projection method.⁶⁷

4.3.2 Effects of acoustic speed variations on TAT and the correction method

The propagation of thermoacoustic waves is governed by the following partial differential equation:^{68,69}

$$\nabla^2 p(\mathbf{r}, t) - \frac{1}{c^2(\mathbf{r})} \frac{\partial^2 p(\mathbf{r}, t)}{\partial t^2} = -\frac{\beta}{C_p} \frac{\partial H(\mathbf{r}, t)}{\partial t} \quad (4.6)$$

Here, β is the volume thermal expansion coefficient; C_p is the specific heat; $p(\mathbf{r}, t)$ is the measured pressure at a certain position and time; $c(\mathbf{r})$ is the acoustic speed distribution in the tissue, and $H(\mathbf{r}, t)$ is the thermal deposition function at a certain

position and time. The thermal deposition function can be written as the product of a spatial energy deposition function and a microwave pulse function $H(\mathbf{r}, t) = \varphi(\mathbf{r}) \cdot I(t)$, where $\varphi(\mathbf{r})$ denotes the energy deposition in the tissue, and $I(t)$ denotes the microwave pulse function.

By assuming $I(t) = \delta(t)$ (Dirac delta function), and performing a Fourier transform with respect to t on both sides of the equation, we obtain

$$\left(\nabla^2 + \frac{\omega^2}{c^2(\mathbf{r})} \right) \tilde{p}(\mathbf{r}, \omega) = -i\omega \frac{\beta}{C_p} \cdot \varphi(\mathbf{r}) \quad (4.7)$$

where ω is the angular frequency, $\tilde{p}(\mathbf{r}, \omega)$ is the Fourier transform of $p(\mathbf{r}, t)$ with respect to t , and $\tilde{p}(\mathbf{r}, \omega) = \int_{-\infty}^{\infty} p(\mathbf{r}, t) \cdot \exp(-i\omega t) dt$.

In an acoustically homogeneous medium, we have $c(\mathbf{r}) = c$ (constant). For spherical detection geometry, $p(\mathbf{r}, t)$ can be solved by using the Green's-function approach:

$$p(\mathbf{r}, t) = \frac{c\beta}{4\pi C_p} \frac{\partial}{\partial t} \oint_{t=|\mathbf{r}-\mathbf{r}'|/c} \frac{\varphi(\mathbf{r}')}{|\mathbf{r}-\mathbf{r}'|} d\mathbf{r}' \quad (4.8)$$

The integration, representing the forward problem, is performed on a spherical surface. The associated inverse problem has been investigated by many researchers. The back-projection solutions for different detection geometries can be found in literatures.^{50,51} In our experiment, a circularly scanning detection geometry is used. An approximate back-projection solution for this 2-D detection geometry in the time domain can be written as:⁵⁰

$$\varphi(\mathbf{r}') \approx \frac{C_p}{c^2 \beta} \int d\theta \left. \frac{\partial p(\mathbf{r}, t)}{\partial t} \right|_{t=|\mathbf{r}-\mathbf{r}'|/c} \quad (4.9)$$

The integration is performed over all of the scanning angles.

In an acoustically inhomogeneous medium, numerical methods based on linear approximations are used to provide the inverse solution for TAT. For weakly refractive tissue, the time profile of the thermoacoustic wave is dominated by the first-order acoustic speed component, and the distortion of the time profile of the thermoacoustic wave is mainly determined by the first-order perturbation. By contrast, higher-order acoustic speed components determine the spatial distribution of the ultrasonic waves. Here, we neglect the high-order acoustic speed components and only implement axial acoustic corrections here. The received thermoacoustic wave can, therefore, be approximately modeled by the following integral over a perturbed sphere:

$$p(\mathbf{r}, t) \approx \frac{c\beta}{4\pi C_p} \frac{\partial}{\partial t} \oint_{\tilde{S}} \frac{\varphi(\mathbf{r}'')}{|\mathbf{r}-\mathbf{r}''|} d\mathbf{r}'' \quad (4.10)$$

where \tilde{S} is a curved surface on which every point source has the same time-of-flight to the receiver, and \mathbf{r}'' denotes the position of a point source on \tilde{S} .

The problem then becomes finding $\varphi(\mathbf{r})$ by minimizing $\|L_\varphi(\mathbf{r}, t) - \hat{p}(\mathbf{r}, t)\|$. Here, $\hat{p}(\mathbf{r}, t)$ is the measured pressure (projection data); L_φ is a linear operator that consists of a summation on \tilde{S} followed by a time differentiation in the time-domain:

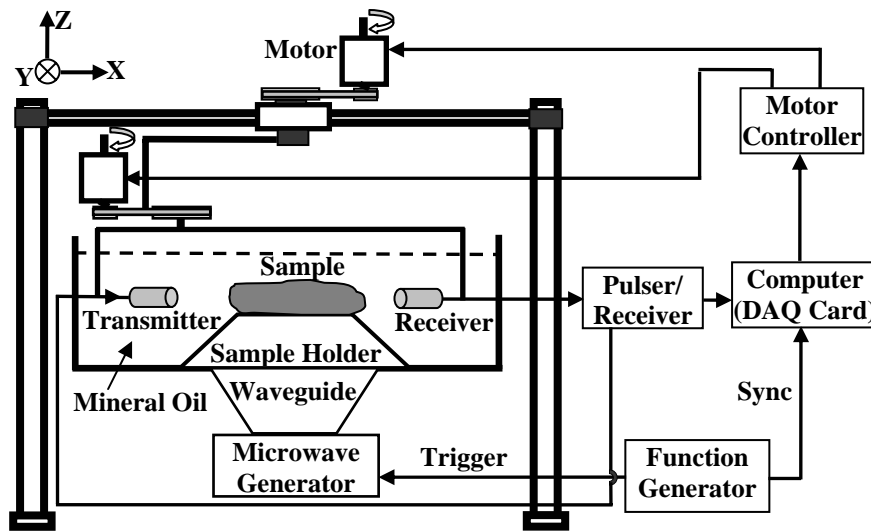
$$L_\varphi(\mathbf{r}, t) := \eta_0 \cdot \frac{\partial}{\partial t} \oint_{\tilde{S}} \frac{\varphi(\mathbf{r}'')}{|\mathbf{r}-\mathbf{r}''|} d\mathbf{r}'' \quad (4.11)$$

where η_0 is a constant. In 2-D, the integration is performed along a perturbed circle. Here, we use LSQR to solve the optimization problem, where LSQR is a least-squares method that uses an iterative approach to generate a sequence of approximations so that the residual norm decreases monotonically.⁷⁰ This method depends on the initial estimate of the energy deposition, which is obtained from the constant-speed model.

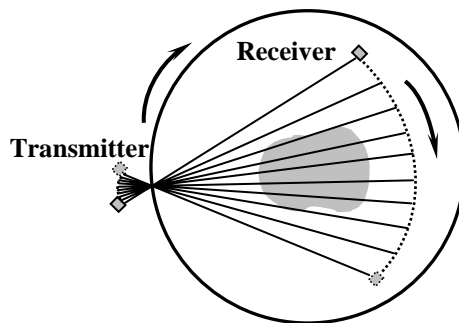
LSQR is selected for its robustness. The algorithm is summarized as follows:

- 1) The acoustic speed distribution is calculated from the time-of-flight measurements obtained by UTT through a filtered back-projection method. The acoustic speeds at specific locations are obtained using bilinear interpolation.
- 2) An initial estimate of the energy deposition $\varphi(\mathbf{r})$ is made from the measurements of projection data $\hat{p}(\mathbf{r}, t)$ by using Eq. (4.9).
- 3) An iterative least-squares method based on LSQR is used to solve $\|L_\varphi(\mathbf{r}, t) - \hat{p}(\mathbf{r}, t)\|$. The iteration stops when either the maximum number of iterations has been reached or the corresponding criterion for the convergence is satisfied.

4.4 Experimental system



(a)



(b)

Fig. 4.2 Experimental setup and the scanning geometry: (a) Experimental setup for the combined TAT/UTT imaging system and (b) Schematic of the scanning geometry in top view. In UTT, the transmitter sent pulsed ultrasonic signals, and the receiver on the opposite side of the transmitter received the ultrasonic pulses. In TAT, the transmitter used in UTT was used as the receiver, which circularly scanned the tissue sample.

An experimental system was constructed based on our current TAT setup to obtain both speed-of-sound and TAT images. The combined TAT/UTT setup is schematically shown in Fig. 4.2(a), and the scanning geometry is shown in Fig. 4.2(b). The scanning system consisted of two single-element unfocused 2.25 MHz ultrasonic transducers (Panametrics Inc., V323) that were approximately 6 mm in diameter with a 6 dB bandwidth of approximately 65%. The to-be-measured samples were immersed in mineral oil, which was used as the acoustic coupling medium in the experiments.

For UTT, two unfocused ultrasonic transducers were required. One was used to transmit the ultrasonic pulses and the other, on the opposite side of the transmitter, was used to receive the pulses. Image reconstruction required fan-beam scanning as well as circular scanning of the two transducers. Both the transmitting and receiving transducers were mounted on a mechanical arm that was driven by two stepping motors to scan the tissue sample submerged in mineral oil. The mechanical arm first scanned in a fan-beam fashion to cover the target region of a 67.5° fan-beam angle at each projection angle in 120 steps by a stepping motor. Then, the two ultrasonic transducers at the positions along the center axis of the fan beam were rotated circularly in the imaging plane with a step size of 2.25° by a second stepping motor. A pulser-receiver (PR 5072, Panametrics Inc.) was used to transmit and to receive the ultrasound pulses. The data were collected by using a PC-based data acquisition card (CS14200, Gage Inc.). The time-of-flight measurements of the transmitted pulses were made using the cross-correlation method. An acoustic speed image was then reconstructed using a filtered back-projection method

on a 200×200 grid. The speed-of-sound images were subsequently used to correct distortion and blurring in the TAT images of the same target.

For TAT, because the thermoacoustic waves were induced by electromagnetic radiation, we did not need an ultrasonic transducer as a transmitter. Either one of the two transducers could be used as the detector for the generated thermoacoustic signals. The central frequency of the microwave pulse was 3 GHz; the peak power was around 10 KW; and the pulse width was 0.5 μ s. The average energy per pulse was calculated to be about 5 mJ. The received thermoacoustic signals were amplified by the ultrasonic amplifier and then sampled by the data acquisition board. At each scan position, 150 measurements were averaged.

The UTT data were collected first, and then the TAT measurements were recorded. We performed phantom experiments on the same tissue sample using both UTT and TAT. The TAT image without acoustic speed compensation was reconstructed by using a modified back-projection method. The TAT image with acoustic speed compensation was reconstructed by using the method discussed in the previous section.

4.5 Results and discussion

We first used numerical simulations to demonstrate the distortion and blurring of small absorbers caused by acoustic speed variations in TAT images. Then, we used the method discussed in the previous section to compensate for the distortion and blurring in the simulated data. The compensation method was further verified by using a phantom

experiment. In the following discussion, we assume refraction effects are relatively weak in the tissue.

Usually we can optimize TAT images by simply adjusting the average acoustic speed in the tissue while assuming the medium is acoustically homogeneous. The image quality of TAT, however, is limited when the acoustic speed variations are no longer negligible compared with the average acoustic speed. Figure 4.3 shows a numerical example of the distortion and blurring brought about by acoustic speed heterogeneities. A strong small microwave absorber was surrounded by acoustically heterogeneous tissue. The object function for TAT is shown in Fig. 4.3(a), while the object (speed-of-sound) function for UTT is shown in Fig. 4.3(b). To make the simulation results closer to the real situation, in the computation we added 2% Gaussian noise in the object function (speed-of-sound) for UTT. Part of the waves generated by the small absorber passed through the acoustically heterogeneous tissue. If we assume constant acoustic speed in the tissue, the time-of-flight error deteriorates the strength of the reconstructed absorber because the back-projection registers the thermoacoustic signals at incorrect positions. To illustrate the effects more clearly, we show a close-up TAT image of the small absorber, marked by the white dotted square in Fig. 4.3(a). The small absorber appears as a crescent-like object in Fig. 4.3(c), which has low spatial resolution. By adjusting the average acoustic speed, we can get a sharp boundary for either the big absorber or the small absorber, but not for both. Figure 4.3(d) shows that the distortion has been alleviated by the proposed correction method using the speed-of-sound distribution in the same sample.

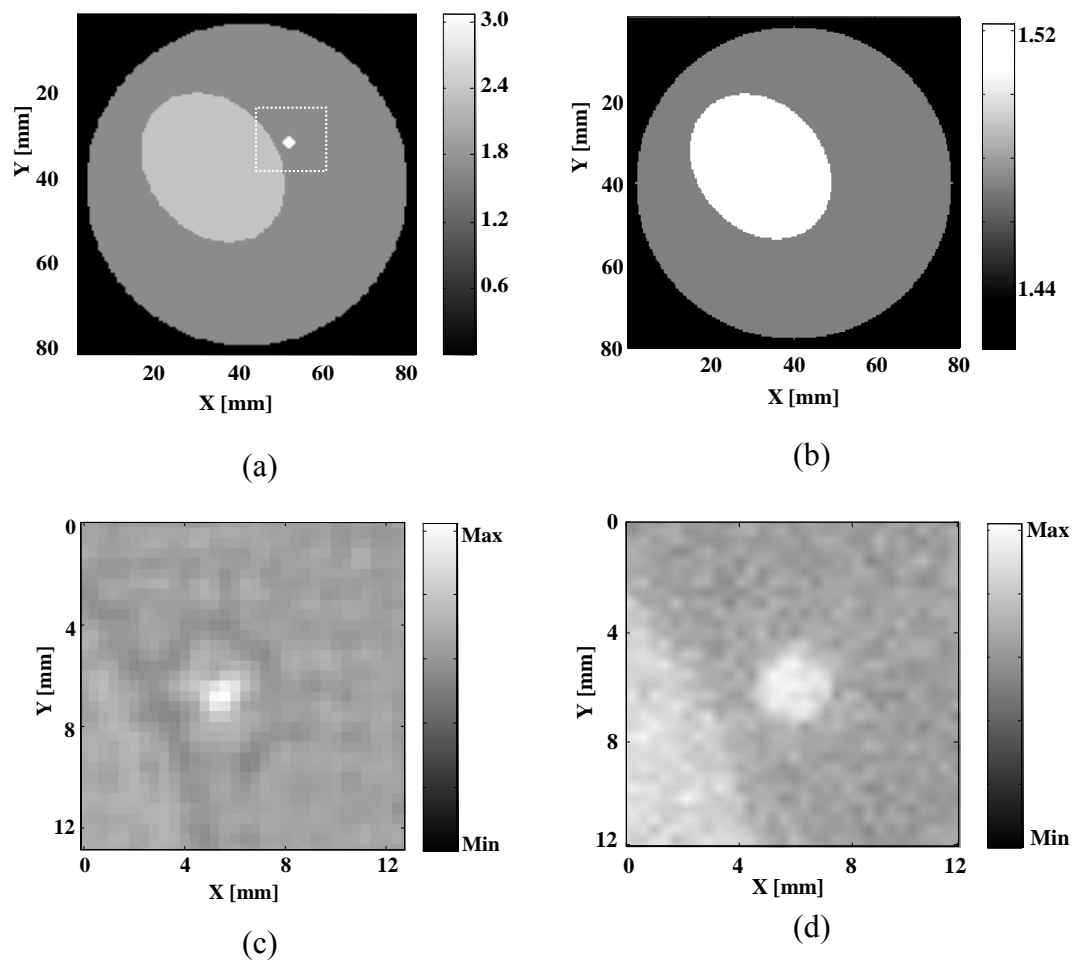


Fig. 4.3 Numerical simulation: (a) Object function (distribution of microwave absorption) for TAT in the simulated phantom sample and (b) object function (acoustic speed distribution) for UTT in the sample. To illustrate the blurring more clearly, we only showed the close-up TAT image of the small absorber as marked by the white dotted square in (a). (c) Close-up TAT image without correction for the acoustic speed variations and (d) close-up TAT image with correction for acoustic speed variations.

The effects of acoustic heterogeneities on TAT image were further illustrated by a phantom experiment. The sample was made by a piece of gelatin with two holes, one is

bigger, and another one is smaller. In Fig. 4.4(a), we assume homogeneous speed distribution, in which we use acoustic speed in mineral oil. We can see the distortion brought by the incorrect acoustic speed used in reconstruction. The acoustic speed in mineral oil is approximately 1.42 mm/us and the acoustic speed in gel is approximately 1.52 mm/us. By adjusting the average acoustic speed, we obtained much better image in Fig. 4.4(b) than in Fig. 4.4(a). In this case the TAT image was focused very well by adjusting average speed, but this method does not work well in small absorber detection in heterogeneous background. This will be shown by the next phantom experiment.

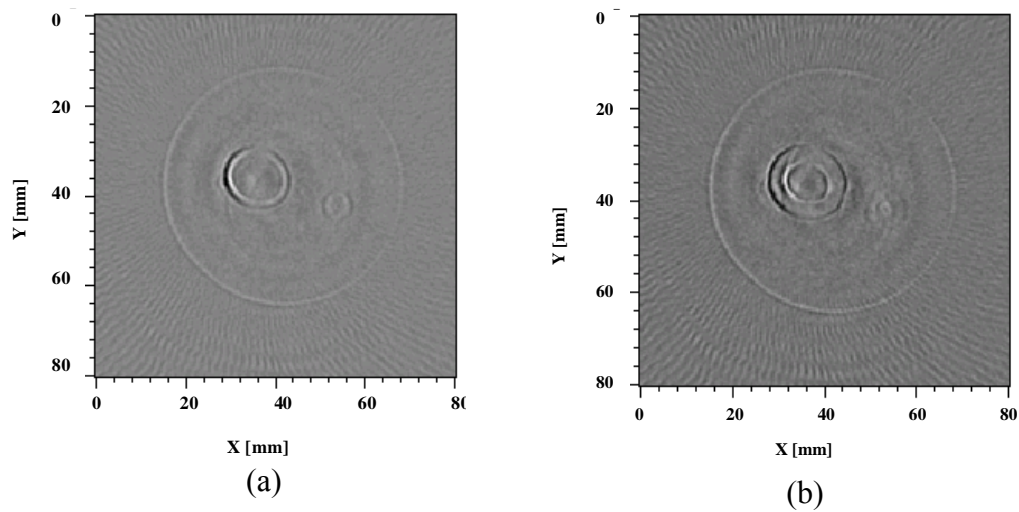


Fig. 4.4 Effects of speed variations on a sample made with gelatin: (a) TAT image without speed compensation; (b) TAT image with speed compensation by adjusting average speed.

Another phantom sample was made by porcine fat and muscle. A small absorber was embedded in the fat. In Fig. 4.5(a), the interface between muscle and fat was imaged well, but the small absorber close to the muscle was blurred due to the speed variations in the tissue. In Fig. 4.5(b), the strong absorber was imaged well, but the muscle shape was not imaged well due to inadequately adjust the acoustic speed in the tissue. The acoustic speed in fat is approximately 1.43 mm/us and the acoustic speed in muscle is approximately 1.51 mm/us. The difference in their acoustic speed is less than 10%. By adjusting the average speed, we obtain the sharpest boundaries for the bigger heterogeneities, but we also misrepresent the small absorber.

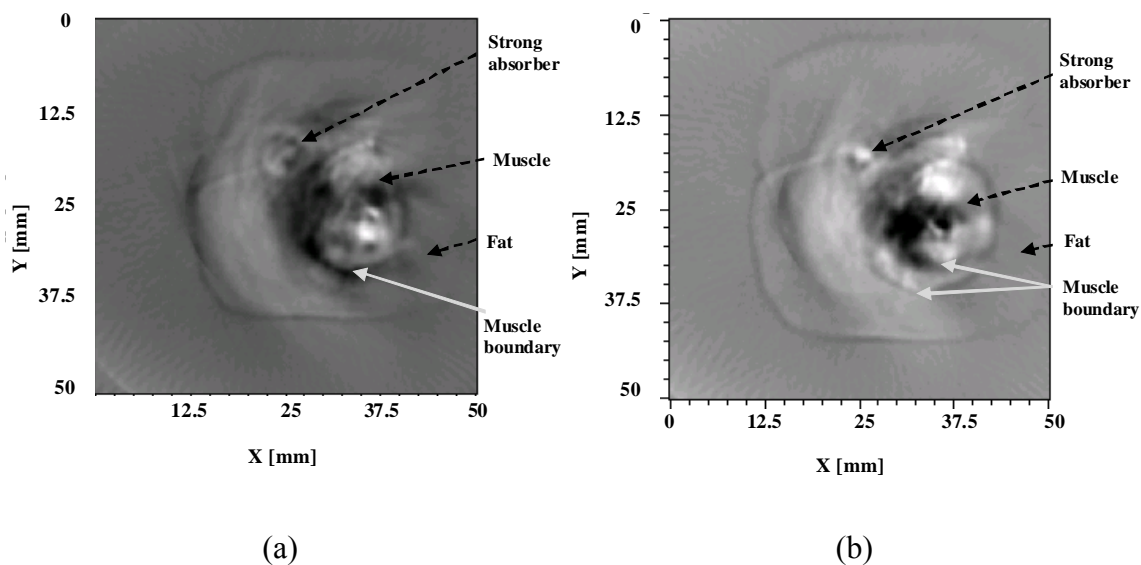


Fig. 4.5 Effects of speed variations on a sample made with porcine fat and muscle: (a) TAT image without speed compensation; (b) TAT image with speed compensation by adjusting average speed.

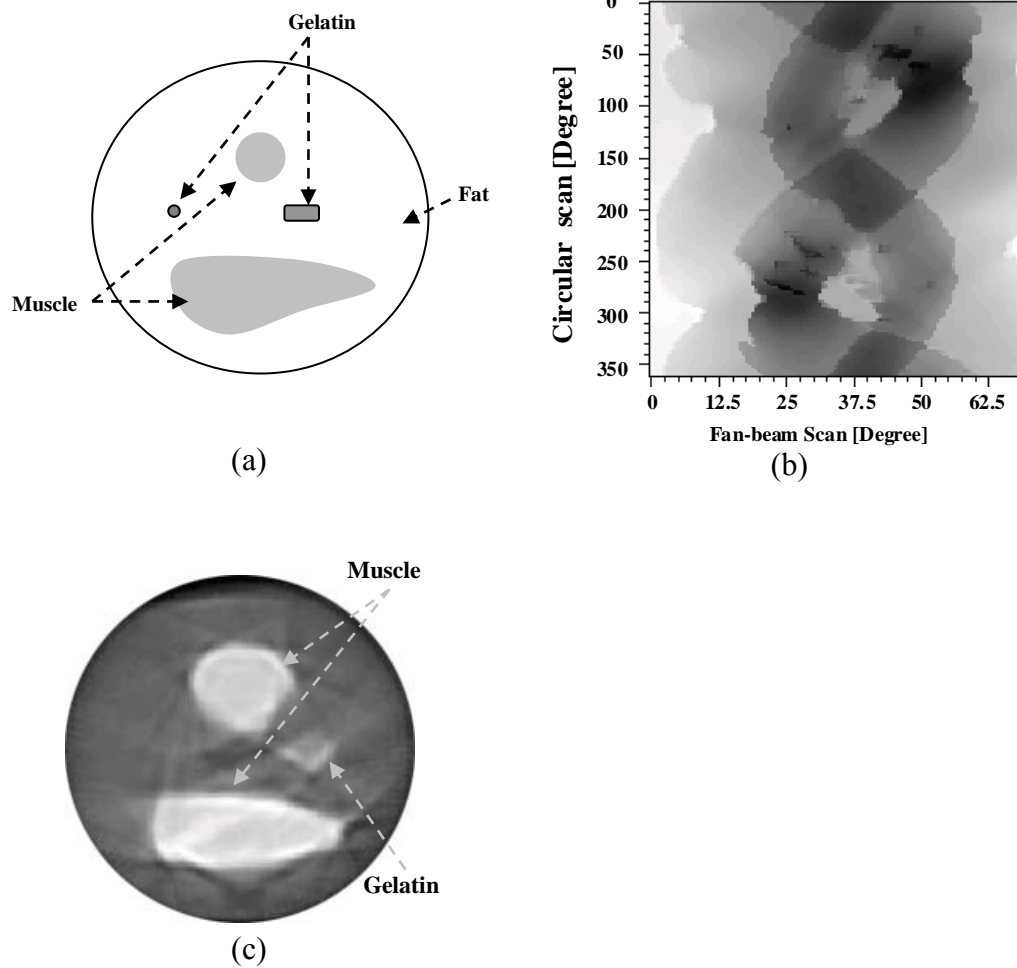


Fig. 4.6 (a) Schematic graph of the phantom used in the experiment; (b) Time of flight image reconstructed from the measurements by ultrasound transmission tomography; (c) Reconstructed speed-of-sound image by using filtered back-projection method. Small gelatin absorbers were not imaged very well in this image.

Next, we use a phantom experiment to illustrate how to get the speed-of-sound image from ultrasound transmission tomography. As shown in Fig. 4.6, the phantom was made by fat, muscle and gel and is illustrated in Fig. 4.6(a). We measured the time of flight perturbation by cross-correlating between the ultrasound waves transverse the medium with and without to-be-imaged object. The time-of-flight perturbation image was shown in Fig. 4.6(b). The time-of-flight perturbation measurements are then used to

reconstruct the sound-of-speed image of the tissue by using the filtered back-projection method, and the result is shown in Fig. 4.6(c). Apparently ultrasound transmission tomography failed to image two strong absorbers made by gelatin. Later we will show that TAT can image small absorbers much better than ultrasound transmission tomography.

We then investigated the performance of the proposed method with a phantom experiment. The phantom sample was composed of porcine fat and muscle. One large porcine muscle was embedded in the porcine fat. Figure 4.7(a) shows the top view of the phantom sample. The size of the phantom sample was approximately $61 \text{ mm} \times 39 \text{ mm}$, and the thickness of the sample was around 12 mm . The sizes of the muscle were approximately $17 \text{ mm} \times 21 \text{ mm}$. One small strong absorber was embedded near the larger piece of muscle. The diameter of small absorber was around 2.5 mm . The absorbers were also constructed from porcine muscle to take advantage of its strong absorption of microwave energy. The whole sample was immersed in mineral oil during the experiment. The phantom sample was designed to include within it relatively large acoustic speed variations. The speed-of-sound measurement is shown in Fig. 4.7(b). The measured acoustic speed in the porcine fat was about $1.44 \text{ mm}/\mu\text{s}$, and the measured acoustic speed in the porcine muscle was about $1.54 \text{ mm}/\mu\text{s}$. We compare the result by the acoustic speed compensation with the result by adjusting average acoustic speed in Fig. 4.7(c) and Fig. 4.7(d). To better illustrate the results, we only show close-up TAT images of the small absorber. First we reconstruct focused TAT image by adjusting average acoustic speed to obtain sharpest boundary for the porcine fat and muscle. We

get blurred image for the small absorber as marked by white arrows in Fig. 4.7(c). The TAT image obtained by acoustic speed compensation is shown in Fig. 4.7(d). The boundary of the small absorber obtained by the proposed method is sharper than that obtained by the method without considering the acoustic heterogeneities. The blurring of the small absorber is also not as serious in Fig. 4.7(d) as that in Fig. 4.7(c).

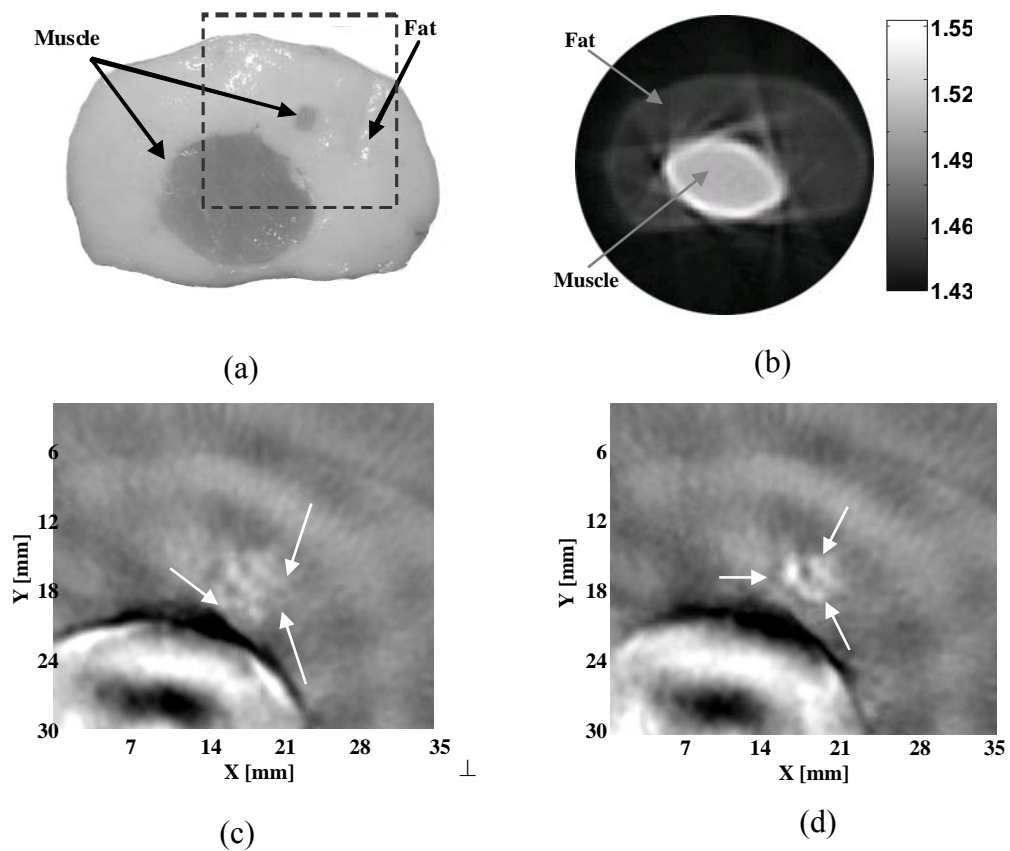


Fig. 4.7 Phantom experiment: (a) Photograph of the phantom sample in top view, (b) the speed-of-sound image of the phantom sample; To illustrate the blurring more clearly, we only showed the close-up TAT image of the small absorber as marked by the black dashed square in (a), (c) close-up TAT image obtained by adjusting the average acoustic speed (boundaries are denoted by arrows), (d) close-up TAT image obtained by acoustic speed compensation using the acoustic speed distribution (boundary are denoted by arrows).

The performance of the proposed method was further investigated by using a phantom experiment. The phantom sample was composed of porcine fat and muscle. We embedded in the sample two large porcine muscles that differed in acoustic speed from the porcine fat. The top view of the phantom sample is shown in Fig. 4.8(a). The size of the whole phantom sample was approximately $52 \text{ mm} \times 84 \text{ mm}$, and the thickness of the sample was around 20 mm . The sizes of the two pieces of muscle were approximately $14 \text{ mm} \times 25 \text{ mm}$ and $18 \text{ mm} \times 33 \text{ mm}$, respectively. Three small strong absorbers were embedded in the middle. The diameters of the three absorbers from top to bottom were around 2.5 mm . The absorbers were constructed from porcine muscle to take advantage of its strong absorption of microwave energy. The whole sample was immersed in mineral oil. The phantom sample was designed to include within it relatively large acoustic speed variations. The acoustic speed in the porcine fat was approximately $1.4 \text{ mm}/\mu\text{s}$, and the acoustic speed in the porcine muscle was approximately $1.52 \text{ mm}/\mu\text{s}$. The acoustic speed difference between the porcine fat and porcine muscle was around 10%. Fig. 4.8(b) shows the reconstructed speed-of-sound image, which fails to show the three small absorbers. Therefore, UTT can image large acoustic speed heterogeneity with good accuracy, but its ability to image smaller acoustic speed heterogeneity is limited. Figures 4.8(c) and (d) show the TAT images of the small absorbers obtained by adjusting the average acoustic speed and by acoustic-speed compensation, respectively. The three small absorbers are marked by white arrows. As can be seen, the center of the scanning geometry has the highest resolution, whereas the outer regions have lower resolutions. Both the size and the intensity of the small absorbers are improved by the

proposed acoustic-speed compensation method. The improvement of the image quality is further illustrated in Fig. 4.8(e) and (f) in line plots across two of the small absorbers in the reconstructed TAT images (shown by gray arrows) in Fig. 4.8(c) and (d). The actual sizes of the absorbers are shown by the dotted circles. The size of each absorber read from the line plot based on Fig. 4.8(e) is approximately 3.0 mm in FWHM, whereas the size of each absorber read from the line plot based on Fig. 4.8 (f) is around 3.5 mm in FWHM. Although the measured sizes are larger than the actual size of each absorber, the acoustic-speed compensation method greatly increases in the ability of TAT to quantitatively define the size of the small absorbers.

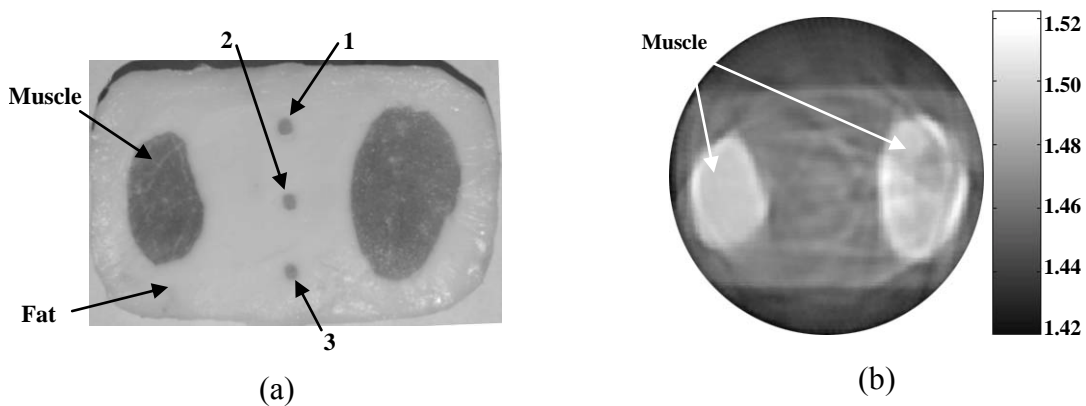


Fig. 4.8 Phantom experiment: (a) Photograph of the phantom sample in top view, the three absorbers were made by porcine muscle, (b) the speed-of-sound image of the phantom sample, (c) TAT image obtained by adjusting the average acoustic speed (boundaries are denoted by arrows), (d) TAT image obtained by acoustic speed compensation using the acoustic speed distribution (boundary are denoted by arrows), (e) line plot across absorber 1 as pointed by the gray dashed arrows in (c), and (f) line plot across absorber 3 as pointed by the gray dashed arrows in (c). The actual sizes of the absorbers were shown by dotted circles in (e) and (f).

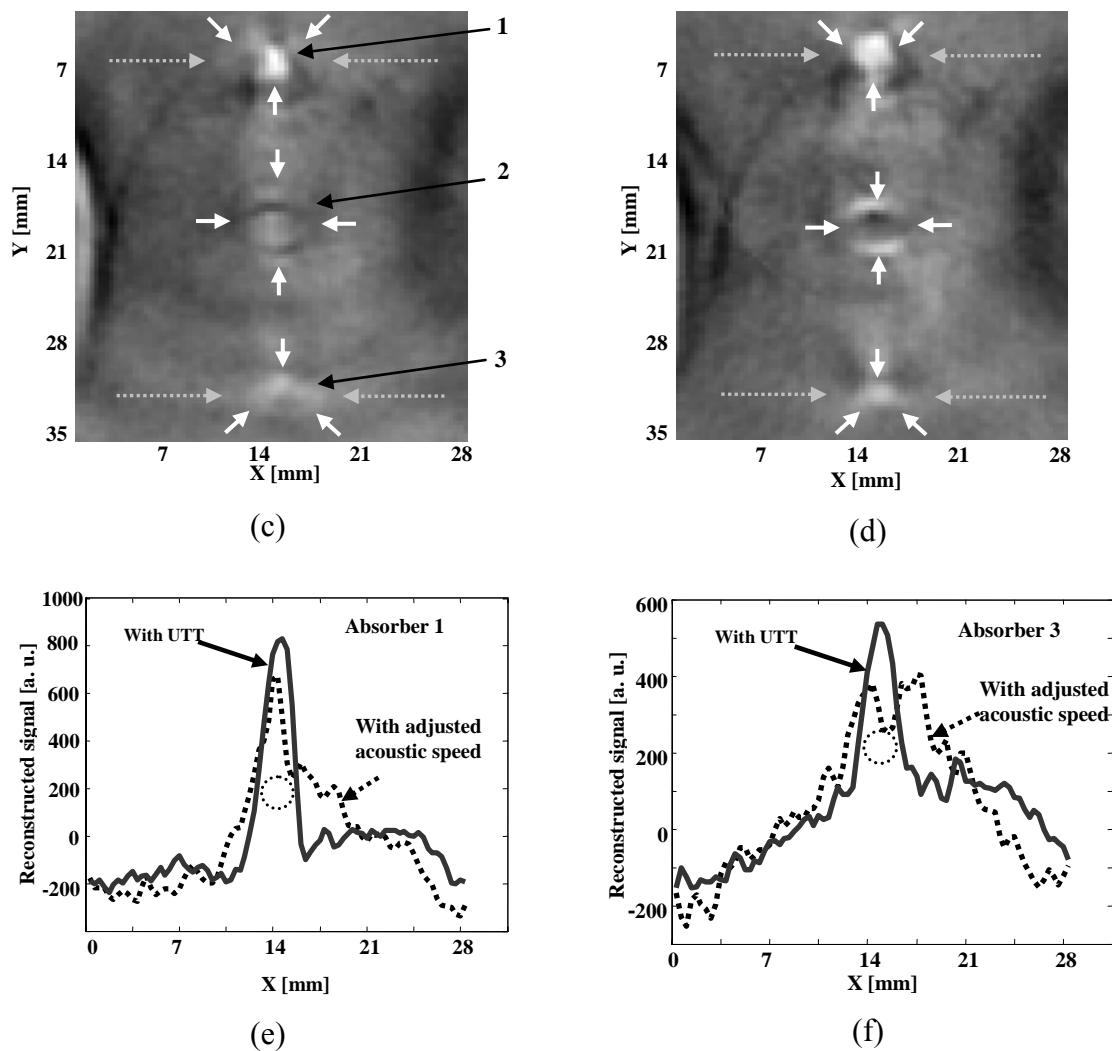


Fig. 4.8 Continued.

The main limitation of the current experimental system is the time required to acquire the data. The data acquisition time can be greatly reduced by using a linear ultrasonic array as the receiver. If the refraction effects are small, it has been shown that the ray-tracing method can be used to improve the results of UTT.⁷¹⁻⁷³ Also inherent in

the application of the UTT algorithm is the assumption that ultrasound pulses travel in straight lines through the target. In some applications, the refraction can be an important cause of artifacts, spatial distortion and loss of resolution. Because of refraction effects, this assumption may be increasingly invalid when acoustic speed variations are greater. For highly refractive tissue, acoustic speed compensation requires more accurate acoustic speed imaging to calculate the refracted beam paths. In such cases, we need to take special measures to improve measurements of the speed-of-sound distributions in the tissue. Mechanical inaccuracies resulting from the use of the stepped single-element transducer is another source of inaccuracies in the reconstructed acoustic speed distribution of UTT, but this error can also be alleviated by using a linear array. Compensation of TAT using UTT is also limited by other quantitative or geometrical properties of the acoustic speed images produced. For example, since the resolution of time-of-flight projections is determined by the transmitted ultrasound beam width, this represents the minimum resolution of the acoustic speed image. These limitations, however, have minimal effect on the correction of the distortion and blurring induced by relatively large acoustic speed variations in TAT.

A potential application for TAT imaging is to use this technique to build a portable instrument to image pediatric brains with intact skull.²³ One of the main obstacles to this potential application is the distortion of the reconstructed TAT images brought about by the highly refractive skull.⁷⁴ When the skull is involved in TAT imaging, another imaging modality can be used to obtain the skull profile.^{75,76} By taking

more biological tissue properties into consideration, we may be able to develop better algorithms to correct the effects of acoustic heterogeneities in TAT brain imaging.

4.6 Conclusions

We have proposed a method for using UTT to compensate for the degradation in TAT images caused by acoustic speed variations in the biological tissue. It has been shown that UTT can, within certain limitations, generate accurate and quantitative images of the acoustic speed distributions of phantoms, which results in high registration accuracy in the TAT images. It has also been shown by a phantom experiment that those acoustic speed images have sufficient accuracy to compensate for the effects of acoustic speed heterogeneities in TAT images. The results obtained by this system indicate that TAT with the acoustic speed compensation is a feasible approach for obtaining higher resolution images of small tumors in acoustically heterogeneous tissues.

5. THE EFFECTS OF ACOUSTIC HETEROGENEITIES ON TRANSCRANIAL BRAIN IMAGING

5.1 Introduction

Because of the large penetration depth of microwave in biological tissue, one of the potential applications of TAT is transcranial brain imaging. Current transcranial brain imaging modalities include ultrasound imaging, X-ray computerized tomography (CT) and magnetic resonance imaging (MRI). Ultrasound imaging has been established as a routine technique to image intracranial abnormalities in newborns when the fontanelles are open. The quality of intracranial brain images, however, becomes worse after closure of the fontanelles. Ultrasound imaging is also limited by its ability to differentiate different tissues in the brain, and only a few structures can be identified.^{77,78} In addition, ultrasound imaging in reflection mode experiences two-way transmission, whereas TAT has only one-way transmission. Because one-way transmission loss through skull is only half of the two-way transmission loss,⁷⁴ TAT suffers from less attenuation and image distortion than ultrasound imaging. Moreover, because of its small size, a TAT system can be easily made portable at 3 GHz. Both CT and MRI have been shown to be capable of obtaining good brain images. X-ray CT, however, is an ionizing radiation; it is unsafe to be used on patients in need of long time monitoring of brain diseases. The cost and availability of MRI also limits its application. Thus it is necessary to develop an inexpensive, portable, non-ionizing, and high-resolution imaging modality, such as TAT, that can be used at the bedside and the operating room to monitor brain diseases.

Experimental evidences in a previous study by Xu and Wang²³ have shown that some thermoacoustic energy can propagate through the skull and generate useful information of the brain structures. Nevertheless, those experimental studies are limited to infants at the age following the closure of the fontanelles, and, thus, monkey heads with a skull thickness of approximately 1 mm are used as tissue samples to simulate the human head. The distortion brought by the skull bone has been ignored by assuming the thin skull layer has only ignorable influences on the reconstructed image. No information, however, has been provided on how the skull bone affects the image quality of TAT and to what extent we can trust the results obtained without considering the attenuation, reflection and refraction of the skull bone. In addition, studies on the properties of human brain have shown that as a child grows, the differences in dielectric properties of the brain become greater;⁷⁹ we expect better image contrasts in young adults. The skull bone, however, thickens considerably from the birth of a child to the adulthood, and consequently induces stronger attenuation and distortion as a child grows.⁸⁰ The skull-induced distortion remains an obstacle for further improving image quality for transcranial brain imaging with TAT. As we know, acoustic speed variations alone can cause displacements of the thermoacoustic signals both axially and tangentially. In the previous section, we corrected the effect of first-order acoustic speed variation on TAT with acoustic speed distribution measured by ultrasound transmission tomography.⁸¹ In this way we only compensated for the displacements of thermoacoustic signals along the assumed linear radiating propagation paths. For highly refractive tissue with respect to soft tissue, such as skull bone, we need to consider the second-order

acoustic speed variations that are due to ultrasonic refraction from the assumed straight paths. If we ignore ultrasonic refraction in the reconstruction algorithm, the recorded acoustic signals from a given viewing angle would be backprojected to a wrong location in the imaging region. This causes both blurring and dislocation and reduces image contrast. Our experimental data also show that the majority of the frequency components in thermoacoustic signals are below 1 MHz, in this frequency range the distortion and attenuation by the human skull is shown to be minimal when the incident directions are nearly normal to the skull surface.⁷⁴ When the incident directions are oblique, however, refraction effects become substantial and shear waves also arise from mode conversions. It is, therefore, necessary to take into consideration of the distortions caused by the skull to obtain good transcranial brain images with TAT.

In this study, we first examined the effects of skull on transcranial TAT images. Then we proposed a numerical model that considers wave reflection and refraction in calculating the propagation of thermoacoustic waves. This model was used to evaluate the feasibility of transcranial TAT through a skull with both simulated and experimental data. The results obtained with our model were compared with the results without considering the skull-induced distortion to evaluate the skull-induced effects on the image reconstruction. We demonstrated that the image quality could be improved by incorporating the skull shape and acoustic properties into image reconstruction.

5.2 Theory and method

5.2.1 Forward propagation in a heterogeneous medium

Reconstruction algorithms for TAT have been extensively studied for a homogeneous medium, in which a constant acoustic speed is assumed. In clinical applications, the acoustic speed is often spatially variant. In this case, a mathematical model to describe the wave propagation can be written as:^{51,82}

$$\left(1 + \alpha(\mathbf{r}) \frac{\partial}{\partial t}\right) \left[\rho(\mathbf{r}) \nabla \cdot \left(\frac{1}{\rho(\mathbf{r})} \nabla p(\mathbf{r}, t) \right) \right] - \frac{1}{c^2(\mathbf{r})} \frac{\partial^2 p(\mathbf{r}, t)}{\partial t^2} = - \frac{\beta}{C_p} \frac{\partial H(\mathbf{r}, t)}{\partial t} \quad (5.1)$$

where $\alpha(\mathbf{r})$ is the ultrasonic absorption distribution, $\rho(\mathbf{r})$ is the density distribution, β is the volume thermal expansion coefficient, C_p is the specific heat, $p(\mathbf{r}, t)$ is the measured pressure at position \mathbf{r} and time t , $c(\mathbf{r})$ is the acoustic speed distribution, and $H(\mathbf{r}, t)$ is the microwave heating function. In the thermal confinement regime, the heating function can be written as a product of a spatial energy deposition function $\varphi(\mathbf{r})$ and a microwave pulse function $I(t)$: i.e., $H(\mathbf{r}, t) = \varphi(\mathbf{r}) \cdot I(t)$. A microwave pulse of sufficiently short duration in comparison to the acoustic transit time through the characteristic length can be approximated by a delta function $\delta(t)$. In the following analysis, we assume that $I(t)$ equals $\delta(t)$. The source $\varphi(\mathbf{r})$ excites the initial wave-field $p_0(\mathbf{r})$, which then propagates through the medium with acoustic speed $c(\mathbf{r})$.

In Eq. (5.1), the speed of sound, density and ultrasonic absorption are functions of space. This forward problem is nonlinear.⁶⁹ In a highly refractive medium, such as the

skull bone in soft tissue, where the variation of the speed of sound is more than 50%, existing reconstruction algorithms^{48-51,81} are incapable of obtaining good image quality without considering wave refraction and other skull-induced distortion. Owing to high acoustic speed, irregular shape and non-uniform thickness of the skull, it is also practically impossible to obtain an exact reconstruction formula from Eq. (5.1). Therefore, we develop a numerical model to simulate the forward problem and to solve the inverse problem. We will discuss the numerical model in section 5.2.3.

5.2.2 Effects of skull bone on TAT image

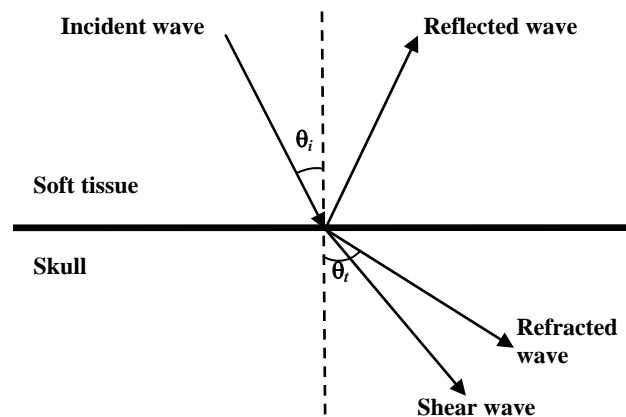


Fig. 5.1 Schematic illustration of the reflection, refraction, and mode conversion of the longitudinal incident waves.

Thermoacoustic waves propagate in brain tissue mainly as longitudinal waves, but on the inner-skull surface they will experience mode conversion, reflection and refraction, as shown in Fig. 5.1, and, thus, we expect both phase and amplitude distortion.

Shear waves can be produced when ultrasound waves travel from soft tissue to bone. They are generally neglected in imaging of soft tissues because they need solid material to be effectively propagated. Shear waves are generated in skull using some of the energy from the incident longitudinal waves through mode conversion. When the ultrasound waves normally incident on the skull (incident angle $\theta_i = 0^\circ$), no shear waves are produced, so only longitudinal waves are considered in imaging. In transcranial brain imaging with TAT, oblique angles of incidence are inevitable because of the irregular shape of the skull. As the incident angle increases, conversion to shear waves gradually increases. When the incident angle becomes greater than the critical angle, only shear waves can propagate into the skull. The measurements in previous study^{74,83} show that the conversion to shear waves in the skull layer is negligible when incident angles are less than 20° . As incident angles become larger than 20° , shear waves gradually dominate the transmitted ultrasound waves. Shear wave imaging has some drawbacks. It has been shown that although the shear wave has lower acoustic speed than the longitudinal wave thus better impedance match with the surrounding medium, the attenuation coefficient for the shear wave is much higher than that for the longitudinal wave in the skull.⁸³ Due to the lower acoustic speed in the skull the wavelength of the shear wave is shorter than that of the longitudinal wave at the same frequency, the resolution of the shear wave, however, may turn out to be worse than that of the longitudinal wave because the attenuation coefficient increases as the frequency increases and after the ultrasonic pulses pass through the skull the central frequency of shear wave is lower than that of the longitudinal wave. For the same reason, the signal-

to-noise ratio of longitudinal wave images is better than that of the shear-wave counterparts. In this study we neglect shear waves and, thus, only model longitudinal waves.

Phase distortion is primarily induced by the high acoustic speed in the skull. As the control factor for reconstructing an undistorted TAT image, the phases of the received signals need to be corrected so that when propagated back to the source the signals can be added in phase. In normal incidence, the skull thickness of an infant is about 1 mm, and the phase shift caused by the skull is linear over a large range of frequencies. As a child grows, the skull becomes thicker, and the phase shift at higher frequency begins to depart from linearity.⁷⁴ Nevertheless, in the frequency range from 0.3 MHz and 1.0 MHz, where the main components of the TAT signals reside, the phase shift caused by the skull remains linear with the frequency, indicating non-dispersive transmission across this frequency range.⁷⁴ Therefore, the phase correction for normal incidence can be easily implemented by adding a constant time shift term when we reconstruct the image in the time domain. If the time shift is much less than 0.5 μ s (the pulse-width of the microwave source used in our current TAT system), we can neglect the shift. Oftentimes the thermoacoustic waves are obliquely incident on the inner-skull and we have to perform the phase compensation on each single source to obtain a focused image at the target region inside the brain.

The thermoacoustic wave is attenuated in amplitude by absorption, scattering and reflection as it travels through the skull. The absorption and scattering are mainly brought by the dipole layer in the skull. The dipole layer is cancellous bone with a blood

and fat-filled porous structure, and the insertion loss increases with frequency. For infants, their skull bones are thin, have little or no dipole layers and the attenuations are low over a large frequency range.⁷⁴ The absence of the dipole layer also eliminates the dependence of insertion loss with the frequency. We can, therefore, neglect the amplitude attenuation caused by absorption and scattering in the infant skull. For young adults, ultrasonic waves passing through the skull reach the receiver with nearly linear attenuations in the frequency range of less than 1.0 MHz. The attenuation induced by absorption and scattering, however, is smaller than reflection loss,⁷⁴ and, thus, in this study we simplify Eq. (5.1) by neglecting the effects of the absorption loss on ultrasonic waves,

$$\left[\rho(\mathbf{r}) \nabla \cdot \left(\frac{1}{\rho(\mathbf{r})} \nabla p(\mathbf{r}, t) \right) \right] - \frac{1}{c^2(\mathbf{r})} \frac{\partial^2 p(\mathbf{r}, t)}{\partial t^2} = -\frac{\beta}{C_p} \frac{\partial H(\mathbf{r}, t)}{\partial t} \quad (5.2)$$

Wave reflection and refraction are also important sources for the amplitude distortion. To simplify our analysis, the skull has been treated as a homogenous material, and the thickness of the skull bone is assumed to vary slowly on the scale of the wavelengths used for imaging. Under these assumptions, the skull is modeled as having a local constant thickness and the pressure transmission coefficient at each interface is expressed as:⁶⁹

$$T = \frac{2 \cdot \rho_2 c_2 \cos \theta_i}{\rho_2 c_2 \cos \theta_i + \rho_1 c_1 \cos \theta_t} \quad (5.3)$$

where ρ_1 and c_1 are the density and acoustic speed of the incident medium, respectively; ρ_2 and c_2 are the density and acoustic speed of the transmission medium,

respectively. The incident angle is θ_i and the refracted angle is θ_t . The refracted angle can be eliminated by using Snell's law. The expression for the transmittance is more complicated when mode conversion is considered, because both longitudinal and shear impedance will be involved in the expression. Therefore, Eq. (5.3) is only an approximation of the forward transmission through the skull. Because we are only interested in longitudinal waves in reconstruction, we will use this approximated form in our numerical model. Multi-path interferences induced by wave reflection refraction at the interfaces can also induce amplitude distortion, and their effects can be corrected by considering wave reflection and refraction in reconstruction.

5.2.3 Numerical model for acoustically heterogeneous problem

In this section, we describe the method to calculate the forward propagation of thermoacoustic waves through the skull and then propose an image reconstruction method. The simulation is based on a three-layer linear transmission model, which takes into account acoustic wave refraction and reflection at the tissue interfaces. The whole imaging area is divided into three acoustically homogeneous layers: the brain, the skull and the skin along with coupling medium. Here, we assume the brain, skin and coupling medium are acoustically identical. Under the assumption that the skull is homogeneous with constant acoustic speed and density, the skull thickness and shape are the main parameters to control the amplitude attenuation and phase distortion.

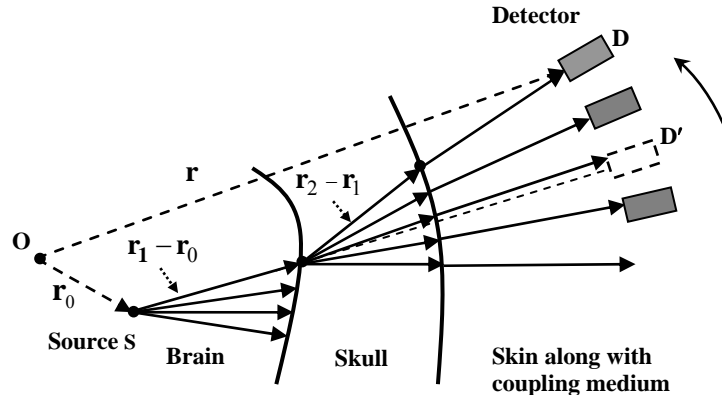


Fig. 5.2 Schematic illustration of the forward TAT propagation.

Consider a simple source S at an arbitrary location \mathbf{r}_0 within the brain as shown in Fig. 5.2. Here we assume the distance between source S and skull surface is much larger than the wavelength. The coordinate origin O is chosen at a selected center inside the skull. We will refer it as the image center in this section. If the source S emits ultrasonic waves isotropically in all directions, the spectrum of the pressure at an arbitrary point \mathbf{r}' within the brain tissue can be written as^{51,84,85}

$$\tilde{p}(\mathbf{r}', k_1) = -\frac{ik_1}{4\pi} \frac{\exp(ik_1|\mathbf{r}' - \mathbf{r}_0|)}{|\mathbf{r}' - \mathbf{r}_0|} p_0(\mathbf{r}_0) \quad (5.4)$$

here, where $p_0(\mathbf{r}_0) = \varphi(\mathbf{r}_0)\Gamma(\mathbf{r}_0)$, $\Gamma(\mathbf{r}_0) = \beta c_1^2 / C_p$, $k_1 = \omega / c_1 = 2\pi / \lambda$ is the wave number in the brain, ω is the angular frequency, λ is the wavelength, and $\bar{t}_0 = c_1 t_0$. In this section, we use the Fourier transformation pair: $\tilde{f}(k) = \int_{-\infty}^{\infty} f(\bar{t}) e^{ik\bar{t}} d\bar{t}$ and $f(\bar{t}) = \frac{1}{2\pi} \int_{-\infty}^{\infty} \tilde{f}(k) e^{-ik\bar{t}} dk$, where $\bar{t} = ct$. Because the wavelength in the skull can be comparable or even larger than the thickness of the skull, on the inner-skull surface diffraction dominates the wave propagation. The condition under which ray theory works is violated,⁶⁹ and, therefore,

we will treat the inner-skull surface area as the secondary source. Let's consider a small surface area ds_2 on the inner-skull surface. On one side of the surface there is brain tissue with density ρ_1 and sound speed c_1 , and on the other side there is skull tissue with density ρ_2 and sound speed c_2 . Here, ds_2 can be regarded as a baffled simple source. The spectrum of the pressure at \mathbf{r}' within the brain tissue is related to the velocity potential $\Phi(\mathbf{r}', k_1)$ by⁶⁹

$$\tilde{p}(\mathbf{r}', k_1) = ik_1 \rho_1 c_1 \Phi(\mathbf{r}', k_1) \quad (5.5)$$

And the radial particle velocity with respect to source S in the brain before reaching the skull is

$$\mathbf{u}_1 = -\nabla \Phi(\mathbf{r}', k_1) = \nabla \left(\frac{i}{k_1 \rho_1 c_1} \tilde{p}(\mathbf{r}', k_1) \right) \quad (5.6)$$

Particle velocity transmission coefficient T_{12} is written as $(\rho_1 c_1 / \rho_2 c_2) \cdot T$ (T is defined in Eq. (5.3)). The particle velocity in the skull is equal to the product of \mathbf{u}_1 and T_{12} , and, thus, the particle velocity \mathbf{u}_2 that is normal to the interface in the skull becomes $\mathbf{u}_1 T_{12} \cos(\theta_{1t})$, where refracted angle θ_{1t} in the skull layer is related to the incident angle on the inner-skull surface θ_{1i} by Snell's law. By combining Eqs. (5.5) and (5.6), the spectrum of the pressure $p(\mathbf{r}_1)$ on the inner-skull surface due to the simple source S can be approximated by^{84,85}

$$\tilde{p}(\mathbf{r}_1, k_1) = (\rho_2 c_2) \mathbf{u}_2 = \frac{ik_1 \rho_2 c_2}{4\pi \rho_1 c_1} p_0(\mathbf{r}_0) \frac{\exp(ik_1 |\mathbf{r}_1 - \mathbf{r}_0|)}{|\mathbf{r}_1 - \mathbf{r}_0|} \left(1 - \frac{1}{ik_1 |\mathbf{r}_1 - \mathbf{r}_0|} \right) T_{12} \cos(\theta_{1t}) \quad (5.7)$$

If we divide the imaging region into M small point sources, then the spectrum of the total pressure at \mathbf{r}_1 on the inner-skull surface can be written as

$$\tilde{p}'(\mathbf{r}_1, k_1) = \sum_{m=1}^M \tilde{p}(\mathbf{r}_{0m}, k_1) \quad (5.8)$$

The subscript m of each parameter in Eq. (5.8) means that value is induced by the simple source m in the imaging area. Similarly, the spectrum of the pressure induced by the inner-skull surface area ds_2 at an arbitrary point \mathbf{r}'' inside the skull can be written as

$$\begin{aligned} \tilde{p}''(\mathbf{r}'', k_2) &= \frac{-ik_2}{2\pi} \frac{\exp(ik_2|\mathbf{r}'' - \mathbf{r}_1|)}{|\mathbf{r}'' - \mathbf{r}_1|} \tilde{p}(\mathbf{r}_1, k_1) \\ &= \frac{k_1 k_2 \rho_2 c_2}{8\pi^2 \rho_1 c_1} \sum_{m=1}^M p_0(\mathbf{r}_{0m}) \frac{\exp(ik_2|\mathbf{r}'' - \mathbf{r}_1| + ik_1|\mathbf{r}_1 - \mathbf{r}_{0m}|)}{|\mathbf{r}'' - \mathbf{r}_1| |\mathbf{r}_1 - \mathbf{r}_{0m}|} \left(1 - \frac{1}{ik_1|\mathbf{r}_1 - \mathbf{r}_{0m}|}\right) T_{12m} \cos(\theta_{1m}) \end{aligned} \quad (5.9)$$

After leaving the skull, the ultrasonic waves transmit into the skin and coupling medium and are received by the ultrasonic transducer in the far field. Because diffraction effects no longer dominate the wave propagation at this interface, under the assumption that energy is transmitted along well-defined path, we can use rays rather than waves to investigate their effects, and, thus, we use Snell's law and Eq. (5.3) to compute approximately the strength of the pressures obtained by the receiver. Let the inner-skull have N secondary sources and the outer-skull be discretized by L parts, the spectrum of the pressure on the transducer at location \mathbf{r}_d can be computed as

$$\begin{aligned} \tilde{p}(\mathbf{r}_d, \omega) &= \frac{k_1 k_2 \rho_2 c_2}{8\pi^2 \rho_1 c_1} \sum_{l=1}^L \sum_{m=1}^M \sum_{n=1}^N \left(1 - \frac{1}{ik_1|\mathbf{r}_{1n} - \mathbf{r}_{0m}|}\right) \times \\ &\quad \frac{\exp(i(k_3|\mathbf{r}_d - \mathbf{r}_{2l}| + k_2|\mathbf{r}_{2l} - \mathbf{r}_{1n}| + k_1|\mathbf{r}_{1n} - \mathbf{r}_{0m}|))}{|\mathbf{r}_{2l} - \mathbf{r}_{1n}| \cdot |\mathbf{r}_{1n} - \mathbf{r}_{0m}| |\mathbf{r}_d - \mathbf{r}_{2l}|} T_{12mn} T_{23nl} \cos(\theta_{1m}) p_0(\mathbf{r}_{0m}) \end{aligned} \quad (5.10)$$

where subscripts n, l represent the location at the inner-skull and outer-skull surfaces, respectively, and T_{23nl} means the transmission coefficient at the outer-skull interface.

Next, we transform Eq. (5.10) back into the time domain. Because $k_1|\mathbf{r}_{1n} - \mathbf{r}_{0m}| \gg 1$ under the assumption that the distance between any source point and the inner skull surface is much larger than the wavelength, we can get the following approximation in the time domain

$$p(\mathbf{r}_d, t) \approx -\frac{\rho_2}{2\rho_1 c_1^2} \sum_{l=1}^L \sum_{m=1}^M \sum_{n=1}^N \frac{T_{12mn} T_{23nl} p_0(\mathbf{r}_{0m}) \cos(\theta_{1lm})}{\bar{t}_1 \bar{t}_2 \bar{t}_3} \frac{\partial^2 \delta(t - t_1 - t_2 - t_3)}{\partial t_1 \partial t_2} \Bigg|_{\substack{\bar{t}_1 = |\mathbf{r}_{1n} - \mathbf{r}_{0m}| \\ \bar{t}_2 = |\mathbf{r}_{2l} - \mathbf{r}_{1n}| \\ \bar{t}_3 = |\mathbf{r}_d - \mathbf{r}_{2l}|}} \quad (5.11)$$

Here, $\bar{t}_1 = c_1 t_1$, $\bar{t}_2 = c_2 t_2$ and $\bar{t}_3 = c_3 t_3$. The temporal delta function comes from the fact that the PA source is assumed to be induced by a delta pulse.

In our simulation, we partition the imaging region into small cells (much less than the wavelengths used for imaging), and then calculate ultrasonic reflection and refraction based on the digitized model. Assume the skull surfaces are continuous and differentiable. To compute the refracted angle, we first calculate the normal direction at the intersecting point, and then apply Snell's law. Locally weighted smooth method with least squares quadratic polynomial fitting is used when necessary. Depending on the location of the simple source within the brain, the incident angles may be normal or oblique. In calculating the wave refraction on a cell, we take into consideration of the total reflection by calculating the incident angle for each ray from any precedent simple source to the current cell and comparing the incident angle with the critical angle to find the non-transmitting cases. The refracted ray after leaving the outer-skull surface will

travel several centimeters before it reaches the ultrasonic receiver, and then, it will be additively received by the ultrasonic transducer. The computation complex is determined by the number of the simple sources in the imaging area and the secondary simple sources on the inner-skull surface. Because our current experimental system is in 2-D, we will use the 2-D version of the numerical model in this study, but it is obvious that the same principle applies to 3-D cases as well. In our simulations and experiments, nonlinear effects (such as induction of harmonic frequency) and brain tissue absorption will be ignored because their effects are minimal in the frequency range used in the experiments.

For the inverse problem, the thermoacoustic signal received by each ultrasonic receiver is backprojected along the refracted path to the imaging region. Each receiver acts as a source to emit ultrasonic waves covering the imaging region. The propagation path and amplitude is computed in the same way as in the forward problem, except that we treat the surface area at the outer-skull surface as the secondary source, use Snell's law on the inner-skull surface and perform the reconstruction for each time step at the time interval we are interested in. In order to compensate for the energy loss during transmission, the transmission coefficients are replaced by their inverse value at each interface during reconstruction. It will be shown in the following section that when the source is close to image center the results obtained with this numerical reconstruction method agree well with those obtained from the filtered back-projection algorithm, and as imaging sources becomes closer to the surface of the inner-skull, the filtered back-projection method starts to generate distorted images, and our method, although still

incapable of completely compensating for the effects of shear waves due to unavailability of information of shear waves, can effectively correct most of the distortions and generate better images.

5.3 Results

5.3.1 Simulations of transcranial brain imaging with TAT

To study the effects of the acoustic heterogeneities on TAT image, we used the above mentioned three-layer model. The acoustic speeds in the brain tissue and coupling medium were selected to be 1.51 mm/ μ s and 1.43 mm/ μ s respectively. The acoustic speed in the skull was chosen to be 2.37 mm/ μ s, which was within the range of the acoustic speed in the skull obtained by Fry⁷⁴ in the frequency range below 1 MHz. According to known measurements,^{32,86} the density of the brain tissue, skull and coupling medium were chosen to be 1035, 1700, and 850 kg/m³, respectively.

We simulated TAT results of a phantom sample with five small strong absorbers. The absorbers were placed on a straight line with an equal space of 4 mm and a diameter of 1.5 mm. The skull surfaces were in elliptic shapes. The outer-skull surface had a semiminor axis 22 mm and a semimajor axis 26 mm, and the inner-skull surface had a semiminor axis 20 mm and a semimajor axis 23.5 mm as shown in Fig. 5.3(a). The close-up image of the absorbers is shown in Fig. 5.3(b). The reconstructed images are

shown in Fig. 5.3 (c) and (d), in which Fig. 5.3(c) was obtained by using a filtered back-projection method,⁴⁸ and Fig. 5.3(d) was obtained by using the proposed numerical method. In Fig. 5.3(e), we compare the line plots across the five absorbers in the reconstructed image by using the two different reconstruction methods. We find that when the absorber is close to the image center, we can obtain a good image by simply using the filtered back-projection method. As the absorber becomes closer to the inner-skull surface, by using the filtered back projection method, however, we got blurred images due to neglecting the refraction and mode conversion of the skull. By using the proposed numerical method, we obtain better images for the absorbers closer to the skull surfaces, but we can only partially reconstructed the strength of the absorber because of the assumption that shear waves contribute trivially to the reconstruction,. This becomes increasingly true when the absorber becomes closer and closer to the inner-skull surface. Nevertheless, compared with the filtered back projection method, our numerical method still shows much improvement of image quality.

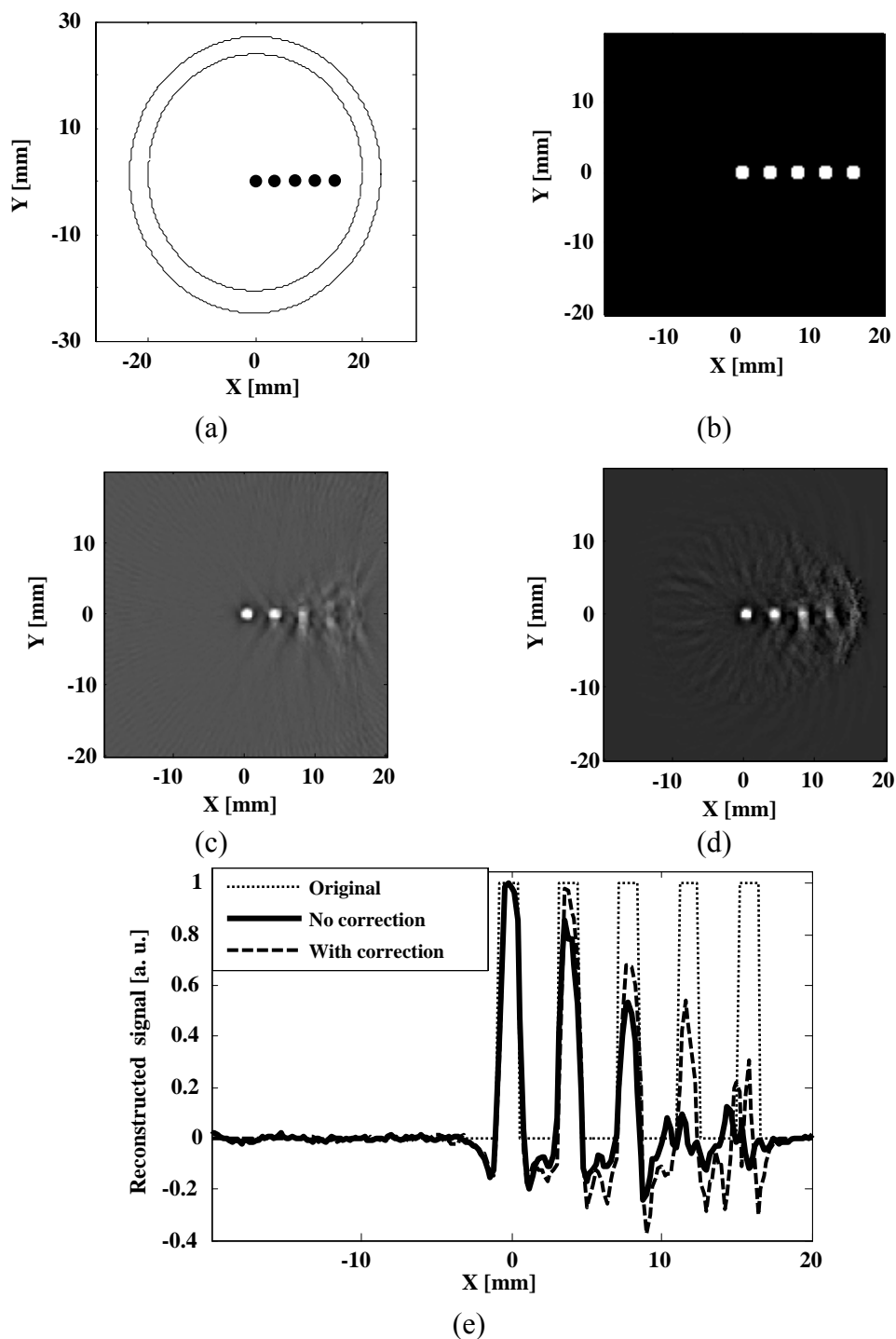


Fig. 5.3 Numerical simulation: (a) Schematic illustration of the phantom sample used in the simulation; (b) Close-up view of the five absorbers in the imaging area. The absorbers are shown as white spots; (c) Reconstructed TAT image without correction for the skull effects; (d) Reconstructed image after correction for the skull effects; (5) Comparison of the reconstructed profile across the five absorbers.

5.3.2 Experimental results

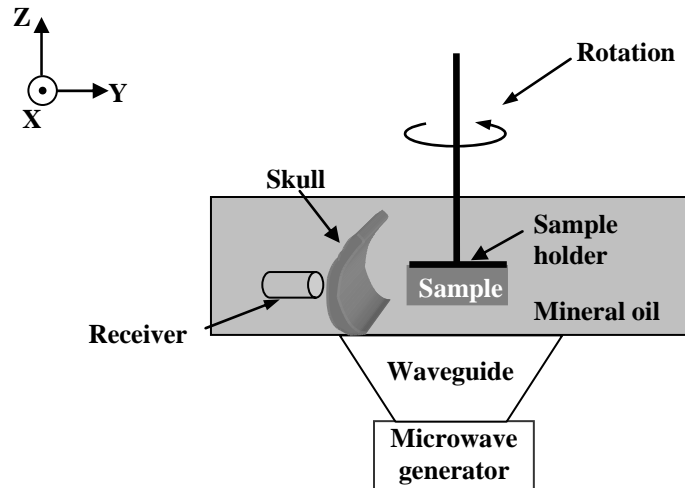


Fig. 5.4 Side view of experimental setup using a piece of monkey skull bone. The ultrasonic receiver and the skull bone were maintained unchanged in the experiment. The phantom sample was fixed on the sample holder with a string, and the sample holder was controlled by a stepping motor.

A schematic experimental setup for TAT is shown in Fig. 5.4. For all the measurements, the speed of sound in mineral oil was $1.437 \text{ mm}/\mu\text{s}$. The size of the images was 200×200 pixels. In this experimental setup, the microwave radiation level on human subject is estimated to be under the safety limit,²³ and, thus, microwave-induced-biological effects are minimal. The microwave radiation time can be further reduced by using an ultrasonic array as the receiver.

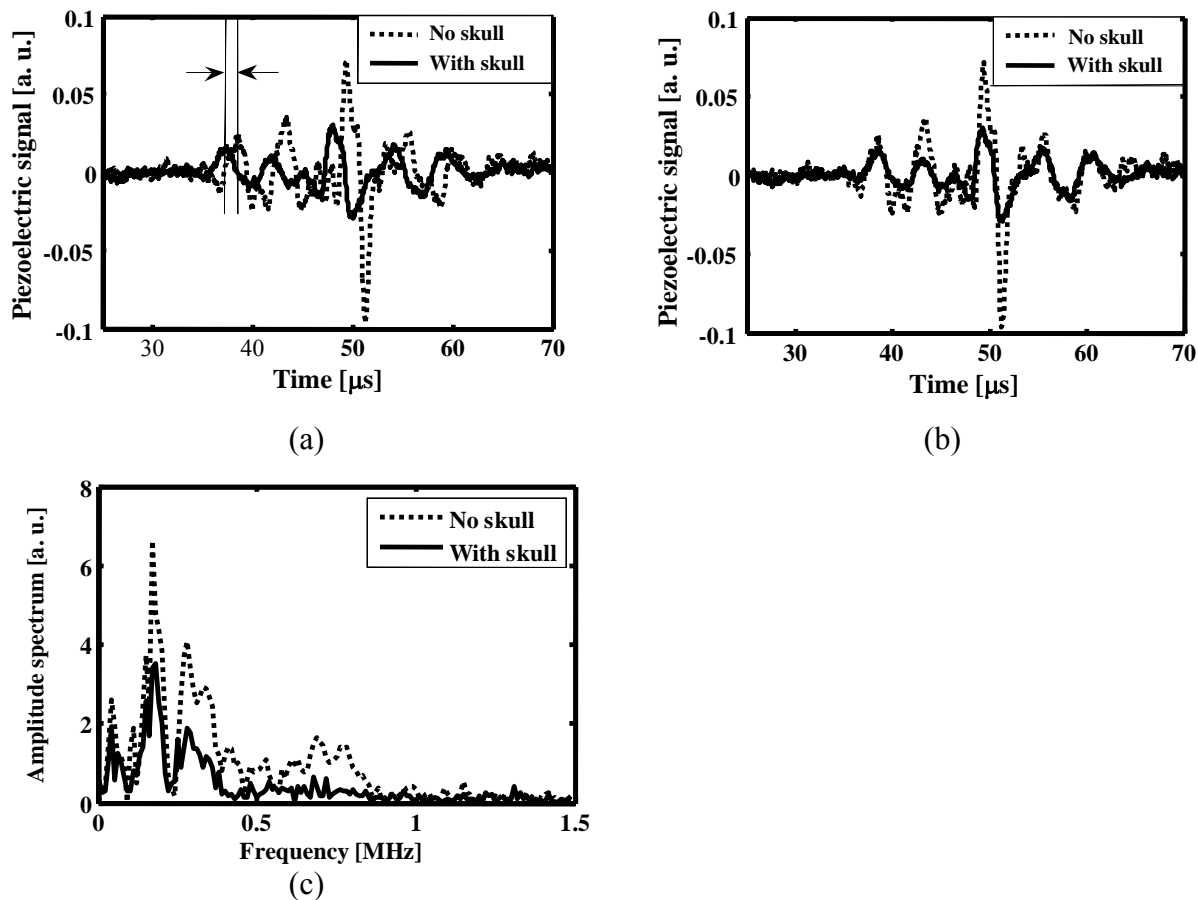


Fig. 5.5 Thermoacoustic signals after traveling through a monkey skull bone with a thickness of 6 mm: (a) Phase shift is marked by two dotted perpendicular lines. The solid line is the thermoacoustic wave with skull bone present and the dotted line is the thermoacoustic wave with skull bone absent; (b) Amplitude attenuation after phase shift has been compensated for. The solid line is the thermoacoustic wave with skull bone present and the dotted line is the thermoacoustic wave with skull bone absent; (c) Comparison of amplitude spectrum of the thermoacoustic signals with and without the skull present.

We first tested the effects of the skull attenuation on TAT image. A piece of formaldehyde-fixed parietal bone of a 10-year-old male *M. nemestrina* monkey was used to simulate the skullbone of small children. Formaldehyde-fixed skull bone has been

shown to be able to maintain the bone properties of a fresh skull,⁷⁴ and, thus, we assume the acoustic properties of the skull is identical to that of a fresh skull. The size of the skull segment was large enough to entirely cover the transducer element (6mm in diameter of active element). The attenuation of the skull fragment was about 6 dB. It has been shown that the thicknesses of children's skull range from 1 mm to 7 mm at the age from birth to 16 years old.⁸⁰ The thickness of the skull used in our experiment was measured to be around 6 mm, which was comparable to the thickness of a child's skull at the age of around 14. A phantom was made by embedding four small pieces of porcine muscle into a piece of porcine fat. Porcine muscle was used as absorbers because of its strong microwave absorption. The size of the porcine fat was approximately 42 mm × 30 mm, and the diameters of four absorbers were around 3.5 mm. The skull segment and phantom sample was immersed in mineral oil. The ultrasonic receiver and the skull remained fixed and their distance was kept constant during the experiment. The phantom sample was fixed on a sample holder by using a thin string and controlled by a stepping motor with a step size of 2.25°. The skull was positioned so that incidence angles of the ultrasonic waves were approximately normal upon the inner-skull surface. Figure 5.5(a) shows the phase shift induced by acoustic speed variations after thermoacoustic waves pass through the skull. The phase shift is marked by two perpendicular dotted lines on the graph. Phase shifts of this magnitude will have a substantial effect on the formation of a focused TAT image through the skull if we assume constant acoustic speed in the reconstruction. After we compensated for the phase distortion, the thermoacoustic signals with and without the skull present were compared in Fig. 5.5(b). We further

compared the spectra of the thermoacoustic signals with and without the skull present in Fig. 5.5(c). We found that the microwave-generated thermoacoustic signals were mostly below 1 MHz with majority of the frequency components less than 0.5 MHz. It was also observed that when the frequency was larger than 0.5 MHz, the amplitude spectrum of the thermoacoustic signal was weaker, but the attenuation induced by the skull was shown to be stronger than those in the frequency range of less than 0.5 MHz. Our results agree well with the results obtained by Fry and Barger⁷⁴ on a skull with the same thickness in the same frequency range.

Because higher frequency components determine the boundary of the reconstructed image, the amplitude of the image boundaries will be dampened most after passing through the skull, and consequently we expect blurring boundaries but still good contrast in the reconstructed image. Figure 5.6(a) is the reconstructed TAT image with the skull absent and Fig. 5.6(b) is the reconstructed TAT image with the skull present by using the filtered back-projection method. To minimize the distortion induced by the higher frequency components, especially noise and interferences, we filtered out frequency components that were greater than 2 MHz in the post-processing of the data. To get better contrast, we also filtered out DC and low frequency components that were less than 0.1 MHz. We further processed the data using the proposed numerical method based on estimated skull information from ultrasound measurement, and the reconstructed image is shown in Fig. 5.6(c). We compared line plots across the three reconstructed images in Fig. 5.6(d) at the depth marked by arrows in Fig. 5.6(a), (b) and (c). With the skull present, skull-induced attenuation was strong and consequently the

reconstructed images were weaker than the image obtained in Fig. 5.6(a) and the boundaries looked less sharp. In spite of that, both reconstruction methods show good

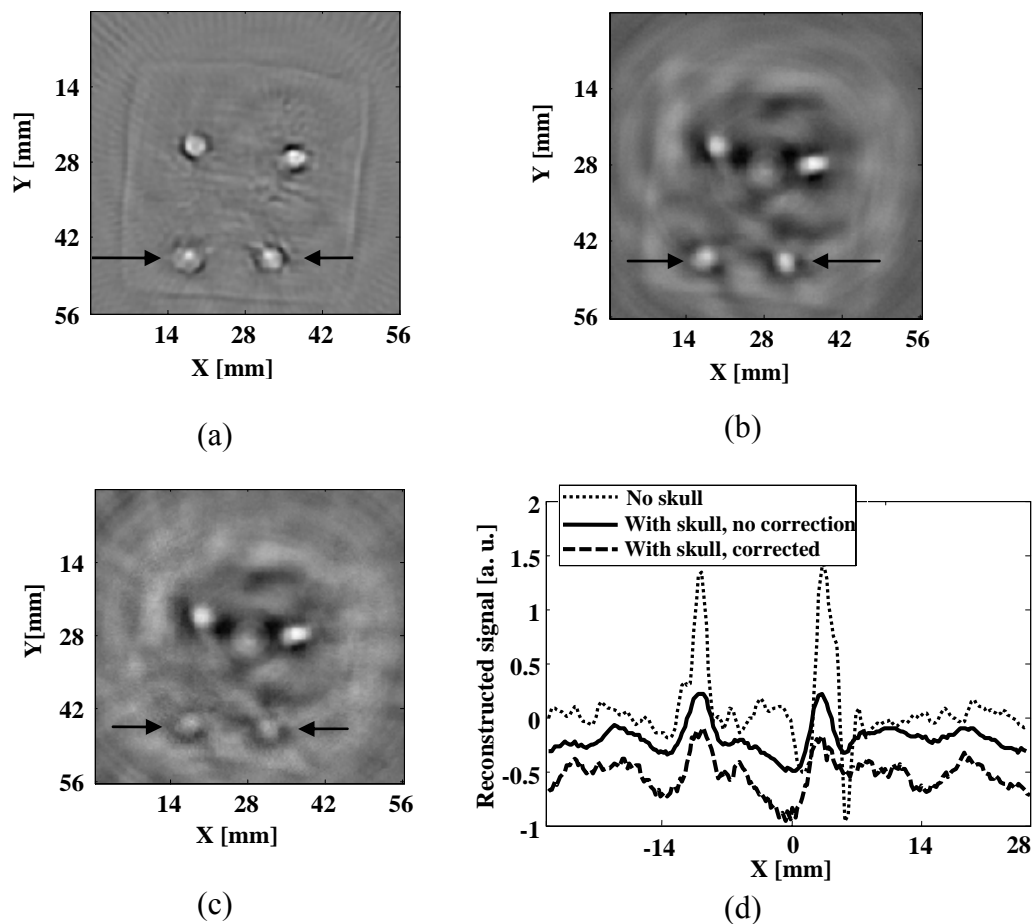


Fig. 5.6 Reconstructed TAT image (a) using filtered back-projection method when skull was absent; (b) using filtered back-projection method when skull was present; (c) using proposed numerical method when skull was present; (d) comparison of the reconstructed signals at the depth as marked on (a), (b), and (c). The plots from (b) and (c) were shifted along the y-axis.

images. Moreover, although the measurement errors of the skull introduced some noises to the image obtained by the proposed numerical method, the line plot in Fig. 5.6(d) showed that both reconstruction methods had similar results. This is because the four absorbers were close to the image center, the effects of wave refraction and mode conversion were minimal and consequently the distortion was ignorable in the reconstructed images.

Next, we tested the effects of wave refraction and mode conversion on TAT. The size of the brain and the skull covering the brain of the monkey used in the previous experiment limited its use to investigate the human skull-induced distortions on TAT. Because we focused on studying the effects of refraction on TAT image, in this preliminary study we used a PVC tube in regular shape to mimic the reflection and refractive effects of the skull and to obtain its position by using ultrasound pulse-echo imaging. We chose PVC tube because of its high acoustic speed, which was close to the acoustic speed in the skull. Thickness of the PVC tube was 3 mm, the acoustic speed was measured to be 2.39 mm/us, and the density was estimated to be 1380 kg/m^3 . The densities of the fat and mineral oil were around 920 kg/m^3 and 850 kg/m^3 , respectively.³² We made a tissue phantom by burying two small strong absorbers made by porcine muscle in porcine fat. The size of the porcine fat was $30 \text{ mm} \times 15 \text{ mm}$ and the diameters of the absorbers were around 3.5 mm. The whole phantom was then immersed in mineral oil and placed on a sample base on the X-Y plane. The transducer was mounted on a mechanical arm controlled by a stepping motor, and then scanned the tissue sample circularly to acquire two dimensional projection data. Figure 5.7(a) is a

schematic of the sample with the PVC tube used in the experiments, where the phantom sample is close to the left side of PVC tube, and Fig. 5.7(b) is the reconstructed TAT image without the PVC tube present. Figure 5.7(c) is the reconstructed TAT images with the PVC present by using the filtered back-projection method. By neglecting the wave refraction and mode conversion at the interfaces between the PVC tube and the surrounding media, the imaging region close to the inner-tube surface was distorted seriously, and if we neglected the refraction effects, it was impossible to obtain acceptable images. By using the proposed numerical method, we corrected refraction effects and improved the shear waves induced distortions. Figure 5.7(d) is the corrected image, which shows improvement of the un-compensated image. We further compared two reconstruction methods in Fig 5.7(e) by plotting their reconstructed signals at the depth marked by arrows in Figs. 5.7(c) and (d). The major sources of discrepancy between the TAT image without the PVC layer present and the one with the PVC layer present resulted from neglecting shear waves and measurement errors.

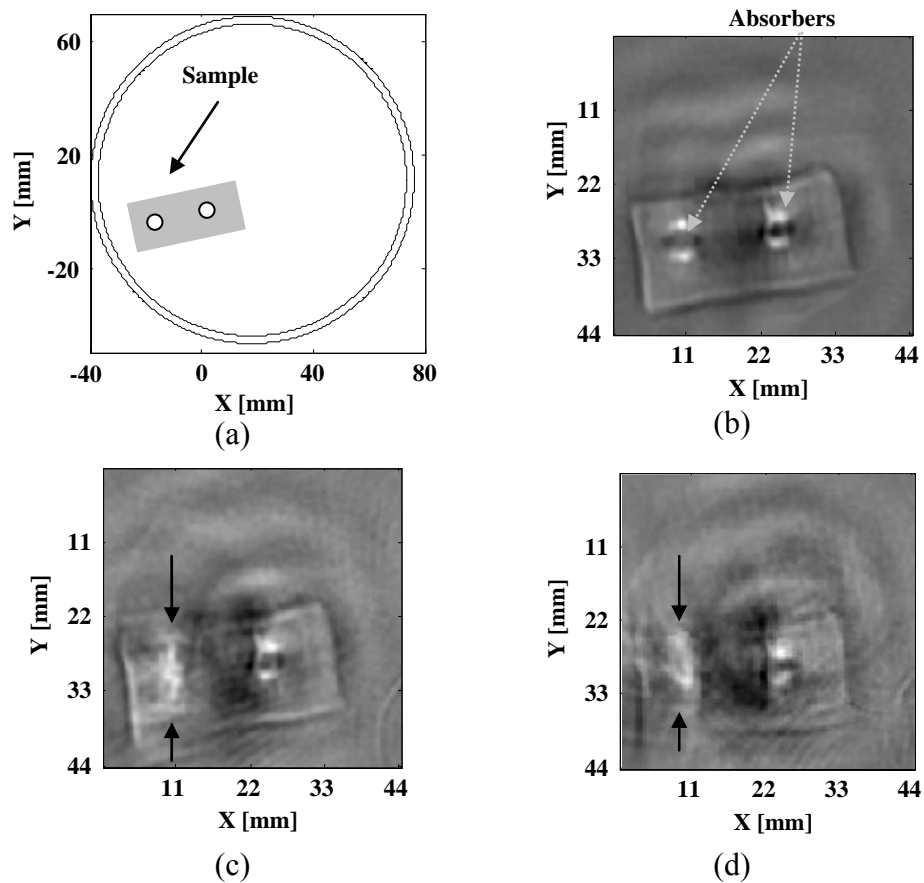


Fig. 5.7 Experimental results with two strong absorbers: (a) Schematic of the phantom sample used in experiments; (b) reconstructed image when no PVC tube was used in the experiment. The boundaries of the two absorbers are shown clearly in the reconstructed TAT image; (c) Reconstructed TAT image using the filtered back-projection method. PVC tube was used to simulate the skull effects. The sample was close to the left side of the inner PVC tube; (d) Reconstructed TAT image using the numerical method proposed in this section. The raw data was same as used for (c); (e) Reconstructed profiles across the region at the depth as marked on (c) and (d).

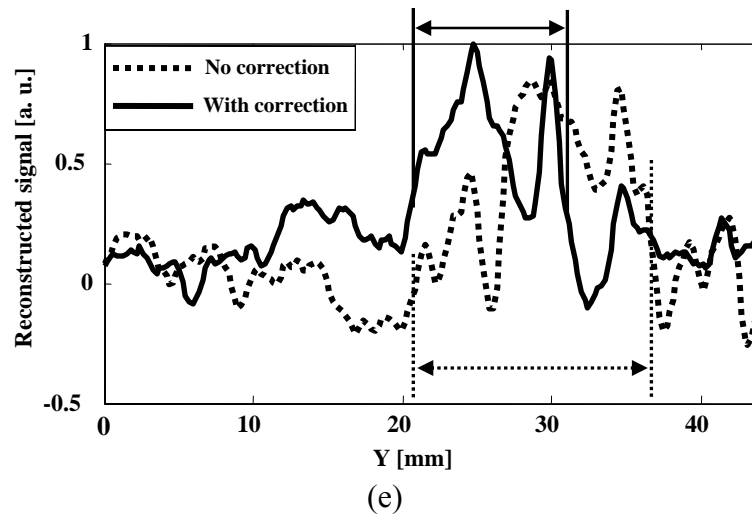


Fig. 5.7 Continued.

We did another phantom experiment by using porcine fat and a thin metal wire. The size of the porcine fat was $40 \text{ mm} \times 16 \text{ mm}$, the diameter of the metal wire was 0.1143 mm and the length was 40 mm . Same PVC tube used in the previous experiment was adopted to simulate the wave reflection and refraction effects. The whole phantom was then immersed in mineral oil and placed on a sample base on the X-Y plane. The data collection process was same as in the previous experiment. Figure 5.8(c) and (d) are the reconstructed images with the tissue sample close to the upper side of the PVC tube. In Fig.5.8(c), the wire was distorted seriously in the region close to the inner-tube surface due to neglecting the effects of the wave refraction and mode conversion. By using the proposed numerical method, we corrected those distortions with the measured information about the tube in Fig.5.8(d). The line plots across the regions marked by

arrows in Fig.5.8(b) and Fig.5.8(c) were compared in Fig.5.8(e). The proposed method shows improved image quality as compared with the filtered backprojection method.

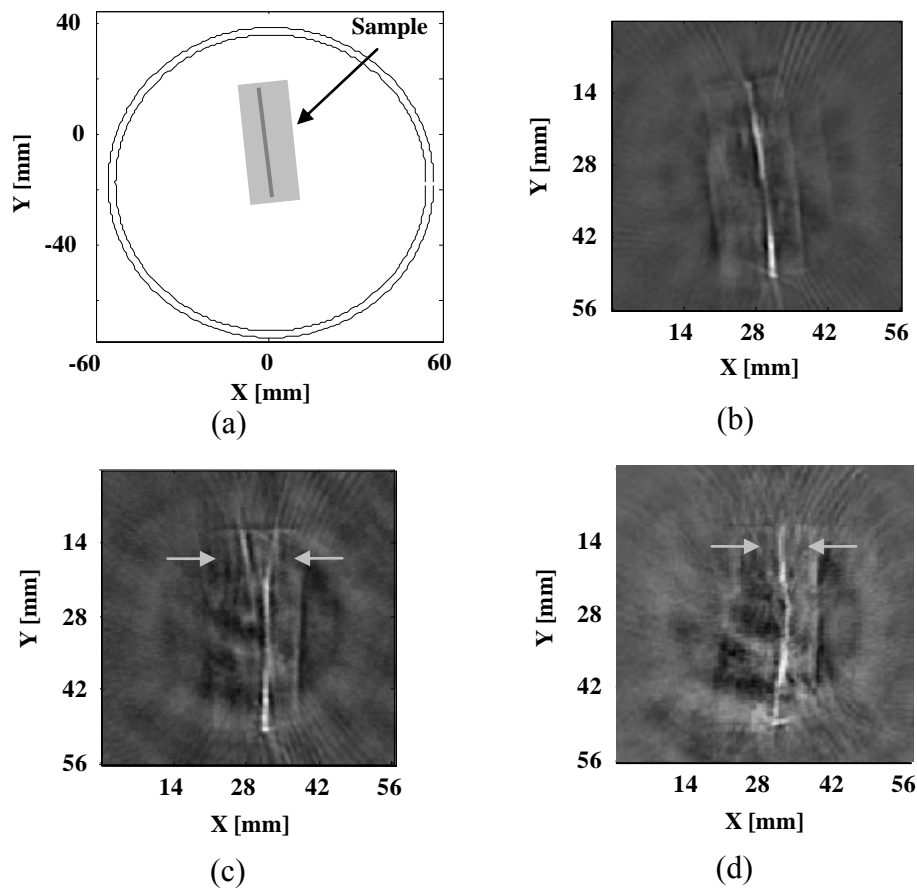


Fig. 5.8 Experimental results with a wire object: (a) Schematic of the phantom sample used in experiments; (b) Reconstructed image when no PVC tube was used in the experiment. The wire is shown to be near straight. (c) Reconstructed TAT image using the filtered back-projection method. PVC tube was used to simulate the skull effects. The top of the wire was close to the inner PVC tube; (d) Reconstructed TAT image using the numerical method proposed in this section. The raw data was same as used for (c); (e) Reconstructed profiles across the region at the depth as marked on (c) and (d).

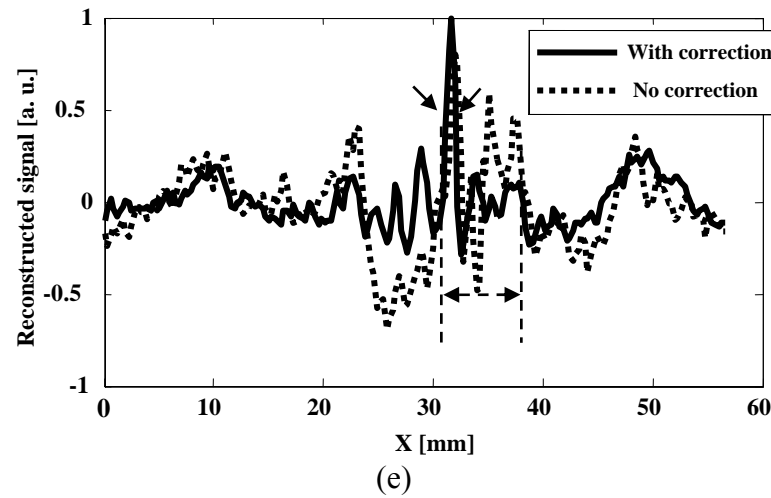


Fig.5.8 Continued.

5.4 Discussion

The purpose of this section is to explore the effects of acoustic heterogeneities on transcranial brain imaging with TAT. We find that if the imaging object is close to the center of the brain, the object can be imaged well. When the object gets closer to the inner-skull surface, however, the distortion brought by the refraction and mode conversion becomes a serious problem. By examining the wave reflection and refraction on the TAT image, it is shown that when the skull shape and acoustic properties are provided, we can correct the phase distortions and remove the artifacts.

The skull is assumed to be acoustically homogeneous in this preliminary study. In real applications, however, the skull bone is an acoustically inhomogeneous material that consists of three relatively homogeneous layers: the outer and the inner ivory tables and the central dipole layer. The ivory tables cause attenuation primarily through

reflections at the interfaces, and the dipole can induce both strong attenuation and scattering. It has also been shown that acoustic speeds can vary greatly in those three layers. The effectiveness of the numerical compensation method is, thus, limited by the accuracy of the information on the inner and outer skull surfaces, thickness of the skull, and internal structure of the skull. In this preliminary study we use ultrasonic pulse-echo imaging to obtain the position the PVC tube, which is later used to correct the distortion of TAT image. Ultrasound imaging modality, however, is incapable to provide accurate measurements on the shape and structures of the skull bone. Fortunately, studies on ultrasonic therapy have shown that MRI and CT can provide accurate shape and thickness information on the skull, and, especially, CT can provide accurate profiles of inner-skull surface and outer-skull surface, and position-dependent density, speed of sound and absorption information of three different layers in the skull, thus it is preferable to use CT-derived skull information to compensate for the distortion induced by the skull in TAT brain imaging.^{82,87} By adjusting the propagation speeds using the thickness and density information obtained by CT, we can improve the phase compensation and consequently obtain better image quality.

The effects of shear waves on TAT image have been neglected in our numerical reconstruction algorithm. When the target regions are closer to the skull surface, however, more incidence angles will become large. By removing the shear waves from our reconstruction, we neglect the distortion brought by shear waves, but, meanwhile, we lose information at those regions and consequently make image intensity at those regions weak. Studies show that if we can quantitatively evaluate the shear waves in the

skull bone, we can incorporate shear wave for imaging.^{83,88} Further experiment by including shear waves in the numerical model may enhance the image quality at the region that is close to the inner-skull surface.

5.5 Conclusion

We evaluated the effects of acoustic heterogeneities on transcranial brain imaging with TAT in this study. A numerical model was proposed. Numerical simulation based on this model was compared with experimental results. The results obtained with our model conform to experimental results well. We further evaluate the conditions under which we can ignore the skull effects in image reconstruction. We also showed that by incorporating the skull shape and acoustic properties into image reconstruction, the image quality can be improved. This study is an important step toward improving the image quality of trans-skull brain imaging with TAT.

6. SUMMARY AND CONCLUSIONS

Thermoacoustic tomography (TAT) has been developed to overcome the limitations of both conventional ultrasound and microwave imaging. Owing to its large penetration depth of microwave and sensitivity to the change of dielectric properties in the tissue, TAT has some unique physical and chemical properties.

HIFU-induced lesions in porcine muscle were imaged with TAT. Our preliminary results have shown that TAT has the capacity to visualize HIFU-induced lesions with good contrast using a local-tomography-type reconstruction algorithm. The boundaries of different tissues can be imaged clearly. The size and position of lesions measured from TAT images were compared with the size and position of those measured from gross pathologic photographs. It was established that TAT can estimate the size of lesions effectively. This preliminary study demonstrates that TAT has the potential to provide an effective, low-cost alternative method for imaging HIFU-induced lesions.

Clinical experimental data were obtained for breast tumors at M. D. Anderson cancer center. We obtained high contrast between the malignant tissue and normal tissue. Those data verified the effectiveness of using TAT in breast cancer imaging.

To compensate for the effects of acoustic speed variations on early detection of breast tumors, we proposed a method by using ultrasound transmission tomography that was compatible with our TAT system. It was shown that ultrasound transmission tomography can, within certain limitations, generate accurate and quantitative images of the acoustic speed distributions of phantoms, which results in high registration accuracy in the TAT images. It was also shown by phantom experiments that those acoustic speed

images had sufficient accuracy to compensate for the effects of acoustic speed heterogeneities in TAT images. The results obtained by this system indicate that TAT with the acoustic speed compensation is a feasible approach for obtaining higher resolution images of small tumors in acoustically heterogeneous tissues.

Finally, we evaluated the effects of wave reflection and refraction on transcranial brain imaging with TAT. A numerical model considering reflection and refraction was proposed. The results obtained with the numerical model conformed to the experimental results well. From our simulation and experimental results, it is found that when the target region is close to the center of the brain, the effects caused by the skull layer is minimal and both reconstruction methods work well. As the target region gets closer to the interface between the skull and brain tissue, however, the skull-induced distortion becomes increasingly severe, the reconstructed image without correcting those effects would be strongly distorted. In this case, the proposed numerical method can improve the image quality by taking into consideration of the wave refraction and mode conversion at the skull surfaces. In the future, by incorporating the measurements of shear waves the image quality may be further improved.

REFERENCES

1. K. R. Foster and E. D. Finch, "Microwave hearing: evidence for thermoacoustic auditory stimulation by pulsed microwaves," *Science* **185**(147) 256-258 (1974).
2. R. T. V. Gutfeld, "Thermoelastic generation of elastic waves for non-destructive testing and medical diagnostics," *Ultrasonics*. **18**(4), 175-181 (1980).
3. T. Bowen, "Radiation-induced thermoacoustic soft tissue imaging," *Proc. IEEE Ultrason. Symp.* **2**, 817-822 (1981).
4. R. G. Olsen, "Generation of acoustic images from the absorption of pulsed microwave energy," in *Acoustic Imaging*, edited by J. P. Powers (Plenum Publishing, New York, 1982), pp. 53-59.
5. J. C. Lin and K. H. Chan, "Microwave thermoelastic tissue imaging –system design," *IEEE Trans. Microwave Theory Tech* **32**, 854-860 (1984).
6. A. Oraevsky, R. Esenaliev, S. Jacques, and F. Tittel, "Laser optoacoustic tomography for medical diagnostics – principles," *Proc. of SPIE* 2676, 22-31 (1995).
7. R. G. M. Kolkman, E. Hondebrink, W. Steenbergen, and F. F. M. de Mul, "In vivo photoacoustic imaging of blood vessels using an extreme-narrow aperture sensor," *IEEE J. Sel. Top. Quant.* **9**, 343–346 (2003).
8. X. Wang, Y. Pang, G. Ku, X. Xie, G. Stoica, and L. V. Wang, "Non-invasive laser-induced photoacoustic tomography for structural and functional imaging of the brain *in vivo*," *Nat. Biotechnol.* **21**, 803–806 (2003).
9. K. Maslov, G. Stoica, and L.-H. Wang, "In vivo dark-field reflection-mode photoacoustic microscopy," *Opt. Lett.* **30**(6), 625–627 (2005).

10. H. F. Zhang, K. Maslov, G. Stoica, and L.-H. Wang, "Functional photoacoustic microscopy for high-resolution and noninvasive in vivo imaging," *Nat. Biotechnol.* **24**, 848–851 (2006).
11. G. Ku and L.-H. Wang, "Deeply penetrating photoacoustic tomography in biological tissues enhanced with an optical contrast agent," *Opt. Lett.* **30**(5), 507–509 (2005)
12. J. H. Jacobi and L. E. Larsen, "Linear FM pulse compression radar techniques applied to biological imaging," in *Medical Applications of Microwave Imaging*, edited by L. E. Larsen and J. H. Jacobi (IEEE Press, New York, 1985), pp. 138-147.
13. K. R. Foster and J. L. Schepps, "Dielectric properties of tumor and normal tissue at radio through microwave frequencies," *J. Microwave Power* **16**(2), 107-119 (1981)
14. C. Gabriel, S. Gabriel, and E. Corthout, "The dielectric properties of biological tissues: I. Literature survey," *Phys. Med. Biol.* **41**, 2231–2249 (1996)
15. S. Gabriel, R. W. Lau, and C. Gabriel, "The dielectric properties of biological tissues: II. Measurements in the frequency range 10 Hz to 20 GHz," *Phys. Med. Biol.* **41**, 2251–2269 (1996)
16. S. Gabriel, R. W. Lau, and C. Gabriel, "The dielectric properties of biological tissues: III. Parametric models for the dielectric spectrum of tissues," *Phys. Med. Biol.* **41**, 2271–2293 (1996)
17. S. S. Chaudhary, R. K. Mishra, A. Swarup, and J. M. Thomas, "Dielectric properties of normal and malignant human breast tissues at radiowave and microwave frequencies," *Indian J. Biochem. Biophys* **21**, 76-9 (1984).

18. R. A. Kruger, K. K Kopecky, A. M. Aisen, D. R. Reinecke, G A. Kruger, and W. L. Kiser Jr., "Thermoacoustic CT with radio waves: a medical imaging paradigm," *Radiology*, **211**, 275-278 (1999).
19. L.-H. Wang, X. Zhao, H. Sun, and G. Ku, "Microwave-induced acoustic imaging of biological tissues," *Rev. Sci. Instr.* **70**, 3744-3748 (1999).
20. G. Ku and L.-H. Wang, "Scanning thermoacoustic tomography in biological tissue," *Med. Phys.* **27**, 1195-1202 (2000).
21. R. A. Kruger, K. Stantz, and W. L. Kiser Jr., "Thermoacoustic CT of the breast," *Proc. SPIE* **4682**, 521-525 (2002).
22. R. A. Kruger, K. D. Miller, H. E. Reynolds, W. L. Kiser, D. R. Reinecke, and G. A. Kruger, "Breast cancer in vivo: contrast enhancement with thermoacoustic CT at 434 MHz-feasibility study," *Radiology* **216**, 279-283 (2000).
23. Y. Xu and L.-H. Wang, "Rhesus monkey brain imaging through intact skull with thermoacoustic tomography," *IEEE Trans. Ultrason., Ferroelect., and Freq. Contr.* **53**, 542-548 (2006).
24. G. Ku, B. D. Fornage, X. Jin, M. Xu, K. K. Hunt, and L.-H. Wang, "Thermoacoustic and photoacoustic tomography of thick biological tissues toward breast imaging," *Tech. Cancer Res. Treat.* **4**, 559-566 (2005).
25. K. G. Ayappa, H. T. Davis, E. A. Davis, and J. Gordon, "Analysis of microwave heating of materials with temperature-dependent properties," *AIChE Journal* **37** 313–322 (1991).

26. W. B. Weir, "Automatic measurement of complex dielectric constant and permeability at microwave frequencies," *Proc. IEEE* **62**(1), 33-36 (1974).
27. P. Gajsek, J. A. D'Andrea, P. A. Mason, J. M. Zirix, T. J. Walters, and W. D. Hurt, "Mathematical modeling using experimental and theoretical methods in evaluating specific absorption rates (SAR)," in *Biological Effects of Electromagnetic Fields*, edited by P. Stavroulakis (Springer, Berlin, 2003), pp. 116-170.
28. J. R. Birchack, C. G. Gardner, J. E. Hipp, and J. M. Victor, "High dielectric constant microwave probes for sensing soil moisture." *Proc. IEEE* **62**(1), 93-98 (1974).
29. D. K. Kim, M. S. Amin, S. Elborai, S.-H. Lee, Y. Koseoglu, M. Zahn, and M. Muhammed, "Energy absorption of superparamagnetic iron oxide nanoparticles by microwave irradiation," *Jour. Appl. Phys.* **97**, 10J510-10J510-3 (2005).
30. S. Ray and J. Behari, "Microwave absorption in lossy liquids," *Phys. Med. Biol.*, **31**(9), 1031-1040 (1986).
31. D. V. Blackham and R. D. Pollard, "An improved technique for permittivity measurements using a coaxial probe." *IEEE Trans. Instr. Meas.* **46**(5), 1093- 1099 (1997)
32. F. A. Duck, *Physical Properties of Tissue, a Comprehensive Reference Book*. (Academic Press, London, 1990).
33. C. J. Harvey, J. M. Pilcher, R. J. Eckersley, M. J. K. Blomley, and D. O. Cosgrove, "Advances in ultrasound," *Clinical Radiology* **57**, 157-177 (2002).
34. G. T. Haar, "Ultrasound focal beam surgery," *Ultrasound in Med. & Biol.* **21**, 1089-1100 (1995).

35. G. T. Haar, "Acoustic surgery," *Phys. Today*, **54**(12), 29-34 (2001).
36. G. T. Haar, D. Sinnett, and I. Rivens, "High intensity focused ultrasound-a surgical technique for the treatment of discrete liver tumors," *Phys. Med. Biol.* **34**, 1743-1750 (1989).
37. F. Wu, Z.-B. Wang, W.-Z. Chen, J.-Z. Zou, J. Bai, H. Zhu, K.-Q. Li, F.-L. Xie, C.-B. Jin, H.-B. Su, and G.-W. Gao, "Extracorporeal focused ultrasound surgery for treatment of human solid carcinomas: early Chinese clinical experience," *Ultrasound in Med. & Biol.* **30**, 245-260 (2004).
38. K. Hynynen, O. Pomeroy, D. N. Smith, P. E. Huber, N. J. McDannold, J. Kettenbach, J. Baum, S. Singer, and F. A. Jolesz, "MR imaging-guided focused ultrasound surgery of fibroadenomas in the breast: a feasibility study," *Radiology* **219**, 176-185 (2001).
39. C. Weidensteiner, B. Quesson, B. Caire-Gana, N. Kerioui, A. Rullier, H. Trillaud, and C. T. W. Moonen, "Real-time MR temperature mapping of rabbit liver *in vivo* during thermal ablation," *Mag. Reson. Med.* **50**, 322-330 (2003).
40. C. M. C. Tempany, E. A. Stewart, N. McDannold, B. J. Quade, F. A. Jolesz, and K. Hynynen, "MR-imaging –guided focused ultrasound surgery of uterine leiomyomas: a feasibility study," *Radiology* **226**, 897-905 (2003).
41. N. L. Bush, I. Rivens, G. R. T. Haar, and J. C. Bamber, "Acoustic properties of lesions generated with an ultrasound therapy system," *Ultrasound in Med. & Biol.* **19**, 789-801 (1993).

42. A. E. Worthington, J. Trachtenberg, and M. D. Sherar, "Ultrasound properties of human prostate tissue during heating," *Ultrasound in Med. & Biol.* **28**, 1311-1318 (2002).
43. R. Righetti, F. Kallel, R. J. Stafford, R. E. Price, T. A. Krouskop, J. D. Hazle, and J. Ophir, "Elastographic characterization of HIFU-induced lesions in canine livers," *Ultrasound in Med. & Biol.* **25**, 1099-1113 (1999).
44. F. L. Lizzi, R. Muratore, C. X. Deng, J. A. Ketterling, S. K. Alam, S. Mikaelian, and A. Kalisz, "Radiation-force technique to monitor lesions during ultrasonic therapy," *Ultrasound in Med. & Biol.* **29**, 1593-1605 (2003).
45. I. J. Rowland, I. Rivens, L. Chen, C. H. Lebozer, D. J. Collins, G. R. T. Haar, and M. O. Leach, "MRI study of hepatic tumors following high intensity focused ultrasound surgery," *The British J. Radiology* **70**, 144-153 (1997).
46. F. Wu, W.-Z. Chen, J. Bai, J.-Z. Zou, Z.-L. Wang, H. Zhu, and Z.-B. Wang, "Tumor vessel destruction resulting from high-intensity focused ultrasound in patients with solid malignancies," *Ultrasound in Med. & Biol.* **28**, 535-542 (2002).
47. P. Vaupel, "Pathophysiological mechanisms of hyperthermia in cancer therapy," in *Biological Basis of Oncologic Thermootherapy*, edited by M. Gautherie (Springer-Verlag, Berlin, 1990), pp. 73-134.
48. Y. Xu, G. Ambartsoumian, P. Kuchment, and L.-H. Wang, "Reconstructions in limited-view thermoacoustic tomography," *Med. Phys.* **31**, 724-733 (2004).
49. M. Xu, and L. V. Wang, "Time-domain reconstruction for thermoacoustic tomography in a spherical geometry," *IEEE Trans. Med. Imag.* **21**, 814-822 (2002).

50. M. Xu, Y. Xu, and L.-H. Wang, "Time-domain reconstruction algorithms and numerical simulations for thermoacoustic tomography in various geometries," *IEEE Trans. Biomed. Engr.* **50**, 1086-1099 (2003).
51. M. Xu and L.-H. Wang, "Universal back-projection algorithm for photoacoustic computed tomography," *Phys. Rev. E* **71**, 1-7 (2005).
52. D. A. McRae and M. A. Esrick, "The dielectric parameters of excised EMT-6 tumors and their change during hyperthermia," *Phys. Med. Biol.* **37**, 2045-2058 (1992).
53. M. Pop, A. Molckovsky, L. Chin, M. C. Kolios, M. A. Jewett, and M. D. Sherar, "Change in dielectric properties at 460 kHz of kidney and fat during heating: importance for radio-frequency thermal therapy," *Phys. Med. Biol.* **48**, 2509-2525 (2003).
54. L. Chin and M. Sherar, "Changes in dielectric properties of ex vivo bovine liver at 915 MHz during heating," *Phys. Med. Biol.* **46**, 197-211 (2001).
55. P. S. Treuhaft and D. J. McCarty, "Synovial fluid pH, lactate, oxygen and carbon dioxide partial pressure in various joint diseases," *Arthritis. Rheum.* **14**, 475-484 (1971)
56. H. Sato, T. Takahashi, H. Ide, T. Fukushima, M. Tabata, F. Sekine, K. Kobayashi, M. Negishi, and Y. Niwa., "Antioxidant activity of synovial fluid, hyaluronic acid, and two subcomponents of hyaluronic acid," *Arthritis. Rheum.* **31**, 63-71 (1988)
57. K. L. Goa and P. Benfield, "Hyaluronic acid: a reivew of its pharmacology and use as a surgical aid in ophthalmology, and its therapeutic potential in joint disease and wound healing," *Drugs*, **47**(3), 536-566 (1994)

58. X. Wang, D. L. Chamberland, P. L. Carson, J. B. Fowlkes, R. O. Bude, D. A. Jamadar, and B. J. Roessler, "Imaging of joints with laser-based photoacoustic tomography: an animal study," *Med. Phys.* **33**(8), 2691-2697 (2006)
59. Y. Xu and L.-H. Wang, "Effects of acoustic heterogeneity in breast thermoacoustic tomography," *IEEE Trans. Ultrason., Ferroelect., and Freq. Contr.* **50**, 1134-1146 (2003).
60. T. L. Chenevert, D. I. Bylski, P. L. Carson, C. R. Meyer, P. H. Bland, D. D. Adler, and R. M. Schmitt, "Ultrasonic computed tomography of the breast," *Radiology* **152**, 155-159, (1984)
61. G. H. Clover and J. C. Sharp, "Reconstruction of ultrasound propagation speed distribution in soft tissue: time-of-flight tomography," *IEEE Trans. on Sonics and Ultrasonics* **24**, 229-234 (1977).
62. J. R. Jago and T. A. Whittingham, "Experimental studies in transmission ultrasound computed tomography," *Phys. Med. Biol.* **36**, 1515-1527 (1991).
63. J. H. Kim, S. B. Park, and S. A. Johnson, "Tomography imaging of ultrasonic reflectivity with correction for acoustic speed variations," *Ultrason. Imag.* **6**, 304-312 (2005).
64. M. Yamasaki, N. Shigeru, M. Hisaharu, K. Sunao, and K. Shunichi, "A review of breast cancer undetectable by ultrasonography in a screening setting," in *Research and Development in Breast Ultrasound*, edited by E. Ueno, T. Shiina, M. Kubota and K. Sawai, (Springer-Verlag, Tokyo, 2005), pp. 163-166.

65. J. G. Berryman, "Fermat's principle and nonlinear traveltime tomography," *Phys. Rev. Lett.* **62**, 2953-2956 (1989).
66. R. Snieder and D. F. Aldridge, "Perturbation theory for travel times," *J. Acoust. Soc. Am.* **98**, 1565-1569 (1995).
67. A. C. Kak and M. Slaney, *Principles of Computerized Tomographic Imaging*, (IEEE Press, New York, 2005).
68. G. J. Diebold, T. Sun, and M. I. Khan, "Photoacoustic monopole radiation in one, two and three dimensions," *Phys. Rev. Lett.* **67**, 3384-3387, (1991)
69. L. E. Kinsler, A. R. Frey, and A. B. Coppens, J. V. Sanders, *Fundamentals of Acoustics*, (John Wiley & Sons, Inc., New York, 2000).
70. C. C. Paige and M. A. Saunders, "LSQR: an algorithm for sparse linear equations and sparse least squares," *ACM Trans. on Mathematical Software* **8**, 43-71 (1982).
71. A. H. Andersen, "Ray tracing approach to restoration and resolution enhancement in experimental ultrasound tomography," *Ultrason. Imag.* **12** 268-291 (1990).
72. F. Denis, O. Basset, and G. Gimenez, "Ultrasonic transmission tomography in refracting media: reduction of refraction artifacts by curved-ray techniques," *IEEE, Trans. Med. Imag.* **14**, 173-188 (1995).
73. B. Mi and I. C. Ume, "Three-dimensional ray tracing laser ultrasound for weld penetration sensing," *J. Acoust. Soc. Am.* **115**, 1565-1571 (2004).
74. F. Fry and J. Barger, "Acoustical properties of the human skull," *J. Acoust. Soc. Amer.* **63**, 1576-1590 (1978).

75. G. T. Clement and K. Hynynen, "Correlation of ultrasound phase with physical skull properties," *Ultrasound in Med. & Biol.* **28**, 617-624 (2002).
76. P. Lasaygues, E. Quedraogo, J.-P. Lefebvre, M. Gindre, M. Talmant, and P. Laugier, "Progress towards in vitro quantitative imaging of human femur using compound quantitative ultrasonic tomography," *Phys. Med. Biol.* **50**, 2633-2649 (2005).
77. K. A. Dines, F. J. Fry, J. T. Patrick, and R. L. Gilmor, "Computerized ultrasound tomography of the human head: experimental results," *Ultrason. Imag.* **3**, 342-351 (1981).
78. J. Ylitalo, J. Koivukangas, and J. Oksman, "Ultrasonic reflection mode computed tomography through a skullbone," *IEEE Trans. Biomed. Eng.* **37**, 1059-1066 (1990).
79. B. A. Holland, D. K. Haas, D. Norman, M. Brant-Zawadzki, and T. H. Newton, "MRI of normal brain maturation," *AJNR Am. J. Neuroradiol.* **7**, 201-208 (1986).
80. M. Letts, D. Kaylor, and G. Gouw, "A biomechanical analysis of halo fixation in children," *J. Bone Joint Surgery* **70**, 277-279 (1988).
81. X. Jin and L. V. Wang, "Thermoacoustic tomography with correction for acoustic speed variations," *Phys. in Med. and Biol.* **51**, 6437-6448 (2006).
82. J.-F. Aubry, M. Tanter, M. Pernot, J.-L. Thomas, and M. Fink, "Experimental demonstration of noninvasive transskull adaptive focusing based on prior computed tomography scans," *J. Acoust. Soc. Am.* **113**, 84-93 (2004).

83. P. J. White, G. T. Clement, and K. Hynynen, "Longitudinal and shear mode ultrasound propagation in human skull bone," *Ultrasound in Med. & Biol.* **32**, 1085-1096 (2006).
84. X. Fan and K. Hynynen, "The effects of curved layers on the power deposition pattern of therapeutic ultrasound beams," *Med. Phys.* **21**, 25-34 (1994).
85. J. Sun and K. Hynynen, "Focusing of therapeutic ultrasound through a human skull: a numerical study," *J. Acoust. Soc. Am.* **104**(3), 1705-1715 (1998).
86. J. D. N. Cheeke, "Reflection and transmission of ultrasonic waves at interface," in *Fundamentals and Applications of Ultrasonic Waves*, (CRC Press, Boca Raton, FL, 2002), pp. 115-142.
87. J. Sun and K. Hynynen, "The potential of transskull ultrasound therapy and surgery using the maximum available skull surface area," *J. Acoust. Soc. Am.* **105**, 2519-2527 (1999).
88. G. T. Clement, P. J. White, and K. Hynynen, "Enhanced ultrasound transmission through the human skull using shear mode conversion," *J. Acoust. Soc. Am.* **115**, 1356-1363, (2004).

VITA

Xing Jin received her B.S. in electronic engineering from Northwestern Polytechnical University (Xi'an, China) in 1995 and her M.S. in electrical engineering from Louisiana State University in 2002. She started her research in Dr. Lihong Wang's lab at Texas A&M University in the spring of 2003. Her research focused on developing applications for microwave-induced thermoacoustic tomography and correcting for the effects of acoustic heterogeneities on thermoacoustic tomography. She received her Ph.D. in biomedical engineering in December 2007.

Xing Jin

c/o Dr. Kenith Meissner

337 Zachry Engineering Center

TAMU 3120

College Station, TX 77843-3120